

The interface in demixed colloid-polymer systems

Wetting, waves and droplets

**The interface in demixed
colloid-polymer systems**

Wetting, waves and droplets

**Het grensvlak in ontmengde
colloïd-polymeer systemen**

Bevochtiging, golven en druppels

(met een samenvatting in het Nederlands)

Proefschrift

ter verkrijging van de graad van doctor aan de
Universiteit Utrecht op gezag van de Rector Magnificus,
Prof. dr. W. H. Gispen, ingevolge het besluit van het
College voor Promoties in het openbaar te verdedigen
op 23 mei 2005 des namiddags te 14.30 uur

door

Dirk Gerard Albert Louis Aarts

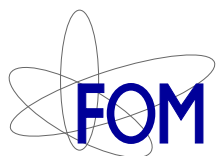
geboren op 10 november 1977 te Nijmegen



Universiteit Utrecht

Promotor: Prof. dr. H. N. W. Lekkerkerker

Verbonden aan de Faculteit Scheikunde van de Universiteit Utrecht



This work is part of the research programme of the ‘Stichting voor Fundamenteel Onderzoek der Materie (FOM)’, which is financially supported by the ‘Nederlandse Organisatie voor Wetenschappelijk Onderzoek (NWO)’.

ISBN 90-393-3484-6

Subject headings: colloid-polymer mixtures/phase and wetting behaviour/interface statics and dynamics/droplet coalescence and breakup.

Cover: Droplet snap-off, see chapter 8 (lay-out: Elise Beynon)

Contents

Chapter 1. Life at ultralow interfacial tension	1
1.1. Colloids	2
1.2. Colloid-polymer mixtures	3
1.3. Consequences of an ultralow interfacial tension	5
1.4. Scope of this thesis	7
Chapter 2. Introduction to the model colloid-polymer mixtures and experimental techniques	9
2.1. Introduction	9
2.2. System 1: SiO ₂ + PDMS in cyclohexane (SPC13)	10
2.3. Systems 2 and 3: PMMA + PS in decalin (PPD25 and PPD71)	12
2.4. Experimental technique	14
2.5. Conclusion	16
Appendix: physical properties of the model colloid-polymer mixtures	18
Chapter 3. Phase behaviour of mixtures of colloidal spheres and excluded-volume polymer chains	19
3.1. Introduction	19
3.2. Free volume theory	21
3.3. Ideal Polymers	23
3.4. Polymers with Excluded Volume Interactions	24
3.5. Results	25
3.6. Discussion and conclusion	28
Appendix: Depletion thickness for ideal polymers	30
Chapter 4. Interfacial tension and wetting behaviour in colloid-polymer mixtures: Theory	31
4.1. Introduction	31
4.2. Bulk phase behaviour	34
4.3. Interface	35
4.4. Colloid-polymer mixture near a hard wall	38
4.5. Conclusions	43
Appendix: Equation (4.19) for $q = 1$	45

Chapter 5. The capillary length and wetting behaviour in colloid-polymer mixtures:	
Experiment	47
5.1. Introduction	47
5.2. Experimental system and technique	49
5.3. Results	51
5.4. Analysis and discussion	54
5.4.1. Capillary lengths	54
5.4.2. Wetting behaviour	57
5.5. Conclusion	58
Chapter 6. Direct visual observation of thermal capillary waves	61
6.1. Introduction	61
6.2. Theoretical background	62
6.3. Experimental methods	67
6.4. Results and discussion	69
6.5. Conclusions	71
Chapter 7. Hydrodynamics of droplet coalescence	73
7.1. Introduction	73
7.2. Film drainage	75
7.3. Film breakup	80
7.4. Neck growth	83
7.5. Conclusion	87
Chapter 8. Droplet snap-off affected by thermal noise	89
8.1. Introduction	89
8.2. Experiment	91
8.3. Results	92
8.4. Concluding remarks	97
Appendix: Routine to track the snap-off of droplets	98
Chapter 9. Interfacial dynamics in demixing systems with ultralow interfacial tension	99
9.1. Introduction	99
9.2. Length- and timescales	100
9.3. Experimental system and method	103
9.4. Initial phase separation	104
9.5. Gravity driven flow	107
9.6. Macroscopic interface formation	109
9.7. Conclusion	110
Appendix: Real-space fluorescence recovery after photo-bleaching	112

CONTENTS	ix
Bibliography	115
Summary	123
Samenvatting voor iedereen	125
List of publications	129
Dankwoord	131
Curriculum Vitae	133

1

Life at ultralow interfacial tension

Interfaces are truly ubiquitous in nature. They play an important role in diverse areas ranging from the cell [1] to black holes [2]. Characteristic of an interface is its interfacial tension. Manifestations of the interfacial tension are observed in every day life: the spherical shapes of drops, the breakup of droplets from a dripping faucet, the meniscus in a glass of water etc. All these phenomena are a macroscopic demonstration of the forces between molecules, which has attracted the interest of scientists since the eighteenth century [3]. Great names of scientific history are associated with important breakthroughs: Laplace, Young, Lord Kelvin and many others. But it was van der Waals who gave the first modern thermodynamic description of the interface between a gas and a liquid at the end of the 19th century [4]. Although it has been questioned what we actually know more than van der Waals about the gas-liquid interface [5], other important theoretical discoveries are the thermal roughness of the interface as realized by Von Smoluchowski in 1908 [6], five years later described by Mandelstam [7] and rediscovered by Buff, Lovett and Stillinger in 1965 [8]. About ten years later wetting transitions in the interface at a wall were predicted independently by Cahn [9] and by Ebner and Saam [10].

In this thesis we will only discuss liquid-gas or fluid-fluid interfaces and not for example solid-gas interfaces. The magnitude of the interfacial tension ranges for atomic and molecular liquids at room temperature from 485 mN/m for mercury, 73 mN/m for water, to 13 mN/m for trimethylamine [11]. The interfacial tension γ is expressed in terms of a force per length or in terms of energy over area. The latter dimensions can be used to understand the following scaling relation for γ [3, 12],

$$\gamma \sim \frac{\epsilon}{d^2}, \tag{1.1}$$

with ϵ the strength of the molecular interaction (for example following from the Lennard-Jones potential) and d the characteristic length scale in the interface. Away from the gas-liquid critical point ϵ is one/two times the thermal energy $k_B T$ (with k_B Boltzmann's constant and T the absolute temperature) and d is of the order of the molecular diameter. For example, liquid argon at 84 K has an experimental interfacial tension of 13.4 mN/m, whereas the scaling relation (1.1) would give 14.6 mN/m using standard (12,6) Lennard-Jones potential parameters of $\epsilon/k_B = 124$ K and $d = 0.342$ nm, the diameter of an argon atom [13]. Close to the critical point the characteristic length becomes very large and the interfacial tension vanishes. In principle, the interfacial tension can become ultralow. To study the consequences of such ultralow interfacial tensions one could therefore use systems that are very close to the critical point, but here we will follow a different approach, namely by directly increasing the typical size d . This is done by using colloid-polymer mixtures and brings us to the topic of this thesis: The study of the behaviour and of the properties of interfaces with an ultralow interfacial tension.

In this chapter we will introduce colloids in section 1.1 and colloid-polymer mixtures in section 1.2. In section 1.3 an outlook is given of the possible consequences the ultralow interfacial tension may have and the scope of the thesis is presented in section 1.4.

1.1. COLLOIDS

“The term colloidal refers to a state of subdivision, implying that the molecules or polymolecular particles dispersed in a medium have at least in one direction a dimension roughly between 1 nm and 1 μ m, or that in a system discontinuities are found at distances of that order.”

The above definition for the term *colloidal* is given by the International Union of Pure and Applied Chemistry (IUPAC). It sets the size of a colloidal particle in the submicrometer lengthscale -a very relevant lengthscale in many biological systems-, whereas atoms are typically subnanometer. A collection of colloidal particles in a solvent is called a colloidal suspension. The size of the colloids is such that the effect of gravity on the particles is balanced by thermal energy. Hence, the colloids diffuse by means of Brownian motion and probe the complete vessel. Since the number of colloids in a suspension is easily of the order of 10^{15} , these suspensions are ideal model systems in the study of statistical mechanics [14–16].

The intrinsic length-scale of the colloids has several important consequences and the main advantages over atoms or molecules is that colloids are “slow, soft and see-able” [17]. They are slow, since the diffusion coefficient is several orders of magnitude smaller than the molecular one. They are soft, since they respond to small external

forces and even thermal fluctuations. And they can be made visible with optical techniques such as light microscopy, since their size is comparable to the wavelength of light, first fully exploited by Perrin [15,16]. Finally, their interactions can be tuned for example by changing the solvent, the solvent properties (e.g. the ionic strength) or by adding a third component (see section 1.2).

1.2. COLLOID-POLYMER MIXTURES

As mentioned above the colloid-colloid interaction can be varied by adding a third component to the colloidal suspension. In the work described in this thesis the third component is a polymer particle. This modifies the colloid-colloid interaction in such a way that in principle three different phases can (co-)exist [18]; a colloid poor-polymer rich phase, a colloid rich-polymer poor phase, and an ordered colloid rich-polymer poor phase. If we consider only the colloids then the first phase resembles a gas, the second a liquid and the third a crystal phase [19]. Here we will explore the properties of coexisting colloidal gas-colloidal liquid phases, hereafter simply called gas-liquid phase coexistence.

In order to obtain a gas-liquid phase separating system the colloid-colloid interaction must have an attractive minimum comparable to the thermal energy $k_B T$, whereas the range of the attraction must be of the order of the colloidal diameter σ_c [19]. In theory, it is straightforward to calculate what properties a suspension of only colloidal particles must have in order to obtain a gas-liquid phase separation [20]. The colloids interact

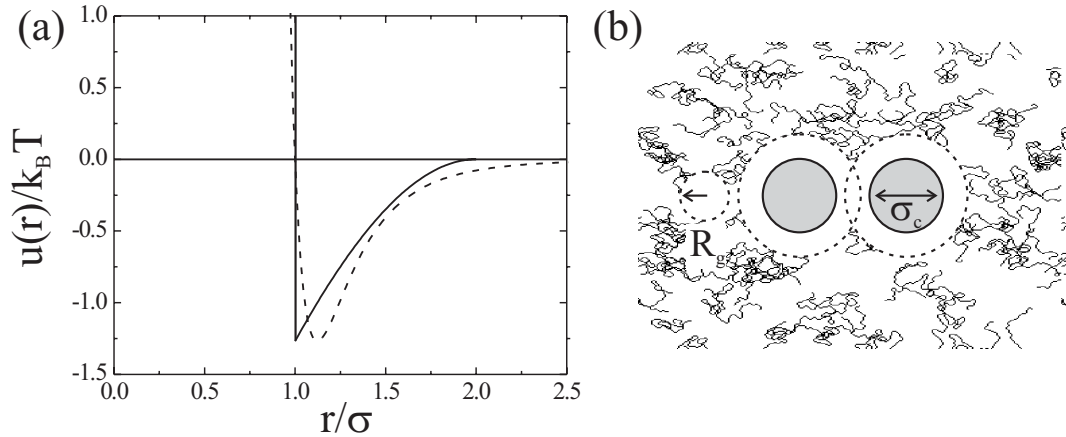


FIGURE 1.1. (a) Pair potential between two colloids in a sea of (ideal) polymers [19] (full curve) and between two argon molecules (dashed curve) interacting through a (12,6) Lennard-Jones potential [13]. The depth of the attractive minimum is fixed and set equal. (b) Two colloids with diameter σ_c in a sea of polymers with radius of gyration R_g . No polymer is present in the depletion zones around the colloids.

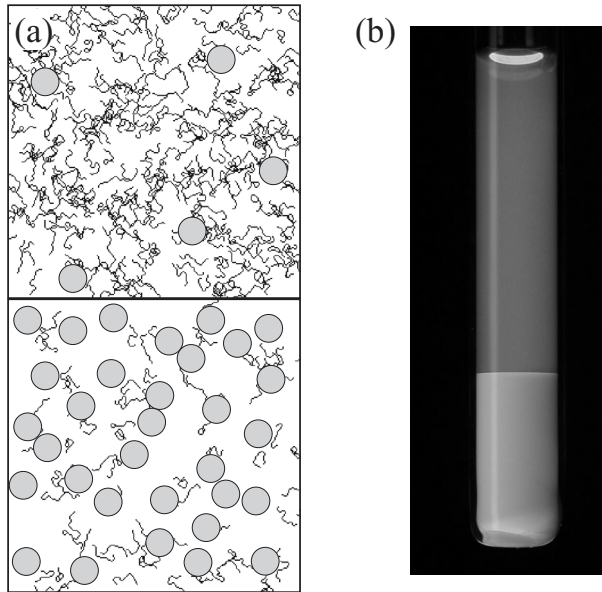


FIGURE 1.2. (a) Schematic representation of coexisting colloid-rich or liquid (bottom) and colloid-poor or gas (top) fluid phases. In (b) a photograph of a phase separated mixture of fluorescently labelled PMMA colloids and poly(styrene) polymer in decalin is shown, which has been taken under UV-light. The very sharp interface can be clearly seen.

through a DLVO potential [21, 22], named after its originators Derjaguin, Landau, and independently Verwey and Overbeek, which has a (secondary) attractive minimum at reasonable distances from the colloid's surface. In the laboratory, however, a DLVO potential that leads to gas-liquid coexistence, is hard to realize, although possible [23]. Upon the addition of polymer the required potential is obtained rather easily [19] as can be seen in figure 1.1(a). Here, the pair potential of two colloids in a sea of polymers is compared to that of two argon atoms, where we observe that the shapes are rather similar.

The origin of the gas-liquid phase separation in colloid-polymer mixtures lies in the entropy-driven attraction between the colloids mediated by the polymers. This interaction was first described by Asakura and Oosawa [24, 25] and later independently by Vrij [19]; a polymer coil is entropically excluded from a region around a (colloidal) surface, which is called the depletion zone. If two such depletion zones overlap there is an osmotic imbalance pushing the particles together, see figure 1.1(b). If the concentrations of both species are large enough a fluid-fluid (i.e. gas-liquid) demixing transition may occur [19] of which the resulting phases are shown in figure 1.2, schematically as well as in an actual sample. This transition is widely accepted to be the analogue of gas-liquid phase separation in molecular systems (see for example [26]). The thickness of the depletion zone depends on the size and hence the molecular mass of the polymer, whereas the strength of the attraction depends on the polymer concentration.

Thus, all interactions are tunable. In addition, the colloid-polymer size ratio sets the general phase behaviour as shown in the work of Gast *et al.* [27] and Vincent and co-workers [28, 29]. Furthermore, the polymer partitioning over the phases as well as the existence of a three-phase region was first addressed by Lekkerkerker [30] and described within free volume theory [18]. Recent years have shown a focus on several issues; an exact statistical mechanical description of colloid-polymer mixtures and –closely related– the interface and wetting behaviour of such mixtures (see e.g. the review of Brader, Schmidt and Evans [31]). Another issue is that of a more realistic description of the polymers beyond penetrable hard spheres (see the reviews of [26, 32–34]).

1.3. CONSEQUENCES OF AN ULTRALOW INTERFACIAL TENSION

The interface of a gas-liquid phase separated colloid-polymer mixture is very sharp as can be seen in figure 1.2(b). As with molecular interfaces there is an interfacial tension associated with this interface [3, 12]

$$\gamma \sim \frac{\epsilon}{d^2} \sim \frac{k_B T}{\sigma_c^2}, \quad (1.2)$$

where since the attraction is entropic, ϵ is of the order of $k_B T$. Furthermore, away from the critical point the typical size d is similar to the colloid diameter σ_c . This leads to ultralow values for the interfacial tension of $1 \mu\text{N/m}$ and below as first measured by Vliegthart and Lekkerkerker [35], de Hoog and Lekkerkerker [36, 37], and Chen *et al.* [38]. The ultralow interfacial tension has several important consequences concerning both the static and dynamic interface behaviour.

For example, the static properties of the interface are directly affected. At rest the interface between any two fluids appears to be smooth. Yet thermal motion inevitably gives rise to statistical fluctuations of the local interface position, leading to a rough interface [6, 7]. The mean interface roughness L_T is proportional to [7]

$$L_T = \sqrt{\frac{k_B T}{\gamma}}, \quad (1.3)$$

where we see that if γ is a million times smaller, L_T is a thousand times larger. The correlation length L_{\parallel} along the interface, i.e. the range over which a disturbance reaches, is given by [7]

$$L_{\parallel} = \sqrt{\frac{\gamma}{g\Delta\rho}} \equiv L_c, \quad (1.4)$$

with g earth's acceleration and $\Delta\rho$ the mass density difference between the two phases. It is equal to the capillary length L_c , which also sets the typical length scale of a fluid interface close to a wall (i.e. the meniscus) [39]. Here, an ultralow interfacial tension decreases the capillary length strongly, which explains why the interface between the colloidal liquid and colloidal gas phase appears to be flat close to a wall, see figure 1.2(b).

TABLE 1.1. Characteristic numbers in a typical molecular system (water/air) (left) and in a colloidal system (right).

			water-air	colloidal
interfacial tension	γ	(N/m)	10^{-1}	10^{-7}
viscosity	η	(Pa s)	10^{-3}	10^{-2}
density difference	$\Delta\rho$	(kg/m ³)	10^3	10^3
roughness	$L_T = L_\perp$	(m)	10^{-10}	10^{-7}
capillary length	$L_c = L_\parallel$	(m)	10^{-3}	10^{-5}
capillary velocity	u_c	(m/s)	10^2	10^{-5}
capillary time	τ	(s)	10^{-5}	10^0
viscous length	L_η	(m)	10^{-8}	10^0
viscous time	t_η	(s)	10^{-10}	10^5

It can be illuminating to indicate the thermal length with L_\perp to put it into perspective with the correlation length L_\parallel along the interface.

The dynamic properties of the interface are affected as well. The interface dynamics are described by the Navier-Stokes equations [40]

$$\rho D_t \mathbf{u} = \eta \nabla^2 \mathbf{u} - \nabla p, \quad (1.5)$$

with ρ the mass density, D_t the material derivative (which denotes $\partial/\partial t + \mathbf{u} \cdot \nabla$), \mathbf{u} the velocity, η the viscosity and p the pressure. The term on the left hand side captures the inertial force, the first term on the right hand side the viscous force and the last term the (capillary) pressure force. The capillary velocity u_c is the characteristic velocity when inertia is unimportant and can be found by equating the capillary with the viscous force (see for example [41]):

$$u_c \equiv \gamma/\eta. \quad (1.6)$$

The relative importance of inertial vs. viscous forces can be found from the Reynolds number $Re \equiv \rho u L/\eta$ with L a characteristic lengthscale. With $u = u_c$ the Reynolds number becomes

$$Re = \frac{\gamma L}{\eta^2/\rho}, \quad (1.7)$$

which we write in this particular form to indicate that both γL and η^2/ρ are forces [42]. We see that inertial terms become important at lengths L_η , where $Re = 1$,

$$L_\eta = \frac{\eta^2}{\rho\gamma}, \quad (1.8)$$

and at times t_η

$$t_\eta = \frac{L_\eta}{u_c} = \frac{\eta^3}{\rho\gamma^2}. \quad (1.9)$$

An ultralow interfacial tension postpones the inertial hydrodynamic regime drastically as can be seen in table 1.1 and the system remains in the viscous hydrodynamic regime for much longer times. Hence, the left hand side of (1.5) is effectively zero, we end up with Stokes flow and observe that life at ultralow interfacial tension is equivalent to life at low Reynolds number [42]. The capillary velocity is the typical velocity in interface phenomena such as droplet coalescence and snap-off. Because of its small magnitude detailed observations in time are possible. Finally, the combination of capillary velocity and capillary length leads to a typical decay time τ of thermal capillary waves [43, 44]

$$\tau = \frac{L_{\parallel}}{u_c} = \frac{L_{\parallel}\eta}{\gamma}. \quad (1.10)$$

The characteristic units introduced in this section are summarised and quantified in table 1.1 and will appear frequently in the chapters ahead.

1.4. SCOPE OF THIS THESIS

In this thesis we will study the behaviour and the properties of interfaces with an ultralow interfacial tension concerning both the statics and dynamics. The contents can be roughly divided into two parts. In the first part we will deal with statics, the second part discusses dynamics. We will describe the colloid-polymer mixtures and the microscopy setup that have been used in this work in chapter 2. In order to minimize repetition the systems are hardly discussed in the other chapters. This chapter will be followed by two theoretical chapters; a calculation of the phase behaviour of mixtures of colloids and interacting polymers (chapter 3), which is an extension of the free volume theory developed for mixtures of colloids and ideal polymers [18], and in chapter 4 the theory is further extended to calculate the interfacial tension and the wetting behaviour. This theoretical work was motivated by our first experiments on a mixture of silica colloids and poly(dimethyl) siloxane in cyclohexane, but will be applied to other experimental systems as well. In the subsequent chapters theory and experiment are interwoven. The system is studied in the vicinity of a single wall in chapter 5 (L_c) with a focus on capillary lengths and the wetting state of the system ¹. Both the statics and dynamics of the free interface are studied in chapter 6 (L_{\perp} , L_{\parallel} and τ). The dynamic interface roughness plays a key-role in droplet coalescence, which is the topic of chapter 7 (L_{η} , L_T , u_c), and also in droplet snap-off described in chapter 8 (L_{η} , L_T , u_c), where we see first experimental evidence of the effects of thermal noise in droplet snap-off. The dynamic part ends with a description of phase separation kinetics and morphology in demixing colloid-polymer mixtures (chapter 9 (u_c and L_c)), where many aspects of the previous two chapters come together. A summary (also in Dutch) will follow and that will conclude this thesis.

¹The experimental key-parameters in the chapters are between brackets.

2

Introduction to the model colloid-polymer mixtures and experimental techniques

ABSTRACT

The three different colloid-polymer mixtures used in this thesis and the experimental techniques to study them are introduced and described in detail. The first system consists of stearyl coated silica colloids + poly(dimethylsiloxane) polymer in cyclohexane and the other two consist of fluorescently labelled poly-(methylmethacrylate) spheres + poly(styrene) polymer in decalin. The diameter of the colloids has been determined using dynamic and static light scattering techniques and transmission electron microscopy. Furthermore, densities and rheological properties of polymers and colloids as well as mixtures have been determined. Phase diagrams have been constructed by preparing several dilution lines. As techniques we used transmission light and laser scanning confocal microscopy, which setups and properties are described as well.

2.1. INTRODUCTION

Finding a good model system can be a difficult process. Many factors have to be dealt with; first of all, the yield of particle synthesis should be considerable so that a minimum of about 10 ml of 40 volume % colloids can easily be obtained. Separately, both colloids and polymers should be stable in the solvent and mixed together the polymer must be non-adsorbing. The colloid index of refraction should not differ too much from the solvent index of refraction in order to allow light microscopy and at the same time minimize van der Waals attractions. Furthermore, the buoyancy of the colloids has to be such that the chemical potential hardly changes over one particle diameter σ_c along the direction of gravity, i.e. σ_c/l_g should be much smaller than one.

Here, l_g is the gravitational length of the particles defined as $k_B T / m^* g$ with $k_B T$ the thermal energy, m^* the buoyant mass of the colloids and g earth's acceleration. The colloids should be small enough such that the interfacial tension is still considerable (see (1.2)) and capillary forces are important with respect to for example hydrostatic forces. Moreover, a sufficiently large polymer must exist to induce gas-liquid phase separation, i.e. the polymer-colloid size ratio should as a rule of thumb be at least 1/3 [18].

To this end, three different colloid-polymer mixtures have been explored to which we will refer throughout this thesis. In section 2.2 a mixture of stearyl-coated silica spheres+poly(dimethylsiloxane) in cyclohexane will be discussed, which has been developed in the van 't Hoff laboratory in Utrecht, the Netherlands, over quite some period of time [36, 37, 45–47]. In section 2.3 two different poly(methylmethacrylate) colloidal spheres + poly(styrene) polymer in decalin will be shown, which has proven to be extremely useful especially by the Edinburgh-group, United Kingdom, see for example [48–55]. The microscopy setups will be discussed in section 2.4. In section 2.5 a verdict over the systems will be returned.

2.2. System 1: SiO₂ + PDMS IN CYCLOHEXANE (SPC13)

This system was originally prepared by Verhaegh *et al.* [45]. The colloids are commercially available ludox spheres (Ludox AS 40 % Dupont) coated with stearyl alcohol (1-octadecanol, Merck, zur synthesis) providing steric stabilisation [56]. The (dynamic light scattering) radius R_c of the particle was 13 nm with a polydispersity of 19 % and the density was 1.60 g/ml [36, 47]. The molecular weight M_w of the poly(dimethylsiloxane) polymers (PDMS, Janssen) was 91.7 kg/mol ($M_w/M_n = 1.9$, with M_n the number average molecular weight) and the density was 0.976 g/ml. The polymer's radius of gyration was determined at 14 nm [36, 47]. A calculation of R_g following Vincent [57] gives 14.1 nm, in good agreement with the measured radius. The θ -temperature for PDMS in cyclohexane is -80°C [58], so the polymer is in a good solvent. No signs were found that the polymer adsorbed on glass walls.

Samples were prepared in several types of optical cuvettes by mixing colloid- and polymer-stock dispersions and diluting with cyclohexane. Since all densities are known, mass fractions can be directly converted to volume fractions of colloids, $\phi_c = \frac{4}{3}\pi R_c^3 n_c$, and of polymers, $\phi_p = \frac{4}{3}\pi R_g^3 n_p$, where n_c and n_p are the number densities of colloids and polymers, respectively. After preparing a colloid-polymer mixture, the system is homogenized either by hand or with a vortex, which is a reproducible way of homogenizing the mixture, although the degree of homogenization is unclear [45]. By visual inspection one learns that the sample immediately becomes turbid if it is in the unstable region. After 5 s for samples away from the critical point up to 30 s for sample close to the critical point gravity starts driving the phases apart leading to strong flow in the system. Gradually a macroscopic interface is formed after 6-7 minutes for samples

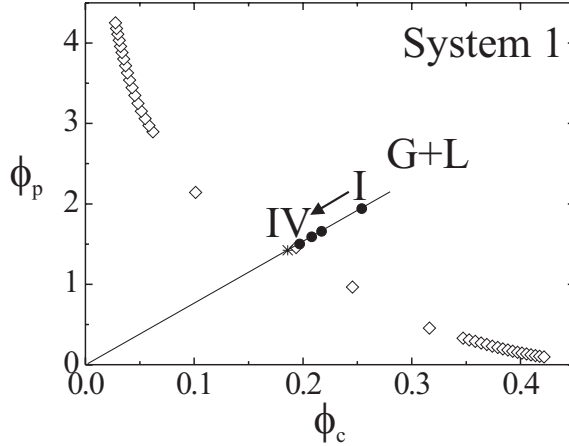


FIGURE 2.1. Experimental phase diagram of a mixture of silica colloids and poly(dimethylsiloxane) polymer with $q = 1.08$ [36]. The diamonds denote the binodal, the points I-IV on the dilution line (drawn line) are studied in more detail in the upcoming chapters. Filled circles are in the two phase region, the cross is in the one phase region. System 1 SPC13.

away from and 13-14 minutes for samples close to the critical point. It takes, however, still one up to several hours before most of the drops have coalesced with their bulk phases [59]. An elaborate study of phase separation kinetics and morphology in colloid-polymer mixtures is presented in chapter 9.

De Hoog and Lekkerkerker determined the binodal and the tie-lines of this system [36] following the approach of Bodnar and Oosterbaan [60], which is based on measurements of the relative amounts of coexisting gas and liquid phases. The phase diagram is shown in figure 2.1. We will make the comparison with theory in chapter 3, figure 3.5(d). In principle, the polymer-colloid size ratio $q = R_g/R_c = 1.08$ allows for the observation of gas, liquid and crystal phases [18], but only gas-liquid phase coexistence was observed. Fluid-crystal coexistence was possibly suppressed by the polydispersity of the spheres as is often the case in systems with small spheres and the system gelled at relatively high polymer concentrations. This observation can be related to theoretical predictions, which show that both sphere and polymer polydispersity favour gas-liquid coexistence and delay the onset of fluid-solid separation [61–64]; These predictions are valid for ideal polymers, but similar effects have been calculated for interacting, polydisperse polymer chains on the level of gas-liquid phase separation [65]. Furthermore, de Hoog and Lekkerkerker extensively characterised the system and measured the viscosities of the gas and liquid phases [36]. The viscosity of the liquid phase is of the order of 100 mPas and of the gas phase 10 mPas, see the Appendix of this chapter. In addition, they measured the interfacial tension using the spinning drop technique and by following the

breakup of a gas cylinder surrounded by liquid [36,37,66]. They measured an interfacial tension of a few $\mu\text{N}/\text{m}$, as will be discussed in more detail in chapter 5.

Please note that we will refer throughout this thesis to this system as system 1 with the system's characteristics as SPC13, i.e. Silica Poly(dimethylsiloxane) in Cyclohexane with the radius of the colloid equal to 13 nm. A summary of the physical properties of this system can be found in the Appendix of this chapter.

2.3. Systems 2 and 3: PMMA + PS IN DECALIN (PPD25 AND PPD71)

Two different poly(methylmethacrylate) PMMA-colloids + poly(styrene) polymer systems were used. The first system of fluorescent PMMA spheres was prepared together with my colleague Roel Dullens. We followed the method of Bosma *et al.* [67] slightly modified by using decalin (Merck, for synthesis) as reaction solvent. The fluorescent dye is 4-methylaminoethylmethacrylate-7-nitrobenzo-2-oxa-1,3-diazol. The (dynamic light scattering) radius R_c was 25 nm and the polydispersity was less than 10%, estimated from scanning electron microscopy images, see figure 2.2. As polymer commercially available poly(styrene) (PS, Fluka) was used with a molecular weight of $M_w = 233 \text{ kg mol}^{-1}$ ($M_w/M_n = 1.06$) and a radius of gyration R_g of $\sim 14 \text{ nm}$ (estimated from data in the literature [57, 68]). The colloidal particles of the second PMMA system, i.e. system 3 in this thesis, were prepared by Gilles Bosma [69]. The same dye was incorporated. The (static light scattering) radius R_c was 71 nm and the polydispersity was around 10%. As depletant polystyrene polymer (Fluka) with a molecular weight

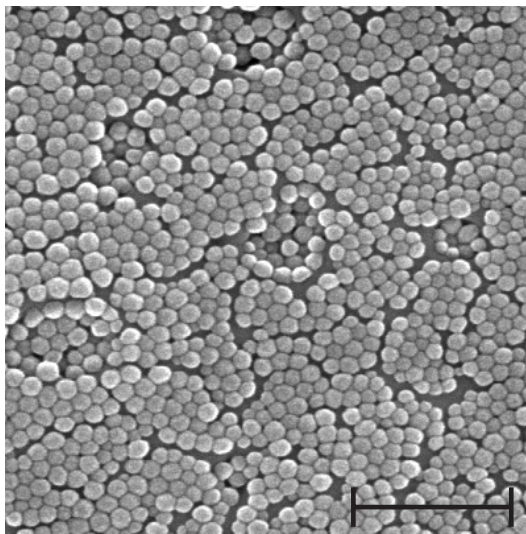


FIGURE 2.2. Scanning electron microscopy image of PMMA spheres with a radius of 25 nm. The scale bar is 500 nm. System 2 PPD25.

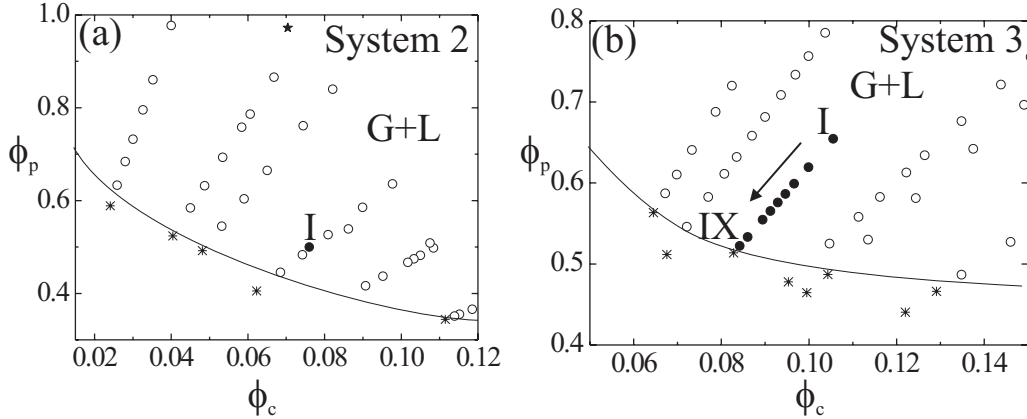


FIGURE 2.3. Experimental phase diagrams of a mixture of PMMA colloids and PS polymer in decalin with (a) $q = 0.56$ (System 2 PPD25) and (b) $q = 0.6$ (System 3 PPD71). Indicated are state points where gas-liquid phase separation occurs (circles), state points in the one-phase region (crosses) and state points where the system gelled (stars). The lines are an estimate of the binodal and are drawn to guide the eye. State points to which references are made in the text are indicated (solid circles and Roman numbers).

of $M_w = 2000 \text{ kg mol}^{-1}$ ($M_w/M_n < 1.2$) has been used; the polymer's radius of gyration is estimated to be 43 nm from data in the literature [57, 68]. The decalin is a mixture of 40 % cis and 60 % trans decalin. The θ -temperature of polystyrene in this solvent is about 16.5°C [68], which means that the polymer is clearly not in the full excluded volume interaction limit, see chapter 3. In fact, Martelozzo *et al.* have used the temperature dependence of the polymer's radius of gyration cleverly to steer the phase behaviour [70]. The samples have been prepared in a similar manner as described above (section 2.2). Mass fractions were directly converted to volume fractions of colloids, $\phi_c = \frac{4}{3}\pi R_c^3 n_c$, and of polymers, $\phi_p = \frac{4}{3}\pi R_g^3 n_p$, after the densities of the species were measured with an Anton-Paar density metre. The first PMMA system did not display a crystal phase and volume fractions have not been scaled on the freezing volume fraction as for example done in [71]. For the second PMMA system the same procedures have been followed as for the first PMMA system. Similar behaviour compared to system 1 SPC13 was observed, although phase separation was on average a bit slower. For the first PMMA system it took at high polymer concentrations a few hours before the system phase separated completely, at intermediate concentrations about 15 minutes and very close to the binodal again up to hours. For the second PMMA system with larger spheres and hence a smaller interfacial tension, phase separation took at least one hour, but never more than one day. Again, the polymer-colloid size ratios $q = 0.56$ for the first and $q = 0.6$ for the second PMMA system allow for the observation of gas, liquid and crystal phases [18]. Only gas-liquid phase coexistence

was observed, see figure 2.3(a) and (b) for the phase diagrams, and the systems gelled at relatively high polymer concentrations.

The theoretical binodal of the first PMMA system will be shown in chapter 3, figure 3.5(b). Unfortunately, the method to determine the binodal and tie-lines as proposed by Bodnar and Oosterbaan [60] did not give physically acceptable results. Thus, the gas-liquid density difference cannot be found directly from the phase diagram and more direct methods have to be used. We determined densities with an Anton-Paar density metre, which requires rather much material (about 1 ml per phase). We obtained density differences in the range of 50 to 100 g/l in both PMMA systems for systems at a moderate distance and away from the critical point. Furthermore, in both systems, viscosities are of the order of 10 and 40 mPas for the gas and liquid phases, respectively, and interfacial tensions are of the order of 200 for the first and 50 nN/m for the second PMMA system. Of course, the interface properties are the topic of the thesis and the mentioned values are only indicative.

Throughout this thesis we will refer to the first PMMA system as system 2 with the system's characteristics as PPD25, i.e. PMMA Poly(styrene) in Decalin with the radius of the colloid equal to 25 nm. The second PMMA system is referred to as system 3 or PPD71, i.e. PMMA Poly(styrene) in Decalin with the radius of the colloid equal to 71 nm. A summary of the physical properties of these systems can be found in the Appendix of this chapter.

2.4. EXPERIMENTAL TECHNIQUE

To study the colloid-polymer mixtures we used the following setup, schematically shown in figure 2.4(a). A transmission light microscope (Nikon Eclipse E400) was placed horizontally. The setup allows for monitoring using transmission light microscopy as well as laser scanning confocal microscopy (LSCM). In the transmission mode a CCD camera can be attached, which has a maximal capturing rate of 50 frames per second. In the LSCM mode a confocal scanning laser head (Nikon C1) was mounted on the microscope with a maximal capturing rate of about 1 full frame per second. The main advantage of confocal over standard (transmission light) microscopy is the considerable increase of contrast. In addition, the resolution is slightly improved in confocal microscopy as first realized by its inventor Minsky [72]. These improvements are reached by using a pinhole before the detector that blocks most of the out-of-focus signal. A schematic setup of confocal microscopy is shown in figure 2.5(a) [73]. Light from a point source (for example created by placing an extra (source) pinhole in front of the actual light source) is focussed by the objective lens onto a spot in the sample, the scattered light is collected by the collector lens and detected by e.g. a photo multiplier tube. The objective and collector lens are usually the same (which is cost effective). The sample is scanned point-per-point.

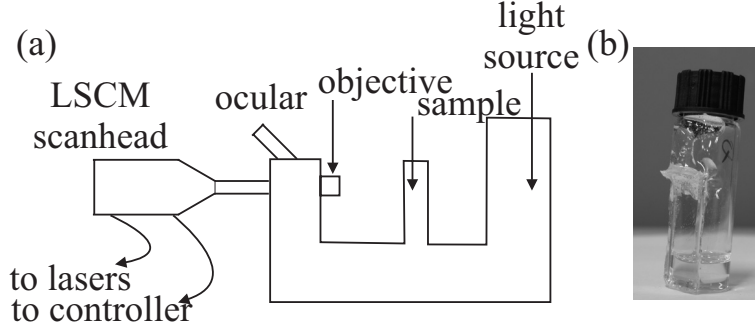


FIGURE 2.4. (a) Schematic microscopy setup. Either in the LSCM-mode or in the transmission light microscopy mode. (b) One of the types of cuvettes used. The front glass wall is 0.17 mm thick.

To quantify the advantages of confocal over standard microscopy we will follow the review of Webb [73] (for similar treatments see [74, 75]) and study the point spread function (PSF). The PSF for confocal microscopy can be viewed as the probability that a photon will reach a certain point or that it will be received from that point [73]. First, we switch from real coordinates around the optical axis, i.e. r (radial) and z (axial), to optical coordinates, $\rho = r \, 2\pi\text{NA}/\lambda$ and $\zeta = z \, 2\pi\text{NA}^2/n\lambda$, where NA is the numerical aperture, λ the wavelength of the light in vacuum, and n the index of refraction of the medium. The numerical aperture describes the angular behaviour of the light cone passing through the objective lens [73]. The PSF, $p(\rho, \zeta)$, is given by

$$p(\rho, 0) = \left(\frac{2J_1(\rho)}{\rho} \right)^4, \quad (2.1)$$

in the plane perpendicular to the optical axis (radially) with J_1 the Bessel function of the first kind and

$$p(0, \zeta) = \left(\frac{\sin(\zeta/4)}{\zeta/4} \right)^4, \quad (2.2)$$

along the optical axis (axially). Both equations are simply the square of the PSF's of standard microscopy. The standard microscopy variant of (2.1) defines the Airy disc, which is where the PSF first drops to zero ($p(\rho_{\text{airy}}, 0) = 0$), see also figure 2.5(b). If another similar source would be positioned at the Airy disc, then the intensity in between would drop 26 % in standard microscopy (figure 2.5(b)), which defines the Rayleigh criterion and we use this criterion to calculate the resolution. The radial resolution (in ρ) is 3.82 for standard and 2.76 for confocal microscopy, whereas the axial resolution (in ζ) is 13.12 for standard and 9.53 for confocal microscopy. In the work described in this thesis we frequently use a lens with $\text{NA} = 1.4$, a system with $n \approx 1.5$ and a laser light source with $\lambda = 488 \text{ nm}$, which leads to radial resolutions of 212 nm and 153 nm and axial resolutions of 780 and 566 nm, for standard and confocal microscopy, respectively. Although the improvement is significant the main advantage

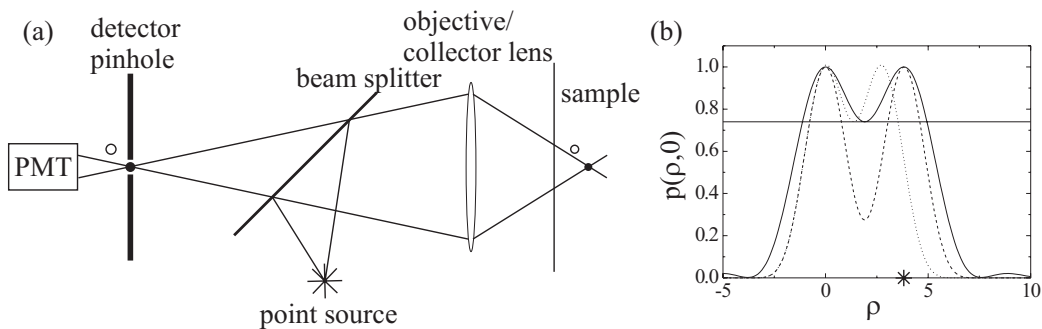


FIGURE 2.5. (a) Schematics of the optics of a confocal microscope. The filled circle is in focus and is imaged in the detector pinhole in contrast to the open circle. [73] (b) Radial PSF's for standard microscopy (full curve) and confocal microscopy (broken curves) of two similar point sources. The star at the horizontal axis denotes the Rayleigh distance. The dashed curve shows the considerable contrast improvement in confocal microscopy. The dotted confocal microscopy curve fulfills the Rayleigh criterion (i.e. the horizontal line) at smaller separations leading to an improved resolution. PSF plots in the axial direction show a similar trend.

is that of the increased intensity contrast; for example, at the secondary PSF maximum of a single scatterer the signal is radially about sixty and axially about twenty times smaller in confocal microscopy than in standard microscopy. As a result the signal-to-noise ratio is improved considerably, which makes it possible to discriminate between bright and dim scatterers in close proximity of each other.

Besides thin glass capillaries, several types of glass cuvettes have been used in the microscopy setups, such as light microscopy Hellma cuvettes with path lengths varying between 1 to 5 mm. Special cuvettes were fabricated in the glass workshop, see figure 2.4(b). These cuvettes have several advantages over the ready-to-use Hellma cuvettes; they are cheap and airtight, yet can be opened and closed easily. Moreover, the front glass wall is only 0.17 mm thick allowing the use of high numerical aperture oil-immersion objectives, and it is easy to build all kinds of pedestals inside such cuvettes.

2.5. CONCLUSION

As will become clear throughout this thesis the three systems each bring their own advantages. In the silica system, system 1 SPC13, the interfacial tension is relatively high and this allows studying certain hydrodynamic effects, such as droplet coalescence and snap-off, in great detail with a practical length- and timescale. The first PMMA system with small colloids, system 2 PPD25, will prove to be very useful in the investigation of wetting behaviour, droplet coalescence and spinodal decomposition. Finally, even the thermal capillary waves of the “free” interface could be directly observed, but for this

study the second PMMA system, system 3 PPD71, was more convenient, because the interfacial tension is even lower than in system 2 and the roughness is therefore much larger. This last system allows studying not only the hydrodynamic effects in droplet coalescence, but also the stochastic effects of capillary waves. However, in studying spinodal decomposition or wetting behaviour the relevant lengthscales become too small. System 1 SPC13 is solely investigated with light microscopy, since the colloids are non-fluorescent. With light microscopy we can record very fast, but sometimes it leads to blurry images. Systems 2 PPD25 and 3 PPD71 are mainly studied with LSCM, but this technique records too slow to follow for example the details of droplet coalescence in time. Therefore, light microscopy was used in these systems as well. Moreover, the optical sectioning of LSCM sometimes obscures events, since these might evolve in or out of focus. Clearly, the transmission light and laser scanning confocal techniques are complementary.

Thus, we may conclude that the three different colloid-polymer mixtures and the two optical techniques have their own advantages and this will be exploited to explore an extensive range of fundamental questions about the static and dynamic interface behaviour of systems with an ultralow interfacial tension.

APPENDIX: PHYSICAL PROPERTIES OF THE MODEL COLLOID-POLYMER MIXTURES

TABLE 2.1. Summary of the physical properties of the model colloid-polymer mixtures. Viscosities of the liquid and gas phases are denoted by η_L and η_G , respectively.

System 1 SPC13					
		radius (nm)	density (g/ml)	M_w (kg/mol)	refractive index
colloid	silica	13	1.60		1.44
polymer	PDMS	14	0.976	91.7	
solvent	cyclohexane		0.78		1.43
ϕ_c	ϕ_p	$\Delta\rho$ (g/ml)	η_L (mPa/s)	η_G (mPa/s)	γ ($\mu\text{N/m}$)
0.24	1.57	0.242	97.1	8.4	~ 2 [36]
System 2 PPD25					
		radius (nm)	density (g/ml)	M_w (kg/mol)	refractive index
colloid	PMMA	25	1.17		1.5
polymer	PS	14	1.05	233	
solvent	decalin		0.88		1.48
ϕ_c	ϕ_p	$\Delta\rho$ (g/ml)	η_L (mPa/s)	η_G (mPa/s)	γ ($\mu\text{N/m}$)
0.076	0.50	0.053	31	8	0.16
System 3 PPD71					
		radius (nm)	density (g/ml)	M_w (kg/mol)	refractive index
colloid	PMMA	71	1.17		1.5
polymer	PS	43	1.05	2000	
solvent	decalin		0.88		1.48
ϕ_c	ϕ_p	$\Delta\rho$ (g/ml)	η_L (mPa/s)	η_G (mPa/s)	γ ($\mu\text{N/m}$)
0.11	0.65		30	12.6	0.1
0.15	0.70	0.096			

3

Phase behaviour of mixtures of colloidal spheres and excluded-volume polymer chains

ABSTRACT

We study the phase behaviour of mixtures of colloidal spheres and polymers that have an excluded volume interaction dispersed in a (background) solvent using the concept of free volume theory. The depletion layer thickness is calculated from the negative adsorption of polymer segments around a sphere. The correlation length and thermodynamic properties of the excluded volume interacting polymer chains in solution are taken into account by using results from the renormalization group theory. For small polymer-colloid size ratios the difference with an ideal description of the polymers is small, while for larger size ratios the gas-liquid coexistence region shifts in the direction of higher polymer concentrations and at the same time the liquid-crystal coexistence region becomes more extended. Both the gas-liquid region and the gas-liquid-crystal region become less extended. These features are compared to experiment.

3.1. INTRODUCTION

Mixtures of colloids and non-adsorbing polymers display a rich phase behaviour, involving colloidal “gas” (poor in colloid, rich in polymer), colloidal “liquid” (rich in colloid, poor in polymer) and colloidal “crystal” phases (rich in colloid, poor in polymer). This phase behaviour finds its origin in the interaction between colloidal particles in a sea of polymers. Between two particles the interaction was first described by Asakura and Oosawa [24, 25], Vrij [19] and Joanny *et al.* [76] who showed that there is an osmotic imbalance pushing the particles together if they are within a certain distance of each other. Subsequent calculations for the phase behaviour of colloidal spheres and

polymers in a “background” solvent based on perturbation approaches were performed by Gast *et al.* [27] and Vincent and co-workers [28, 29]. These approaches successfully identified that the topology of the phase diagram depends on the polymer to colloid size ratio $q = R_g/R_c$, with R_g the polymer’s radius of gyration and R_c the radius of the colloid. For a concise review of this early work, see [77]. In these approaches the polymer partitioning between coexisting phases was not taken into account. This issue was first addressed by Lekkerkerker [30] and developed using the concept of *free volume theory* [18]. It is especially successful in understanding why one should find a three phase coexistence *region* instead of a three phase coexistence *line*. Extensive computer simulations [78–80] and exact solutions in one dimension [81–83] validate the free volume approximation. It qualitatively and for polymers much smaller than the colloids even quantitatively predicts the correct phase behaviour as can be seen by comparison with experiments [48–52]. The main limitation of the original free volume approach is that it considers the polymers as ideal. Recently, other theoretical approaches to describe colloid-polymer mixtures were explored aiming at a better description of the polymer [84–87] (for a review, see [88]). In this chapter we extend the free volume theory to describe the phase behaviour of mixtures of colloidal spheres and polymer chains with excluded volume interactions. This work was originally motivated by the observed large discrepancy between the theoretical binodal, which was calculated using free volume theory for ideal polymers [18], and the experimental binodal for a colloid-polymer mixture of stearyl coated silica particles and poly(dimethylsiloxane) polymer in cyclohexane [36], i.e. system 1 SPC13 described in chapter 2. We will also make the comparison with system 2 PPD25, whereas system 3 PPD71 shows similar results.

In section 3.2 we will briefly explain the thermodynamic framework needed to calculate the phase behaviour using the free volume theory. The theory for ideal polymers and colloidal spheres of Lekkerkerker *et al.* [18] and the resulting phase diagrams will be discussed in section 3.3. In this approach polymers are modelled as penetrable hard spheres with a radius R_g . Therefore, the polymers are ideal and the depletion layer thickness around a colloid Δ is equal to R_g . However, when using the polymer density profile around a sphere [89, 90] and replacing this profile by a step function, Δ becomes a function of the curvature q ($= R_g/R_c$) as will also be shown in section 3.3. In section 3.4 we make the transition from ideal polymers to polymers with excluded volume interactions using results from Renormalization Group (RG) theory [91]. We will use an expression from Hanke *et al.* [92] to incorporate curvature effects. In section 3.5 the resulting phase diagrams are presented and compared to the original free volume theory and to experimental phase diagrams. We will summarize and conclude our findings in section 3.6.

3.2. FREE VOLUME THEORY

The natural thermodynamic potential to use when calculating the phase behaviour of colloid-polymer mixtures is the semi-grand canonical potential [30]. The colloids are treated canonically, while the polymers are treated grand canonically as is schematically shown in figure 3.1. The solvent is treated as background. The semi-grand canonical potential $\Omega(N, T, V, \mu_p)$ can be written as

$$\Omega(N, V, T, \mu_p) = F(N, V, T) - \int_{-\infty}^{\mu_p^r} N_p d\mu_p^{r'}, \quad (3.1)$$

in which $F(N, V, T)$ is the Helmholtz free energy of a pure hard sphere dispersion and depends on the number of colloidal particles N , the system volume V and the temperature T . The reservoir is filled with polymers up to a final chemical potential of polymers μ_p^r , resulting in N_p polymers being pushed into the system. To calculate N_p as a function of μ_p^r the following assumption is made:

$$N_p(\mu_p^r) = n_p^r \langle V_{\text{free}} \rangle_0 = n_p^r \alpha V, \quad (3.2)$$

implying that N_p is equal to the number density of polymers in the reservoir n_p^r times the free volume in the unperturbed system $\langle V_{\text{free}} \rangle_0$. This free volume is equal to the free volume fraction α times the system volume V . The free volume fraction can be found from Scaled Particle Theory [18, 93] and reads

$$\alpha = (1 - \phi_c) \exp \left[- \left(Ad + Bd^2 + Cd^3 \right) \right], \quad (3.3)$$

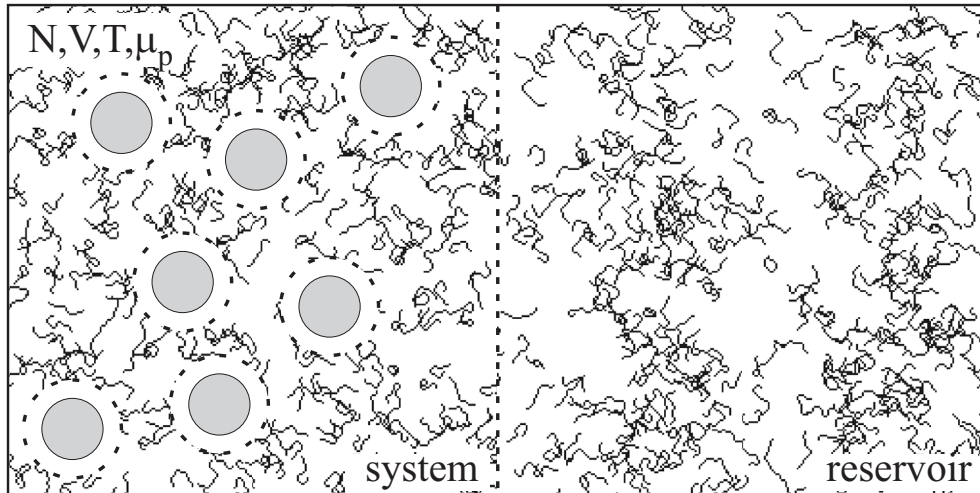


FIGURE 3.1. Schematic representation of the semi-grand canonical scheme. The reservoir is filled with polymer and connected to the system via a semi-permeable membrane. The system contains both polymers and colloids and its free volume is the total system volume V minus the volume of the depleted zones. Note that the centres of mass of the polymers cannot penetrate the depletion zones.

with $d = \phi_c/(1 - \phi_c)$ and the quantities A , B and C functions of the depletion thickness (in this approach a step function with thickness Δ) divided by R_c :

$$\begin{aligned} A &= 3\frac{\Delta}{R_c} + 3\left(\frac{\Delta}{R_c}\right)^2 + \left(\frac{\Delta}{R_c}\right)^3 \\ B &= \frac{9}{2}\left(\frac{\Delta}{R_c}\right)^2 + 3\left(\frac{\Delta}{R_c}\right)^3 \\ C &= 3\left(\frac{\Delta}{R_c}\right)^3. \end{aligned} \quad (3.4)$$

The integration over μ_p^r in (3.1) can be replaced with an integration over n_p^r by applying the Gibbs-Duhem relation:

$$d\mu_p^r = \frac{1}{n_p^r}d\Pi = \frac{1}{n_p^r}\left(\frac{\partial\Pi}{\partial n_p^r}\right)_T dn_p^r. \quad (3.5)$$

Here Π is the osmotic pressure of the polymers. Finally, it is convenient to rewrite (3.1) in a dimensionless form:

$$\tilde{\omega} = \tilde{f} - \int_0^{\phi_p^r} \alpha \left(\frac{\partial\tilde{\Pi}}{\partial\phi_p^{r'}}\right)_T d\phi_p^{r'}, \quad (3.6)$$

with $\tilde{\omega} = \Omega v_c/k_B TV$ (with k_B the Boltzmann constant and $v_c = \frac{4}{3}\pi R_c^3$ the volume of a colloid), $\tilde{f} = F v_c/k_B TV$ and $\tilde{\Pi} = \Pi v_c/k_B T$ the dimensionless osmotic pressure of the polymer solution. Furthermore, ϕ_p^r is the polymer volume fraction ($\phi_p^r = n_p^r v_p$ with $v_p = \frac{4}{3}\pi R_g^3$). Equation (3.6) is the central equation in this thermodynamic scheme. The coexisting phases follow from the conditions (common-tangent procedure)

$$\begin{aligned} \left(\frac{\partial\tilde{\omega}_1}{\partial\phi_{c1}}\right)_{\phi_p^r} &= \tilde{\mu}_1(\phi_p^r) = \tilde{\mu}_2(\phi_p^r) = \left(\frac{\partial\tilde{\omega}_2}{\partial\phi_{c2}}\right)_{\phi_p^r} \\ \left(\frac{\partial\tilde{\omega}_1}{\partial\phi_{c1}}\right)_{\phi_p^r} \phi_{c1} - \tilde{\omega}_1 &= \tilde{P}_1(\phi_p^r) = \tilde{P}_2(\phi_p^r) = \left(\frac{\partial\tilde{\omega}_2}{\partial\phi_{c1}}\right)_{\phi_p^r} \phi_{c2} - \tilde{\omega}_2 \end{aligned} \quad (3.7)$$

Throughout this chapter we use a very accurate expression for the free energy of the pure hard sphere system \tilde{f} following from the Carnahan-Starling equation of state [94]:

$$\tilde{f} = \phi_c \ln \phi_c + \frac{4\phi_c^2 - 3\phi_c^3}{(1 - \phi_c)^2} - \phi_c. \quad (3.8)$$

This can be used to describe both gas (G) and liquid (L) phases as well as the fluid (F) phase. To describe the crystalline phase (C) we make use of a reference free energy obtained from computer simulations [95], from which the crystalline free energy \tilde{f}_c follows as

$$\tilde{f}_c = -\tilde{P}_c + \phi_c \tilde{\mu}_c = -\frac{3\phi_c}{1 - \phi_c/\phi_{cp}} + \phi_c \left(2.1306 + \frac{3}{1 - \phi_c/\phi_{cp}} + 3 \ln \left[\frac{\phi_c}{1 - \phi_c/\phi_{cp}} \right] \right) \quad (3.9)$$

with the closest packed volume fraction $\phi_{cp} = \pi\sqrt{2}/6$. Except for the thermodynamic properties of the polymer solution and the depletion layer thickness we have all ingredients to calculate the binodals using (3.7).

3.3. IDEAL POLYMERS

The osmotic pressure of ideal polymers is given by van 't Hoff's law $\Pi = n_p k_B T$ and the osmotic compressibility $\partial\tilde{\Pi}/\partial\phi_p^r$ then simply is $1/q^3$. The integral in (3.6) now becomes

$$\int_0^{\phi_p^r} \alpha \left(\frac{\partial\tilde{\Pi}}{\partial\phi_p^{r'}} \right)_T d\phi_p^{r'} = \frac{\alpha}{q^3} \phi_p^r. \quad (3.10)$$

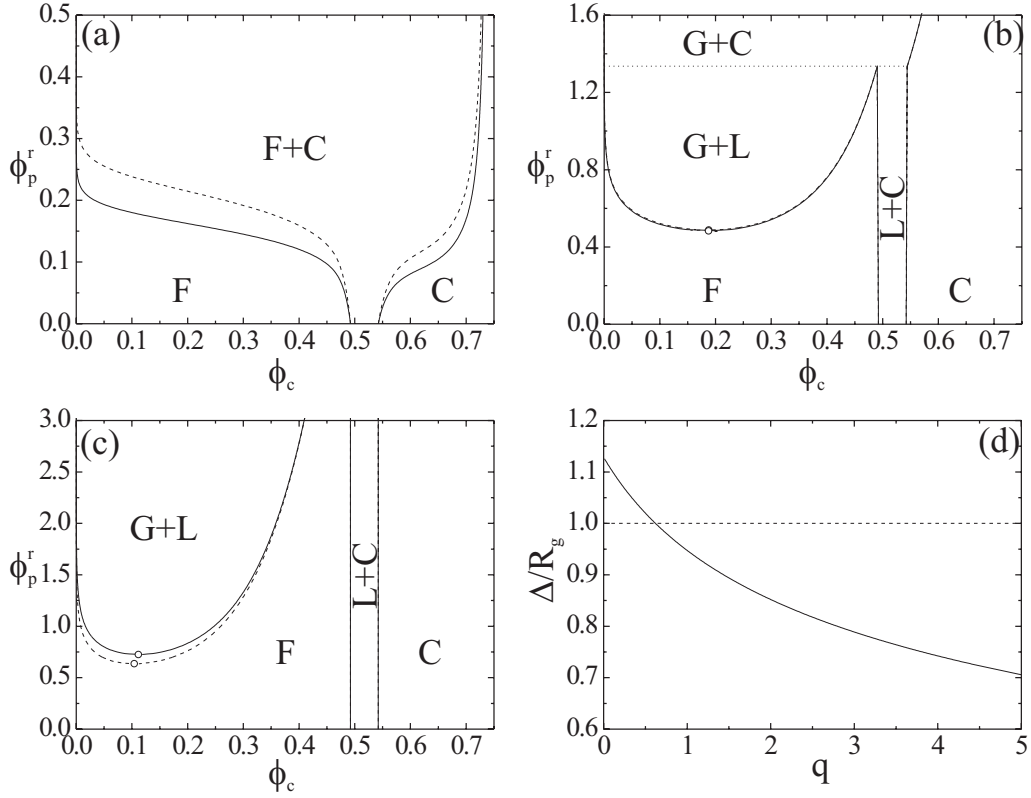


FIGURE 3.2. (a-c) Phase diagrams for colloid-polymer mixtures with different polymer-colloid size ratios (respectively, $q = 0.1$, $q = 0.6$, $q = 1.0$) in polymer reservoir concentration. In (d) the curvature dependence of Δ/R_g as in (3.11) is plotted. Dashed lines follow from the theory described in [18] ($\Delta = R_g$), while solid lines are the result when using (3.11). Dotted lines denote triple points (gas-liquid-crystal coexistence) and open circles denote critical points. The characters G, L, F and C stand for colloidal gas, liquid, fluid and crystal phases respectively.

If Δ is known we have all the ingredients to calculate the phase behaviour. Lekkerkerker *et al.* [18] used $\Delta = R_g$ and thus treated the polymers as penetrable hard spheres with effective radius R_g . In that case Δ/R_c in (3.4) becomes q .

Although the typical length scale of an ideal polymer solution in the bulk indeed is the radius of gyration, the typical length scale near a wall or spherical colloidal surface is different. The depletion thickness near an interface can be calculated if the polymer density profile is known. The density profile is found by solving the Edwards diffusion equation [96, 97]. Near a single wall, this profile was calculated by Eisenriegler [98], leading to $\Delta = 2R_g/\sqrt{\pi}$. The polymer density profile around a sphere was derived by Taniguchi *et al.* [89] and independently by Eisenriegler *et al.* [90]. In the Appendix of this chapter the depletion thickness as a function of curvature is derived for ideal polymers leading to (3.18), i.e.

$$\frac{\Delta}{R_c} = \left(1 + \frac{6}{\sqrt{\pi}}q + 3q^2\right)^{1/3} - 1. \quad (3.11)$$

This expression for Δ/R_c is used in (3.4). In the limit of $q \rightarrow 0$, Δ/R_c becomes $2q/\sqrt{\pi}$ agreeing with the flat wall case and for larger q , Δ/R_c decreases. Curvature effects are now included in the free volume approach. The resulting phase diagrams are presented in figure 3.2. Clearly, the effect of curvature on the general phase behaviour is small in the ideal case, except for very large q where $\Delta \ll R_g$.

3.4. POLYMERS WITH EXCLUDED VOLUME INTERACTIONS

In good solvents excluded volume interactions between polymer segments have to be taken into account in order to describe the thermodynamics of the polymers in solution properly. Thus, we first need an expression for the osmotic compressibility. This can be found from RG-theory [91] for polymers in the full excluded volume limit and is in dimensionless form equal to

$$\left(\frac{\partial \tilde{\Pi}}{\partial \phi_p^r}\right) = \frac{1}{q^3} \left(1 + 2.629\phi_p^r \left(\frac{1 + 3.251\phi_p^r + 4.151(\phi_p^r)^2}{1 + 1.480\phi_p^r}\right)^{0.309}\right). \quad (3.12)$$

Secondly, curvature effects have to be incorporated. Hanke *et al.* [92] calculated the insertion energy to place a single colloidal sphere in a sea of excluded volume polymers. This energy is equal to the total number of polymers depleted from a certain region and is analyzed in terms of flat and curvature terms. We can calculate a depletion thickness from this number by making use of a step-function and Δ/R_c becomes

$$\frac{\Delta}{R_c} = \left(1 + 3a\left(\frac{R_g}{R_c}\right) + 3b\left(\frac{R_g}{R_c}\right)^2 - 3c\left(\frac{R_g}{R_c}\right)^3\right)^{\frac{1}{3}} - 1, \quad (3.13)$$

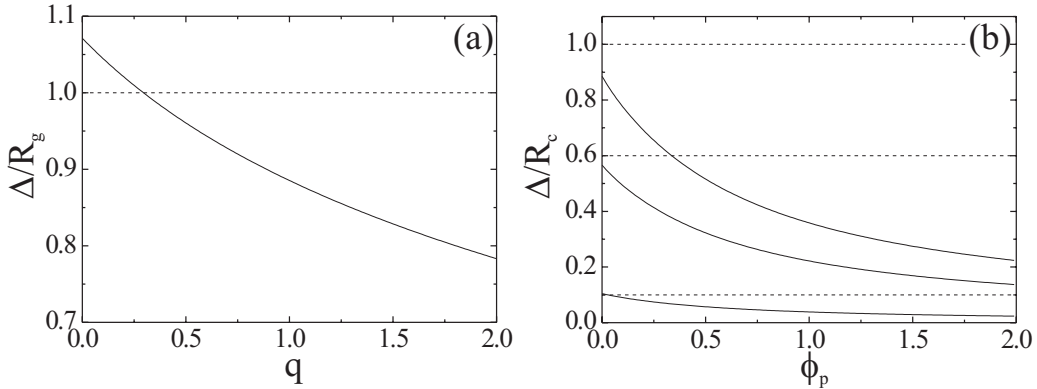


FIGURE 3.3. (a) Curvature dependence of Δ/R_g and (b) concentration dependence of Δ/R_c following (3.13) (full curves) with modifications explained in the text and for the ideal case with $\Delta = R_g$ (dashed curves). The concentration dependence is shown for three different polymer-colloid size ratios, from top to bottom curves: $q = 1.0, 0.6$ and 0.1 .

with

$$\begin{aligned}
 a &= \frac{2}{\sqrt{\pi}} \left[1 - \frac{1}{4} \left(1 - \frac{3}{2} \ln 2 - \frac{\pi}{2} + \frac{\pi}{\sqrt{3}} \right) \right] \approx 1.0710 \\
 b &= 1 - \frac{5\pi}{8} + \frac{17}{36} + \frac{\pi\sqrt{3}}{4} \approx 0.8691 \\
 c &= \frac{1}{3\sqrt{\pi}} \left(\frac{1673\pi}{48} - \frac{551}{15} - \frac{40\pi}{\sqrt{3}} \right) \approx 0.0399.
 \end{aligned} \tag{3.14}$$

Note that (3.13) is the RG-theory result up to third order in curvature and hence applicable for small q . To incorporate the polymer concentration dependence we replace R_g with the correlation length in bulk which is in line with the work of Joanny *et al.* [76]. Expressions for the bulk correlation length as well as the osmotic compressibility are taken from [91] and we have all the ingredients for (3.6). In figure 3.3(a) we show the curvature dependence of Δ/R_g , which clearly deviates from the standard ideal case with $\Delta = R_g$ and in figure 3.3(b) the concentration dependence of Δ/R_c is plotted. The depletion thickness decreases strongly as a function of the polymer concentration.

3.5. RESULTS

In this section we present phase diagrams obtained with the proposed theory for mixtures of colloidal hard spheres and polymer chains with excluded volume interactions between the segments in a common solvent. The results are compared with those for mixtures of ideal polymers mixed with colloidal spheres as described in [18] and with experimental phase diagrams. In figure 3.4 we present phase diagrams for three different colloid-polymer size ratios. For $q = 0.1$ (figure 3.4(a)) the difference between describing

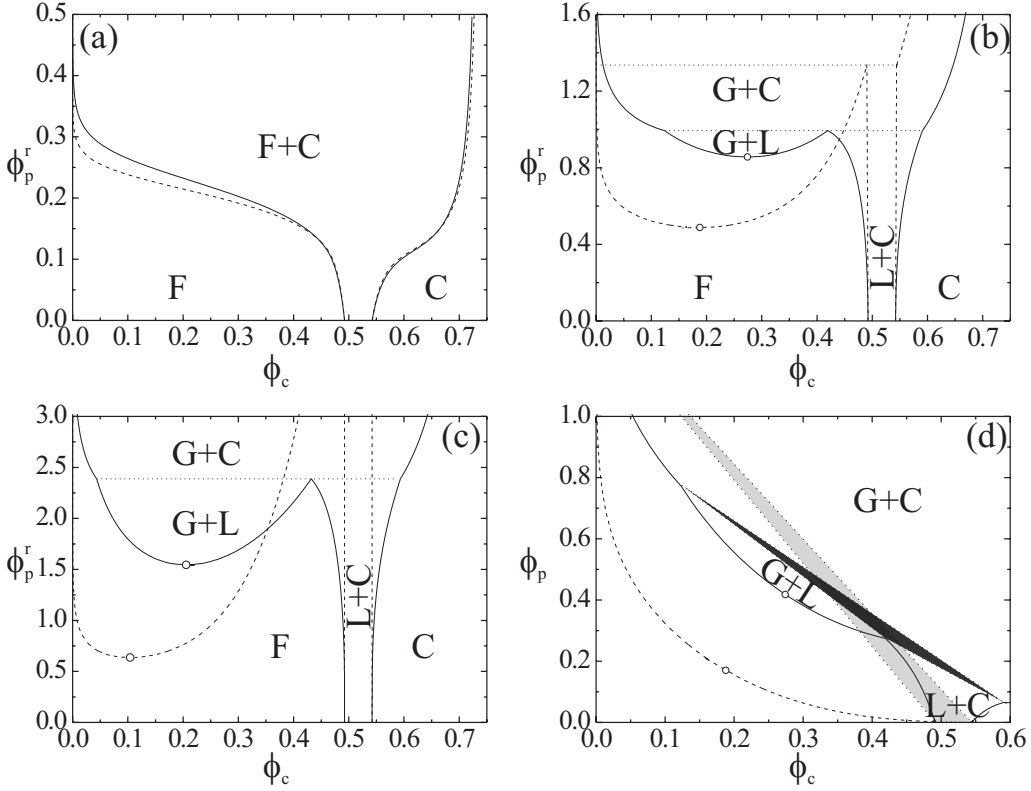


FIGURE 3.4. (a-c) Phase diagrams for colloid-polymer mixtures with different colloid-polymer size ratios (respectively, $q = 0.1$, $q = 0.6$, $q = 1.0$) in reservoir polymer concentration. Dashed curves follow from the theory described in [18] ($\Delta = R_g$), while solid curves are valid for mixtures of excluded volume polymers and colloids and follow from (3.13) with modifications explained in the text. (d) Phase diagram in system polymer concentration for $q = 0.6$. The light grey area is the three phase region for ideal polymers and the dark grey area for excluded volume polymers. Dotted lines denote triple points (gas-liquid-crystal coexistence) and open circles depict critical points.

the polymers as ideal following [18] or with excluded volume interactions is clearly very small, while the difference is much larger for $q = 0.6$ and $q = 1.0$ (figure 3.4(b) and (c)). Since the depletion thickness Δ becomes smaller than R_g if $q > 0.30$ (figure 3.3(a)) and because Δ decreases rapidly as a function of polymer concentration (figure 3.3(b)) more polymer is needed for gas-liquid phase separation to occur for $q = 0.6$ and $q = 1.0$. Furthermore, the gas-liquid region becomes quickly metastable with respect to gas-crystal coexistence due to the strongly rising osmotic compressibility (3.12) compared to the ideal case. Related to this is the observation that gas-liquid coexistence first becomes stable for $q = 0.48$, while this is at $q = 0.33$ for ideal polymers. In fact, quantitative agreement is found with predictions for star polymer-colloid mixtures by Dzubiella *et al.* [99, 100], when comparing to star polymers with two arms, i.e. linear

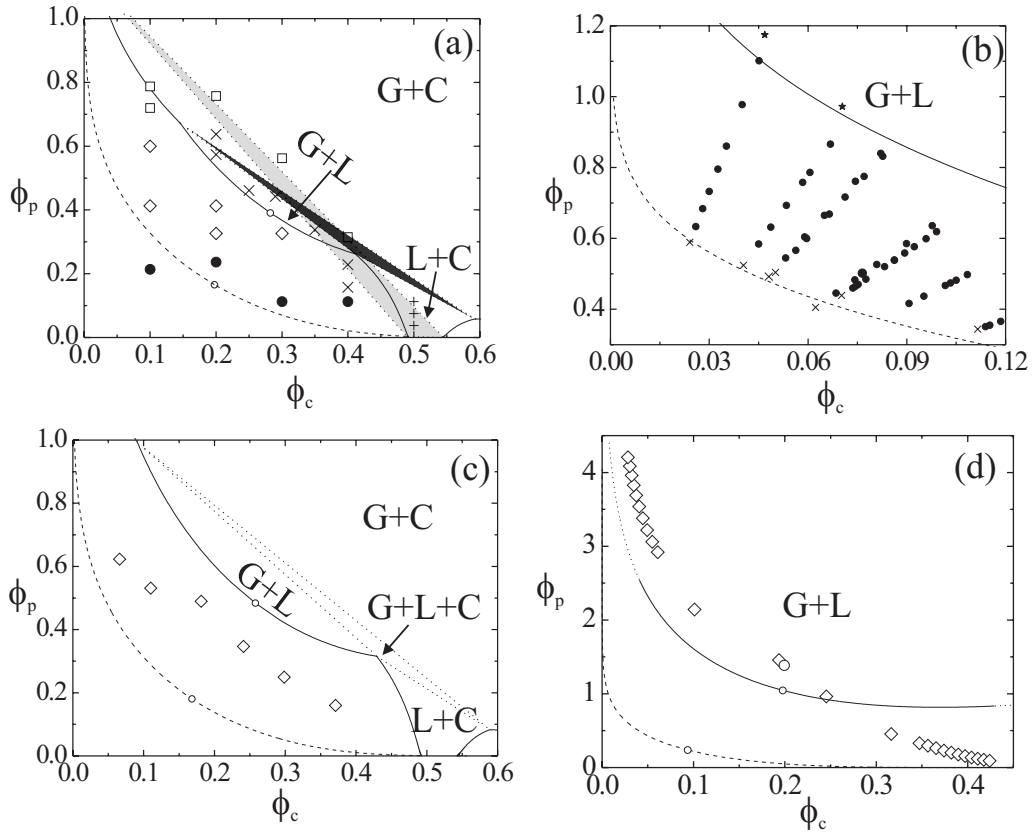


FIGURE 3.5. Comparison of experiment with the ideal theory described in [18] (dashed curves) and the model proposed here for excluded volume polymers (full curves) with experimental phase diagrams for (a) $q = 0.57$ from [50], (b) $q = 0.56$ (system 2 PPD25), (c) $q = 0.667$ from [101] and (d) $q = 1.08$ from [36] (system 1 SPC13). The open circles denote critical points. The symbols in (a) denote the following: filled circle, fluid; diamond, gas plus liquid; cross, gas plus liquid plus crystal; plus sign, liquid plus crystal; square, gas plus crystal. The light area is the three phase region for ideal polymers and the dark area for excluded volume polymers. In (b) state points are indicated where gas-liquid phase separation occurs (circles), state points in the one-phase region (crosses) and state points where the system gelled (stars). In (c) and (d) the open diamonds are the experimental binodal points.

polymer chains. They found stable fluid-fluid demixing for $q \geq 0.5$. In figure 3.4(d) we make the transition to system polymer concentrations for $q = 0.6$ by multiplying the reservoir polymer volume fraction ϕ_p^r with the free volume fraction in one phase $\alpha(\phi_{c1})$: $\phi_{p1} = \phi_p^r \alpha(\phi_{c1})$. Here, we see that the liquid-crystal region is much larger than in the ideal case. In addition, the three phase coexistence region is shifted upwards and becomes slightly smaller.

In figure 3.5 we make the comparison with experimental phase diagrams. Ilett *et al.* constructed phase diagrams for mixtures of polymethylmethacrylate (PMMA) colloidal spheres and polystyrene polymer in purely cis-decalin [50] resembling systems 2 PPD25 and 3 PPD71 of chapter 2, but with a lower polymer θ -temperature of 12°C instead of 16.5°C [68]. In figure 3.5(a) we compare their constructed phase diagram for $R_c = 228$ nm and $R_g = 130$ nm ($q = 0.57$) with the original free volume theory and with the extension described in section 3.4 to include excluded volume polymers. Although the gas-liquid region is underestimated by the extended theory, both the liquid-crystal as well as the three phase region are much better predicted. In (b) we show results for a similar system even closer to θ -conditions, i.e. system 2 PPD25 as described in chapter 2. Here, the ideal polymer model leads to a gas-liquid binodal in closer agreement with the experimental binodal than the EVI-polymer model. Ramakrishnan *et al.* [101] measured the gas-liquid binodal for mixtures of colloidal silica spheres coated with stearyl alcohol ($R_c = 50$ nm) and polystyrene polymer in toluene. Here, we compare the result with polystyrene with a molar mass of $5.5 \cdot 10^5$ g mol⁻¹ ($R_g = 33.37$ nm) resulting in a size ratio $q = 0.667$ in figure 3.5(c). The dashed curve (the original theory) clearly predicts too low polymer concentrations at the binodal, while the full curve (present theory) overestimates the required polymer concentration at the binodal. In figure 3.5(d) we compare with the experimental phase line of mixtures of small stearyl coated silica spheres ($R_c = 13$ nm) and polydimethylsiloxane polymer ($R_g = 14$ nm) in cyclohexane with a size ratio $q = 1.08$, i.e. system 1 SPC13 in chapter 2. De Hoog and Lekkerkerker [36] determined the binodal by following the method of Bodnar and Oosterbaan [60]. The dashed curve is the ideal polymer theory result and again the new theory (full curve) predicts phase separation to occur at much higher polymer concentration. This full curve is partially dotted where the gas-liquid phase separation is no longer stable with respect to gas-solid phase separation. However, no gas-solid phase coexistence was observed experimentally possibly due to suppression by sphere polydispersity, which is not accounted for in the present theory. Furthermore, the present theory predicts too high polymer concentration above a certain colloid volume fraction, the reason for which is unknown.

3.6. DISCUSSION AND CONCLUSION

The effects of curvature and of excluded volume polymers on the phase behaviour of colloid-polymer mixtures have been taken into account by extending the free volume theory [18]. For ideal polymers curvature effects are included by using the polymer density profile [89, 90], which has a small effect on the general phase behaviour. For excluded volume polymers results from RG-theory [91, 92] were used and in that case both the description with excluded volume polymers and the curvature play a role. For small size ratios (as shown for $q = 0.1$) the depletion thickness is approximately R_g ;

curvature effects are weak and the concentration is not yet sufficiently large to decrease the correlation length significantly with respect to R_g . For $q = 0.6$ and 1.0 the curvature effects are stronger and especially the correlation length has dropped significantly at the polymer concentrations where the system becomes unstable. Thus, the gas-liquid phase coexistence will shift to larger polymer concentrations for excluded volume polymers as compared to ideal polymers. At the same time the liquid-crystal region becomes larger, while the three phase coexistence region becomes less extended.

In comparison with experiment we see that the ideal polymer theory predicts too low polymer concentrations for gas-liquid phase separation to occur and that our new model predicts too high polymer concentrations, except for $q = 1.08$ [36]. Although the phase diagram for this colloid-polymer mixture was carefully determined, both colloidal spheres and polymers are rather polydisperse, which certainly affects the location of the binodal [61–64]. Liquid-crystal coexistence, clearly present in experiment for $q = 0.57$ [50] (figure 3.5(a)), is almost absent for ideal polymers (a discrepancy of about a factor of 250 [52]). It appears, however, when using excluded volume polymers. A significantly more accurate description of the liquid-crystal coexistence region is perhaps one of the major achievements of the present theory. In addition, we observe that most experimental gas-liquid binodals lie in between the ideal polymer and the EVI-polymer predictions. Furthermore, in mixtures of PMMA colloids and poly(styrene) polymer in decalin the phase behaviour appears to depend on the exact θ -conditions of the polymer. We conclude that modifying the free volume theory to incorporate excluded volume polymers is rather straightforward and results in a better description of some of the significant features in the experimental phase diagrams. More sophisticated theories are, however, required to obtain a more complete quantitative agreement with experiments.

APPENDIX: DEPLETION THICKNESS FOR IDEAL POLYMERS

Placing a colloidal sphere in a sea of polymers depletes N_p^{dep} polymers from a certain volume. This number is equal to the polymer number density n_p times the volume that is depleted of polymers, which is the colloid volume v_c plus a region around the colloid found from the polymer concentration profile $f(x) = n(x)/n_b$:

$$N_p^{dep} = n_p v_c + n_p \int_{R_c}^{\infty} 4\pi x^2 (1 - f(x)) dx. \quad (3.15)$$

The profile [89,90] gives the local polymer segment density $n(x)$ at a distance x from the colloidal surface divided by the polymer bulk segment density n_b and has the following form

$$\begin{aligned} f(x) = & \left[\frac{R_c}{R_c + x} \right]^2 \left\{ \left(\frac{x}{R_c} \right)^2 + \frac{2x}{R_c} \left(\operatorname{erf}(z) - 2z^2 [1 - \operatorname{erf}(z)] + \frac{2}{\sqrt{\pi}} z \exp(-z^2) \right) \right. \\ & + 2 \operatorname{erf}(z) - \operatorname{erf}(2z) + \frac{4z}{\sqrt{\pi}} [\exp(-z^2) - \exp(-4z^2)] \\ & \left. + 8 z^2 \left[\frac{1}{2} - \operatorname{erf}(2z) + \frac{1}{2} \operatorname{erf}(z) \right] \right\}, \end{aligned} \quad (3.16)$$

where $z = x/2R_g$. This polymer profile can be replaced by a step-function and this defines a depletion thickness Δ , which can be found by solving (3.17) for Δ

$$n_p v_c + n_p \int_{R_c}^{\infty} 4\pi x^2 (1 - f(x)) dx = n_p \frac{4\pi}{3} (R_c + \Delta)^3 \quad (3.17)$$

After doing the integration the resulting curvature dependence of $\Delta(q)$ becomes

$$\frac{\Delta}{R_c} = \left(1 + \frac{6q}{\sqrt{\pi}} + 3q^2 \right)^{1/3} - 1. \quad (3.18)$$

4

Interfacial tension and wetting behaviour in colloid-polymer mixtures: Theory

ABSTRACT

We calculate the interfacial tension and the wetting behaviour in phase separated colloid-polymer mixtures both for ideal and excluded volume interacting polymers. Within the recently developed extension of the free volume theory to include polymer interactions [Aarts, Tuinier, and Lekkerkerker, *J. Phys.: Condens. Matter* 14, 7551, 2002], see also chapter 3, the interfacial tension of the free interface is calculated by adding a van der Waals squared gradient term. The wetting behaviour at a hard wall is calculated following a Cahn-Fisher-Nakanishi approach taking the one- and two-body colloid-wall interactions into account. Comparing results for interacting polymers with those for ideal polymers we find that for interacting polymers the interfacial tension does not increase as steeply as a function of the gas-liquid colloid density difference. Furthermore, the wetting transition shifts to higher polymer concentrations, even to above the triple line. The predictions for both the interfacial tension and the wetting behaviour are compared to recent experiments.

4.1. INTRODUCTION

Mixtures of colloids and non-adsorbing polymer display rich phase behaviour and are an excellent tool for studying equilibrium properties, phase transition kinetics, and metastable gel or glass states (for a recent comprehensive review, see [26]). Recently, the interfacial tension between the coexisting phases received some attention, first experimentally by measurements of the ultralow interfacial tension of the order of at most a few $\mu\text{N}/\text{m}$ between demixed colloidal “liquid” (rich in colloid, poor in polymer) and

colloidal “gas” (poor in colloid, rich in polymer) phases [35, 36, 38]. This in turn led to a number of theoretical efforts, starting with a paper by Vrij [102]. Within the Asakura-Oosawa-Vrij (AOV) model [19, 25], which treats the polymers as ideal mutually penetrable hard spheres (PHS), Brader and Evans [103] calculated the interfacial tension using a squared gradient approach. In the work of Brader and Evans the degrees of freedom of the polymer were integrated out such that an effective one-component system was obtained, similar but not equal to the semi-grand potential derived using the free volume theory [18]. The order of magnitude of the resulting interfacial tensions compares well to the experimental values even though the predicted phase diagram does not quantitatively correspond to the experimental bulk phase diagram, see the discussion in chapter 3 about figure 3.5(d). The fact that the experimental bulk phase diagram is not well described by theory is that in experiment polymers often behave far from ideal.

Theory preceded experiment in the prediction of the existence of a wetting transition of the mixtures in contact with a hard planar wall [82]. At this wetting transition the “liquid” phase starts wetting the wall completely instead of partially and the contact angle between the interface and the wall changes to zero degrees. Again polymers were modelled as PHS but they were now explicitly described, hence the colloid-polymer mixture is treated as a true binary mixture, within the formalism of fundamental measures theory [104]. For homogeneous phases this density functional reduces exactly to the aforementioned free volume theory [18]. Moreover, it can be extended to a mixture in the vicinity of a hard wall. Doing so, in addition to layering transitions, a first-order wetting transition was found [82]. These results were recently confirmed using computer simulations by Dijkstra and van Roij [105], again describing polymers as PHS. They found transitions reasonably close to those of the predictions in [82]. First experiments on system 1 SPC13, which will be shown in chapter 5, did confirm that the colloidal liquid phase favours the wall [106] and the accompanying interfacial tension was in reasonably good agreement with previous measurements [36]. Whether or not the liquid phase was partially or completely wetting could not be concluded in this work, because of the difficulty in measuring the contact-angles with sufficient accuracy. This was subsequently solved by studying a fluorescent colloid-polymer mixture (system 2 PPD25) with laser scanning confocal microscopy. No wetting transition was observed, as will be presented and discussed in chapter 5 [107]. However, in a colloid-polymer mixture similar to system 1 SPC13 a wetting transition was reported [108, 109]. The authors mention the difficulty of comparing the experimentally found location of the wetting transition to the theoretical prediction. The reason for this is that in their experiment polymers behave far from ideal. Several ways to describe polymers more realistically are available in literature [87, 110–116] mainly focussing on bulk phase behaviour. Here

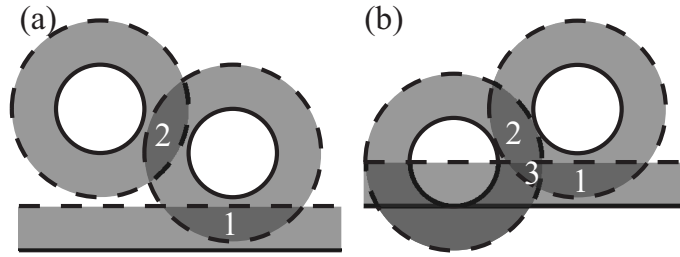


FIGURE 4.1. Two possible configurations for two colloids near a flat hard wall. The depletion zones are indicated by dashed lines. In (a) we have a colloid-wall interaction (1) and a colloid-colloid interaction (2) while in (b) we also have a colloid-colloid-wall interaction (3).

we extend the earlier bulk model of Ref. [111], see chapter 3, to calculate the interfacial tension and to describe the wetting behaviour now also for interacting polymers.

That the colloidal liquid phase (partially) wets the wall is normally explained with “classical” AOV-like arguments, hence in terms of overlap volumes and accompanying interactions (see figure 4.1). Since at contact the overlap-volume between a wall and a colloid (volume 1 in figure 4.1(a)) is about twice the overlap-volume between two colloids (volume 2 in figure 4.1(a)) the colloidal liquid phase favours the wall, although the pair attraction is reduced if two colloids are close to the wall and to each other (volume 3 in figure 4.1(b)). One of the goals of this work is to put this qualitative view in a quantitative form using the Cahn theory of wetting [9]. In addition, we want to explore theoretically the possibilities of observing a wetting transition in experiment, especially in experimental system 1 SPC13 (chapter 2), since this system initiated this theoretical work, but also in system 2 PPD25. The accompanying experimental part is presented in chapter 5.

We work at a semi-grand canonical level, treating the polymers grand canonically and the colloids canonically. We thus effectively have a one component system of colloids at a constant chemical potential of the polymer maintained by a reservoir filled with only polymer. We focus on predictions of the bulk phase behaviour, the interfacial tension, the wetting transition and the prewetting line for ideal polymers as well as for excluded volume interacting (EVI) polymer chains. To keep descriptions simple and straightforward we describe the inhomogeneities with a squared gradient term as in [103], but with the free volume expression [18] for the bulk free energy. The interaction with the wall is described up to second order in colloid contact density, i.e. we follow a Fisher-Nakanishi like [117] extension of the Cahn theory of wetting [9] (for a recent review see [118]). We present theory for the bulk phase behaviour in section 4.2, for the free interface in section 4.3 and for the mixture near a flat hard wall in section 4.4. We summarize our main findings in section 4.5.

4.2. BULK PHASE BEHAVIOUR

The starting point of our analysis is the thermodynamic potential $F(N_c, V, T, \mu_p^r)$ of a bulk fluid of N_c colloids in a volume V and with temperature T , in osmotic contact with a polymer reservoir of chemical potential μ_p^r (and osmotic pressure Π). Using the free volume approach of [18] yields

$$F(N_c, V, T, \mu_p^r) = F_0(N, V, T) - V \int_0^{n_p^r} dn_p^{r'} \alpha \left(\frac{\partial \Pi}{\partial n_p^{r'}} \right). \quad (4.1)$$

In [111], chapter 3, we derived this in detail, showed how to make the extension from ideal to interacting polymer chains, and gave the necessary expressions explicitly. Here, we will only briefly repeat some of it. In (4.1) F_0 is the free energy of the pure hard sphere system, i.e. without added polymer, α is the free volume fraction, and n_p^r the polymer number density in the reservoir. The polymer concentration in the system is given by: $n_p = \alpha n_p^r$. For F_0 we use the Carnahan-Starling equation of state [94] to describe the fluid, gas and liquid phases and we make use of a reference free energy obtained from computer simulations [95] to describe the crystalline phase. The osmotic compressibility ($d\Pi/dn_p^r$) depends on the nature of the polymers; for ideal polymers it equals $1/\beta$ with $\beta = 1/k_B T$ and for polymers in the full excluded volume limit we use expressions from Renormalization Group theory (equation (17.53) from [91]):

$$\beta \left(\frac{d\Pi}{dn_p^r} \right) = 1 + 2.629 \phi_p^r \left(\frac{1 + 3.251 \phi_p^r + 4.151 (\phi_p^r)^2}{1 + 1.480 \phi_p^r} \right)^{0.309}, \quad (4.2)$$

with $\phi_p^r = n_p^r v_p$ and $v_p = \frac{4}{3} \pi R_g^3$ (R_g is the polymer's radius of gyration). The free volume fraction α is given by

$$\alpha = (1 - \phi) \exp \left[- \left(Ad + Bd^2 + Cd^3 \right) \right], \quad (4.3)$$

with ϕ the volume fraction of colloids and $d = \phi/(1 - \phi)$. The parameters A, B and C are functions only of the depletion thickness (in this approach a step function with thickness Δ) divided by the radius of the colloid R_c :

$$\begin{aligned} A &= 3 \frac{\Delta}{R_c} + 3 \left(\frac{\Delta}{R_c} \right)^2 + \left(\frac{\Delta}{R_c} \right)^3 \\ B &= \frac{9}{2} \left(\frac{\Delta}{R_c} \right)^2 + 3 \left(\frac{\Delta}{R_c} \right)^3 \\ C &= 3 \left(\frac{\Delta}{R_c} \right)^3. \end{aligned} \quad (4.4)$$

For ideal polymers within the PHS approach Δ simply equals R_g and Δ/R_c becomes q , the polymer to colloid size ratio. For EVI-polymers we take both curvature (a polymer can –to some extent– wrap around a colloid) and concentration effects into account. The

depletion thickness now depends on the size ratio q and on the polymer concentration. We use results from Hanke *et al.* [92] to incorporate the curvature dependence:

$$\frac{\Delta}{R_c} = \left(1 + 3a \left(\frac{R_g}{R_c} \right) + 3b \left(\frac{R_g}{R_c} \right)^2 - 3c \left(\frac{R_g}{R_c} \right)^3 \right)^{\frac{1}{3}} - 1, \quad (4.5)$$

with analytical expressions for a , b and c approximately equal to 1.071, 0.869 and 0.040 respectively. To further incorporate polymer concentration dependence we replace R_g with the polymer bulk correlation length (equation (19.24) in [91]) which is in line with the work of Joanny *et al.* [76]. Having all ingredients for (4.1) we apply common-tangent constructions (after dividing the free energy by V to switch to free energy densities) and are thus able to find the coexisting densities (ρ_L and ρ_G for liquid and gas). In chapter 3, figure 3.5(d), we have compared the theoretical predictions to the experimentally determined binodal for a colloid-polymer mixture with $q = 1.08$ of stearyl-coated silica colloids ($R_c = 13$ nm) with poly(dimethylsiloxane) polymer ($R_g = 14$ nm) in cyclohexane [36], i.e. system 1 SPC13 in chapter 2. The predicted binodal for the mixture with ideal polymers does not agree quantitatively to the experimental binodal. The binodal for EVI-polymers shifts in the right direction, although it clearly predicts too high polymer concentrations above a certain colloid volume fraction, the reason for which is unknown. The overall agreement, however, has improved significantly and such a more quantitative agreement between the predicted phase behaviour for mixtures with EVI-polymers compared to experimental systems is a first step in making quantitative predictions about surface tension and wetting phenomena.

4.3. INTERFACE

To describe the free colloidal liquid-gas interface we start with the functional for the surface tension $\gamma[\rho]$:

$$\gamma[\rho] = \int_{-\infty}^{\infty} dz \left[f(\rho) - \mu_c \rho + p_c + m \left(\frac{d\rho}{dz} \right)^2 \right]. \quad (4.6)$$

Here, z is the distance to the interface, $f(\rho) = F/V$ is the free energy density, for which we use the semi-grand canonical potential F defined in (4.1) and divide by the volume V . Together with the second and third term (μ_c being the chemical potential and p_c the pressure at coexistence) this gives the excess free energy in the interfacial region. The last term in the integral accounts for density inhomogeneities. This quadratic term with the squared gradient coefficient m is in fact the first term of an expansion in derivatives of the density.

The coefficient m is given by the second moment of the direct correlation function $c(r)$ with r the center to center distance and reads:

$$m\beta = \frac{\pi}{3} \int_0^{\infty} dr r^4 c(r), \quad (4.7)$$

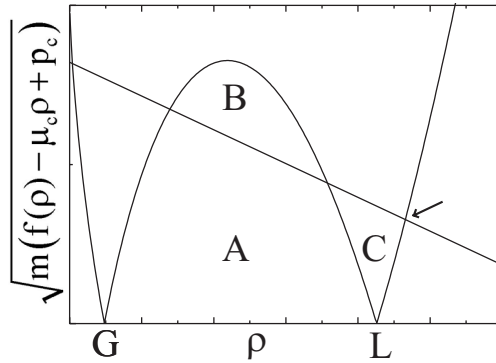


FIGURE 4.2. Ignoring the straight line the area A+B is proportional to the surface tension following from (4.12). The two minima are the gas liquid coexistence points. Adding the straight line, which is given by the l.h.s. of (4.23), enables one to solve (4.23) graphically. At the wetting transition the areas B and C must be equal. The arrow indicates the density of liquid phase at the wall.

Here, we use the mean spherical approximation for the direct correlation function which only depends on the attractive part of the pair potential $u(r)$ and hence $c(r) = 0$ for $r < \sigma_c$ (with σ_c the colloid diameter) and $c(r) = -\beta u(r)$ for $r \geq \sigma_c$. For ideal polymers the pair potential can be written as

$$u(r) = -k_B T n_p^r V_o(r), \quad (4.8)$$

with $V_o(r)$ the overlap volume between the two depletion zones. For general q and ideal polymers modelled as PHS m becomes

$$\frac{m\beta}{\sigma_c^5} = \frac{\pi}{6} \phi_p^r \left[1 + \frac{7q}{4} + \frac{7q^2}{5} + \frac{7q^3}{10} + \frac{q^4}{5} + \frac{q^5}{40} \right]. \quad (4.9)$$

For EVI-polymers the pair potential can be written as [119]

$$u(r) = - \int_0^{n_p^r} dn'_p \left(\frac{\partial \Pi}{\partial n'_p} \right) V_o(r, n'_p), \quad (4.10)$$

and m can be calculated numerically.

More sophisticated expressions for $c(r)$ could have been used, for example by rewriting the direct correlation functions from the density functional in [104] to an effective colloid-colloid direct correlation function. However, the resulting m can then become negative at high colloid densities, where the repulsive hard sphere contribution to $c(r)$ becomes more important than the attractive depletion contribution. This shows that the expansion in (4.6) in terms of gradients in the density does not converge as also noted in [103].

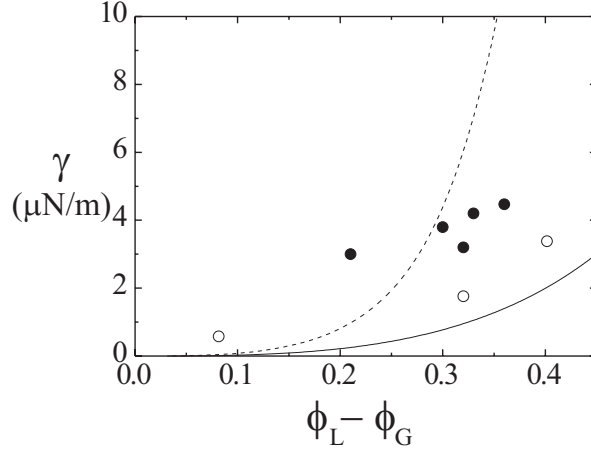


FIGURE 4.3. Comparison of experimental surface tension with theoretical predictions. The circles denote surface tensions measured in a colloid-polymer mixture with size ratio $q = 1.08$ of which the phase diagram is given in figure 3.5(d) (system 1 SPC13 in chapter 2). Closed circles represent measurements done by De Hoog and Lekkerkerker using a spinning drop technique [36] and open circles denote measurements by Aarts *et al.* obtained by analyzing the static profile near a vertical hard wall [106] (see chapter 5) on exactly the same experimental system. The dashed curve is the prediction describing the polymers as ideal, while describing the polymers as having excluded volume interactions results in the full curve.

Minimizing the interfacial tension (4.6) with respect to ρ using functional differentiation leads to

$$2m \frac{d^2 \rho}{dz^2} = \frac{df(\rho)}{d\rho} - \mu_c, \quad (4.11)$$

which can be used to calculate the equilibrium interfacial tension (without actually having to know the true shape of the interfacial profile):

$$\gamma = 2 \int_{\rho_G}^{\rho_L} d\rho \sqrt{m (f(\rho) - \mu_c \rho + p_c)}. \quad (4.12)$$

The interfacial tension is thus equal to area A + B in figure 4.2 (ignoring the straight line of which the meaning will be explained in section 4.4).

In figure 4.3 we present the surface tension obtained from the functional in (4.6) for ideal polymers with $q = 1.0$ (dashed curve) and for EVI-polymers with $q = 1.08$ (full curve). We chose $q = 1.0$ for ideal polymers in order to compare our results with existing theories [82, 103] and simulations [105] and we chose $q = 1.08$ for EVI-polymers to compare with experimental results [36, 106]. The change from $q = 1.0$ to 1.08 leads to better agreement with experiment, while this change has no serious consequences for the comparison with theory. Also shown are experimental interfacial tensions determined by De

Hoog and Lekkerkerker with a spinning drop apparatus for colloid-polymer mixtures at $q = 1.08$ [36] (filled circles). Aarts *et al.* measured the interfacial tension in exactly the same system (i.e. system 1 SPC13 in chapter 2) using a different (static) technique [106] (open circles), which will be presented in chapter 5: the gas-liquid interface was analyzed near a vertical hard wall, where the interface curvature depends only on the capillary length; by fitting the interfacial profile the interfacial tension was obtained. The discrepancy between the two experiments shows the difficulty of measuring such ultra-low interfacial tensions. Clearly, our prediction for the interfacial tension for ideal polymers (PHS) rises rather fast compared to the experiment, which is not surprising at all, because there is no good agreement between the predicted and the experimental phase diagram as was already mentioned in section 4.1 and discussed in section 4.2. The plot does illustrate, however, clear agreement with predictions by Brader *et al.* [82], where fundamental measures theory was used to describe the colloid-polymer mixture. This agreement justifies the use of squared gradient theory. Furthermore, we would like to stress the importance of the bulk free energy density on the predicted interfacial tensions, which is best illustrated by comparing our predictions to those from Brader and Evans [103]. We describe the density inhomogeneities in the same way as in [103], but use a different free energy density [18]. As a result, our predictions do not agree with those of [103], but do agree better with the more sophisticated approach of [82].

For EVI-polymers the predicted interfacial tension slightly underestimates the experimental data points, although the data taken from [106] are reasonably followed. The smaller interfacial tensions as well as the shift in the binodal to higher polymer concentrations as shown in figure 3.5(d) means that in the description with EVI-polymers instead of ideal polymers the effect of shrinking depletion zones as a function of polymer concentration, which leads to smaller overlap volumes and hence smaller attractions, is more important than the steeply increasing osmotic compressibility as a function of polymer concentration, which leads to stronger attractions. In fact, recently Louis and co-workers [120, 121] as well as Vink and Schmidt [122] observed similar trends, when including polymer-polymer interactions into theory and theory and simulations, respectively. The interfacial tension decreases with respect to calculations with ideal polymers.

4.4. COLLOID-POLYMER MIXTURE NEAR A HARD WALL

The next step is to describe the colloid-polymer mixture near a hard wall. We use the same expressions as above and add the following terms to the functional in (4.6) (in which the integration now ranges from 0 to ∞) to incorporate the interactions with

the wall

$$\begin{aligned} \gamma[\rho] = & \int_0^\infty dz \left[f(\rho) - \mu_c \rho + p_c + m \left(\frac{d\rho}{dz} \right)^2 \right] + \int_0^\infty dz \rho(z) U_2(z) \\ & - \frac{1}{2} \int_0^\infty dz \int d\mathbf{r} \rho(z) \rho(\mathbf{r}) U_3(z, \mathbf{r}) + \dots \end{aligned} \quad (4.13)$$

Here, U_2 is the attractive colloid-wall interaction, $U_2 \leq 0$, and can be found from (4.10), in which the overlap volume V_o now depends on the depletion zones of the wall and the colloid. The next term in (4.13) is a wall-induced correction (hence the minus sign) to the pair-wise colloid-colloid interaction, which is reduced (compared to its bulk pair interaction $u(r)$) in the vicinity of the hard wall. This is illustrated in figure 4.1(b), where the volume labeled “3” is counted twice (it contributes to $u(r)$ and $U_2(z)$) and should therefore be subtracted in order to give a proper account of the free volume. In other words, the system gains free volume only once. This is in fact the first order correction since three and more particle interactions with the wall are also possible and become more important for large q . One can easily show that for ideal polymers there are no volumes 3 when q becomes less than $\frac{1}{4}$. Thus this second term with U_3 depends on overlap volumes of type 3 (see figure 4.1(b)) to be included in (4.10) as V_o . We now should do this for all positions of the two particles with respect to each other and to the wall.

Instead of using the explicit form of (4.13) we make the following approximations

$$\int_0^\infty dz \rho(z) U_2(z) \approx \rho_1 \int_0^\infty dz U_2(z) \equiv -\rho_1 h_1, \quad (4.14)$$

in which we define the contact density as $\rho_1 \equiv \rho(0)$ and $h_1 = -\int_0^\infty dz U_2(z)$. In addition we approximate

$$-\int_0^\infty dz \int d\mathbf{r} \rho(z) \rho(\mathbf{r}) U_3(z, \mathbf{r}) \approx -\rho_1^2 \int_0^\infty dz \int d\mathbf{r} U_3(z, \mathbf{r}) \equiv \rho_1^2 g, \quad (4.15)$$

with $g = -\int_0^\infty dz \int d\mathbf{r} U_3(z, \mathbf{r})$. Here we make the same approximation as in (4.14) and write the correlated density-density product as the density squared. With these approximations we obtain a Cahn-Fisher-Nakanishi-like functional [9, 117] in which the interaction with the wall is described up to second order in density with clear physical parameters h_1 and g . These are similar to the “surface chemical potential” and the “surface enhancement parameter” in [117]. Note that the arguments of the integrals vanish beyond a certain small distance to the wall, since the overlap volumes with the wall needed to calculate U_2 and U_3 rapidly decay to zero. Our working functional therefore reads

$$\gamma[\rho] = \int_0^\infty dz \left[f(\rho) - \mu_c \rho + p_c + m \left(\frac{d\rho}{dz} \right)^2 \right] - \rho_1 h_1 + \frac{1}{2} \rho_1^2 g. \quad (4.16)$$

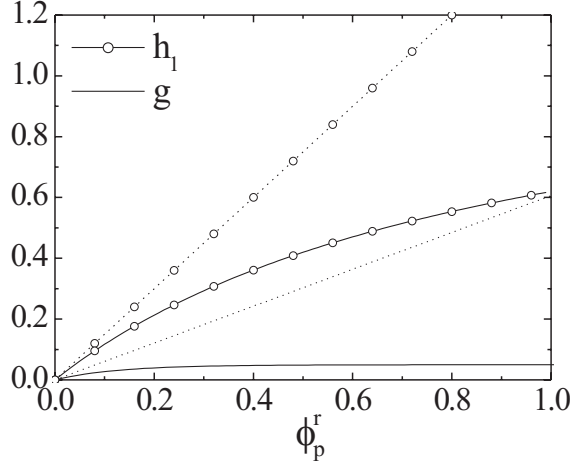


FIGURE 4.4. The parameters h_1 (with symbol) in units of σ_c/β and g (without symbol) in units of σ_c^4/β for $q = 1.0$ as a function of polymer concentration for ideal (dotted) and EVI-polymers (full).

For PHS h_1 can be calculated analytically and is given by

$$\frac{h_1\beta}{\sigma_c} = \phi_p^r \left(1 + \frac{q}{2}\right), \quad (4.17)$$

while for EVI-polymers it depends not only on Δ , but also on the depletion thickness near a wall, Δ_w . This can be found from (4.5) by taking the limit $q \rightarrow 0$. In figure 4.4 we plot h_1 as a function of polymer concentration and show that in case of ideal polymers (dotted line+symbol) this term rises faster than in case of EVI-polymers (full line+symbol). The next term, g , depends on the triple overlap volume (volume 3 in figure 4.1(b)) and is more difficult to calculate,

$$g = - \int dz \int d\mathbf{r} U_3 = \int dz \int d\mathbf{r} \int_0^{n_p^r} dn'_p \left(\frac{\partial \Pi}{\partial n'_p} \right) V_o = \int_0^{n_p^r} dn'_p \left(\frac{\partial \Pi}{\partial n'_p} \right) \int dz \int d\mathbf{r} V_o. \quad (4.18)$$

The resulting geometrical problem is closely related to problems described by Belleman [123] and Fischer [124]. There, however, the problem concerns two hard particles at a hard wall, while here we have soft particles at a wall which breaks some of the symmetry and changes the limits of integration. We follow the approach and notation of Fischer, change to cylindrical coordinates around particle 1 (shown in figure 4.5), and write the integrals in (4.18)) as

$$\int dz \int d\mathbf{r} V_o = 2\pi \int dz_1 \int dz_{21} \int dz_{31} \int dr_2 r_2 F_3, \quad (4.19)$$

with F_3 the overlap area between two disks at height z_{31} . For EVI-polymers and general q equation (4.19) can readily be calculated numerically, while for PHS and

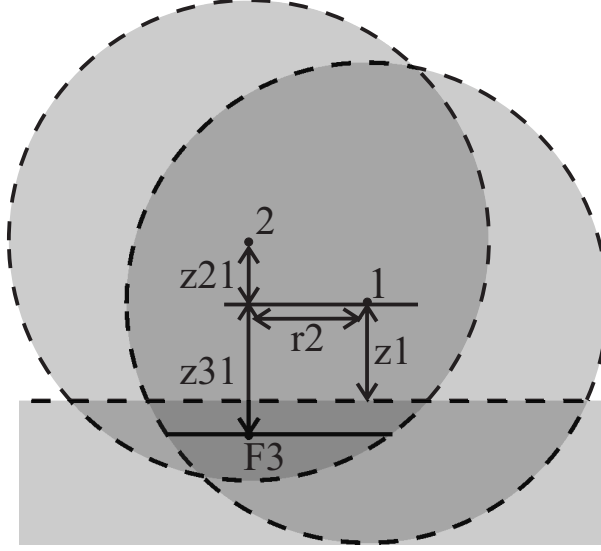


FIGURE 4.5. Explanation of the notation used in (4.19) following Fischer [124].

the symmetric case of $q = 1$ the integrals can be rewritten to much simpler integrals and equation (4.19) becomes $\frac{9}{280}\pi^2\sigma_c^7$ (see the Appendix of this chapter), and g reads

$$\frac{g\beta}{\sigma_c^4} = \frac{9}{280}\pi^2\sigma_c^3 n_p^r = \frac{27}{140}\pi\phi_p^r. \quad (4.20)$$

In figure 4.4 we plot g as a function of polymer concentration. Again, in case of ideal polymers (dotted line) this term rises faster than in case of EVI-polymers (full line). Moreover, for EVI-polymers g rapidly does not change anymore as a function of polymer concentration. The consequences of this for wetting will be discussed at the end of this section.

We now have all the ingredients of (4.16). Minimizing the interfacial tension with respect to ρ gives rise to the Euler-Lagrange equation

$$2m\frac{d^2\rho}{dz^2} = \frac{df(\rho)}{d\rho} - \mu_c \quad (4.21)$$

with boundary condition

$$-h_1 + g\rho_1 = 2m\left.\frac{d\rho}{dz}\right|_{z=0}. \quad (4.22)$$

The boundary condition appears because of the wall and one has to solve

$$h_1 - g\rho_1 = 2\sqrt{m(f(\rho_1) - \mu_c\rho_1 + p_c)}, \quad (4.23)$$

which can be done graphically [9]. At the wetting transition the three interfacial tensions in play satisfy $\gamma_{GS} = \gamma_{LS} + \gamma_{GL}$, where γ_{GS} and γ_{LS} are the gas and liquid-wall interfacial tensions, respectively, and γ_{GL} is the gas-liquid interfacial tension. This means that the areas B and C from figure 4.2 must be equal, since liquid at the wall (indicated by

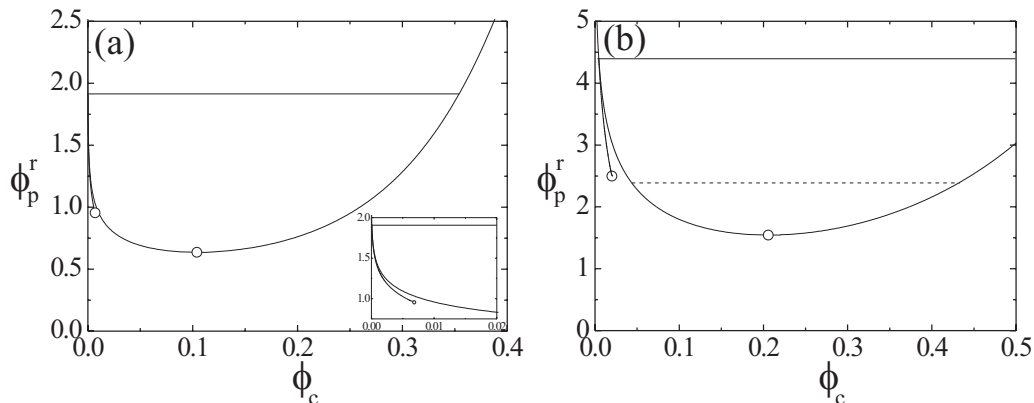


FIGURE 4.6. Wetting phase diagrams in polymer reservoir representation with $q = 1$ both for (a) ideal and (b) EVI-polymers. The full horizontal lines denote the location of the wetting transition. Mixtures are partially wetting above and completely wetting below these lines. The dashed line in (b) depicts the location of the triple line (crystal-fluid coexistence is not shown for the sake of clarity). The lines at the left/gas side of the phase diagrams represent the prewetting line starting from the wetting transition and ending in the prewetting critical point. The inset in (a) shows a zoom in on this area. The open circles depict critical points.

the arrow in figure 4.2 with a density higher than the bulk liquid density) costs more inhomogeneities (area B) which are balanced by a favourable interaction with the wall (area C).

For mixtures slightly off-coexistence in the gas phase the prewetting line can be calculated in the same way as the wetting transition [9]. Now, only one true minimum appears indicating the density of the gas phase and one local minimum indicating the density of the metastable liquid phase. Again, an equal area construction can be made to determine the location of the prewetting line, which starts at the wetting transition and ends in a prewetting critical point [125]. In figure 4.6 we show the theoretical phase diagram in polymer reservoir representation for $q = 1.0$ for (a) ideal polymers and (b) EVI-polymers. For ideal polymers a first order wetting transition is found at $\phi_{p,w}^r = 1.917$ with a prewetting line ending in a prewetting critical point. The wetting transition takes place rather close to the critical point; for comparison the triple line is at $\phi_{p,t}^r = 6.081$. The triple line is found by the crossing of the gas-liquid and the fluid-crystal coexistence (calculated as described in section 4.2). In [82] the wetting transition is found at $\phi_{p,w}^r = 0.85$, while in [105] it is found at $\phi_{p,w}^r = 1.05$. Clearly, we find the transition further away from the critical point than in [82, 105], but it is still much closer to the critical point than to the triple line. Furthermore, we calculate a prewetting line very close to the binodal whereas in [82, 105] a first order

wetting transition was found, but not the accompanying prewetting line. In addition, we find that increasing h_1 drives the wetting transition away from the critical point, while increasing g counteracts this effect. Of course, higher order terms in the contact density are present for the relatively large size ratio $q = 1$, where mutual overlapping depletion zones of three and more particles are likely to occur, and taking these into account would even give better agreement with the predictions in [82, 105].

In contrast, for EVI-polymers higher order terms contribute little. For example, for EVI-polymers the g -term does not change anymore with increasing polymer concentration from the bulk critical point on, see figure 4.4. Moreover, g is very small compared to the result for ideal polymers (0.050 instead of $0.606 \times \phi_p^r$, figure 4.4). This means that the wetting transition for EVI-polymers is mainly driven by the h_1 term. The direct consequence of this is that the transition occurs far away from the critical point, at $\phi_{p,w}^r = 4.403$ (indicated by the horizontal full line in figure 4.6(b)), which is even above the triple line, located at $\phi_{p,t}^r = 2.388$ (indicated by the horizontal dashed line in figure 4.6(b)). Note that in our calculations we can ignore the crystal phase and we are thus able to determine the location of the wetting transition even if it is above the triple line. Furthermore, the prewetting line is more extended than for ideal polymers and does not follow the binodal so closely. Wijting *et al.* [108, 109] find a wetting transition in a colloid-polymer mixture similar to system 1 SPC13, but with $q = 0.93$ and transform the experimental polymer concentration back to a theoretical reservoir polymer concentration thus locating the wetting transition between $4.3 < \phi_{p,w}^r < 4.5$. For $q = 0.93$ we find the transition at $\phi_{p,w}^r = 3.80$, which is again above the theoretical triple line. Yet in many experimental systems the crystalline phase seems to be suppressed by colloidal sphere polydispersity.

Finally, we give the results for the experimentally relevant $q = 0.6$, corresponding to systems 2 PPD25 and 3 PPD71. Here, a wetting transition is predicted to occur at $\phi_{p,w}^r = 0.91$ for ideal polymers, whereas the transition is located at $\phi_{p,w}^r = 0.60$ by the two component DFT treatment [82]. A different approach, using an analytic formula for the interfacial free energy of the colloid-polymer mixture in contact with a hard wall predicts a wetting transition at $\phi_{p,w}^r = 0.87$ [126]. Here, details of the layering structure in the vicinity of the wall are lost, as in our approach. For interacting polymers we find the wetting transition at $\phi_{p,w}^r = 1.615$, again above the triple line. The experimental relevance of these and the above results will be discussed in extended form in chapter 5.

4.5. CONCLUSIONS

We have calculated the interfacial tension of the free interface in phase separated colloid-polymer mixtures within a squared gradient approach. For ideal polymers we find reasonable agreement with a much more sophisticated approach [82]. Moreover, by

using a recently developed extension of the free volume theory for ideal polymers to excluded volume interacting polymers [111], see also chapter 3, the polymer is incorporated much more realistically into the theory and the predicted bulk phase behaviour agrees better with experiment. This first step should be taken when one wants to compare the predicted interfacial tensions with experimental values. Making this comparison for the interfacial tension we see that the ideal polymer description overestimates, while the EVI-polymer description underestimates the experimental data. The two different methods used to measure the interfacial tension in exactly the same system do not agree completely showing that measuring such ultra-low interfacial tensions is very difficult.

Furthermore, we have put the often used qualitative interpretation of wetting in colloid-polymer mixtures based on particle wall overlap volumes and hence microscopic interactions into an insightful, semi-phenomenological, quantitative form within the Cahn-Fisher-Nakanishi formalism. This way we clearly see which terms drive the transition to or away from the critical point. For ideal polymers we find that the location of the wetting transition is somewhat further away from the critical point than predicted by the theory of [82] and by the computer simulations of [105], but still much closer to the critical point than to the triple line. We thus see that the two particle-wall term alone is not enough to drive the transition back towards the critical point and that higher order terms -although smaller- are important. Again, we can extend this model to incorporate EVI-polymers. In this case, the two-particle wall term is already very small, higher order terms are even smaller and hence the wetting transition is driven away from the critical point by the attractive particle-wall term even to above the triple line. In experiment, however, a wetting transition is found [108, 109], but in a system which does not display a crystal phase. We calculated the wetting transition for that system by ignoring the crystal phase. We then found a wetting transition reasonably close to the experimentally found one. Furthermore, in [109] it is mentioned that the pictures of the gas-liquid interface are somewhat fuzzy and we feel that experimentally the challenge is in accurate measurements of the contact angle as will be discussed in chapter 5. Theoretically, the challenge is to describe polymers even more realistically in order to obtain not only a better overall agreement with the experimental bulk phase behaviour, but also with the measured interfacial tensions.

APPENDIX: EQUATION (4.19) FOR $q = 1$

For $q = 1$ we can calculate equation (4.19) analytically. First we calculate all volumes of type 3, see figure 4.7(a), as if particles 1 and 2 do not feel each other and next we subtract all volumes 3 where particles 1 and 2 did penetrate each other. For the first calculation we do not perform the calculation with z_1 as the axis of symmetry, but we choose the axis of symmetry around a ghost particle, particle 3, at the other side of the depletion layer, see figure 4.7(b). If particles 1 and 2 lie within the shaded volume, V_s , in figure 4.7(b), then their depletion zones certainly overlap at the centre of particle 3. Doing this for all positions of particle 3, with z_3 the distance of particle 3 to the depletion wall, gives the first part of the integration:

$$\int_0^{\sigma_c} dz_3 V_s^2(z_3) = \int_0^{\sigma_c} dz_3 \left(\frac{\pi}{3} (\sigma_c - z_3)^2 (2\sigma_c + z_3) \right)^2 = \frac{11}{105} \pi^2 \sigma_c^7. \quad (4.24)$$

This is exactly the same calculation (in a different way) as done by Bellemans in [123]. The second part of the integration can be understood as follows. We let ghost particle 3 scan the volume behind the depletion wall, see figure 4.7(c), but then particle 3 should always be within a diameter σ_c of particles 1 and 2, just as particle 1 should be within σ_c of 2 and 3, and 2 with respect to 1 and 3. Thus, all particles are identical. One can easily see that if we put and keep particle 2 behind the wall as in figure 4.7(d) and let particle 3 scan the overlap volume between particles 1 and 2 behind the wall for all positions of 1 and 2 -let us call this integration *a*- that this integration is exactly the same as letting particle 3 scan before the wall again for all positions of particles 1 and 2, called integration *b*. Because of symmetry these integrations are exactly equal to integration *c* with particles 1 and 2 before and particle 3 behind the wall, depicted

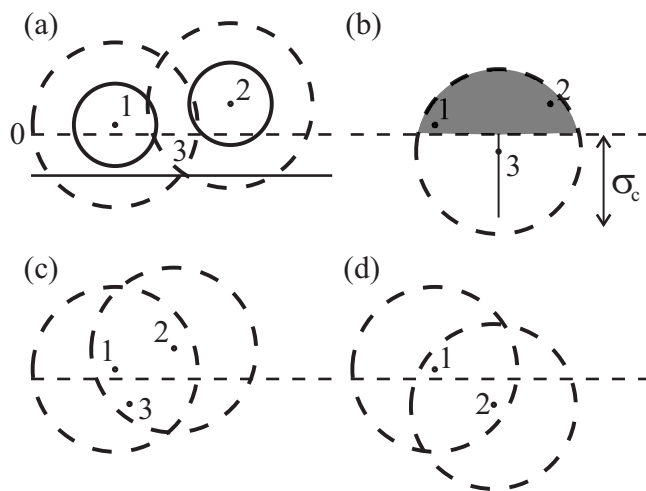


FIGURE 4.7. Pictures to support the derivation given in this Appendix. Dashed lines mark depletion zones. The horizontal dashed line marks the depletion layer of the wall and particle-wall distances are relative to this line.

in figure 4.7(c), which we want to know. We can easily do integrations a and b together since the total overlap volume between 1 and 2 is straightforward and $a + b$ becomes:

$$a + b = \int_0^{\sigma_c} dz_1 \int_0^{\sigma_c - z_1} dz_2 V_o(z_1, z_2) 2\pi(z_1 + z_2)z_2 = \frac{61}{420}\pi^2\sigma_c^7, \quad (4.25)$$

with $V_o(z_1, z_2)$ the overlap volume between particles 1 and 2, z_x the distance of particle x to the depletion wall and $2\pi(z_1 + z_2)z_2 dz_2$ the number of points 2 in a shell around particle 1. Bellemans calculated $a + b + c$ in [123] in a different way. Now, $c = \frac{1}{2}(a + b)$ and our integration (4.19) becomes

$$\left(\frac{11}{105} - \frac{61}{840}\right)\pi^2\sigma_c^7 = \frac{9}{280}\pi^2\sigma_c^7. \quad (4.26)$$

5

The capillary length and wetting behaviour in colloid-polymer mixtures: Experiment

ABSTRACT

We study two different gas-liquid phase separating colloid-polymer mixtures in the vicinity of a vertical hard wall. We use a horizontally placed microscope in either the transmission light or in the laser scanning confocal mode. The first technique is applied on a non-fluorescent system of silica colloids and poly(dimethylsiloxane) polymer in cyclohexane and enables us to measure the capillary length. The second technique is used for a fluorescent system of poly(methylmethacrylate) colloids and poly(styrene) polymer in decalin and allows for precise contact angle measurements as well. This colloid-polymer mixture shows complete wetting for all statepoints measured. The interfacial profiles are accurately described by the interplay between the Laplace and hydrostatic pressure and from this description the capillary lengths are obtained. For different statepoints approaching the critical point the capillary length varies from 50 to 5 μm . These results are compared to the theory presented in chapter 4.

5.1. INTRODUCTION

The study of colloid-polymer mixtures in the vicinity of walls is of fundamental as well as practical importance. Fundamental importance arises from the analogy between molecular fluid-fluid systems and phase separated colloid-polymer mixtures. In a classical paper, which also contains references to much earlier work, Vrij pointed out the importance and relevance of this analogy [19] (for a recent review, see [26]). Moreover, the depth and range of the interactions are tunable, which makes the mixtures ideal for

testing theories about wetting [127, 128]. The origin of the phase separation in colloid-polymer mixtures lies in the polymer mediated colloid-colloid depletion attraction as first described by Asakura and Oosawa [24, 25] and Vrij [19]: polymers are excluded from a region around the colloids for entropical reasons and two colloids within a certain distance of each other are effectively pushed together by the polymer osmotic pressure. The coexisting phases in this work are a colloidal liquid (rich in colloid and poor in polymer) and a colloidal gas (poor in colloid and rich in polymer). The resulting wetting behaviour can be very rich and it recently gained attention from theory [129, 130], experiment [106–109] and simulations [105].

Studying these systems close to walls is of practical importance as well since the food industry, for example, extensively uses the properties of both colloids and polymers to induce gelation or creaming [131, 132] and walls clearly play an important role, e.g. in confining the products, which has implications for the products' shelf-life. Furthermore, it is conjectured that in the living cell microcompartmentation is the result of phase separation and it is evident that wetting properties play a crucial role in the structure of the cell [133].

Close to a vertical solid surface the interface between two fluids or between a gas and a liquid is curved. The exact shape of the interfacial profile, i.e. the meniscus, is determined by the interplay between the Laplace and the hydrostatic pressure. The characteristic length scale of the meniscus, the capillary length L_c , is given by

$$L_c = \sqrt{\frac{\gamma}{g\Delta\rho}}, \quad (5.1)$$

with γ the interfacial tension, g earth's acceleration and $\Delta\rho$ the mass density difference between the bottom and top phase. For molecular fluids the interfacial tension and the density difference are typically of the order of 10-100 mN/m and 0.1-1 g/ml, respectively, leading to a capillary length of ~ 3 mm, which is also the capillary length of water in contact with clean glass. In colloid-polymer mixtures γ is much smaller, since far away from the critical point it has a typical magnitude proportional to [3, 12]

$$\gamma \sim \frac{k_B T}{\sigma_c^2}, \quad (5.2)$$

where $k_B T$ is the thermal energy and σ_c the particle diameter. This order of magnitude has been confirmed in experiment [35–38, 106, 134], theory [102, 103, 120, 129, 130] and recently in computer simulations [135, 136]. For colloids that are about a hundred times larger than molecules the capillary length thus becomes approximately a hundred times smaller, i.e. $\sim 30 \mu\text{m}$.

In this chapter the capillary length is measured in two different fluid-fluid phase separated colloid-polymer mixtures by analyzing the meniscus close to a vertical wall. This is done by means of transmission light microscopy on a mixture of silica colloids

and poly(dimethylsiloxane) polymer in cyclohexane, system 1 SPC13, and by means of laser scanning confocal microscopy on a system of poly(methylmethacrylate) (PMMA) colloidal spheres and poly(styrene) polymer in decalin, system 2 PPD25 in chapter 2. This allows us to look at the wetting behaviour as well and see whether or not the system shows partial or complete wetting, which will be discussed in light of the theoretical findings in chapter 4. The interfacial tensions determined for system 1 have already been compared to theory in the previous chapter [130]. In this chapter the measured capillary lengths in system 2 are compared with theory, that has been presented in chapter 4. The aim of this work is two-fold: to quantify the measured capillary lengths *and* determine the wetting state of the mixture. We will show results for system 1 first followed by a more elaborate study on system 2.

The chapter is organised as follows. We will start with a description of the experimental methods in section 5.2. The results will be presented in section 5.3 and the further analysis and discussion will be given in section 5.4. Concluding remarks are made in section 5.5.

5.2. EXPERIMENTAL SYSTEM AND TECHNIQUE

In figure 5.1 the experimental phase diagrams are shown for systems 1 SPC13 (a) and 2 PPD25 (b) including the dilution lines along which the capillary lengths have been determined. Here, ϕ_c denotes the colloid volume fraction and ϕ_p the polymer volume fraction with respect to its overlap concentration. In (a) the open symbols denote the experimental binodal [36], the closed symbols denote the measured statepoints and the cross indicates a statepoint in the one-phase region. In (b) the full curve denotes the approximate location of the binodal with stable mixtures to the left (crosses) and phase-separating mixtures to the right. Capillary lengths have been determined for the open symbols.

The difference in the location of the experimental binodals is considerable. In (a) the experimental critical point lies at $\phi_c^{cp} \approx 0.20$, $\phi_p^{cp} \approx 1.38$, in (b) it is estimated to be at $\phi_c^{cp} \sim 0.1$, $\phi_p^{cp} \sim 0.36$. Especially the difference in the polymer concentration is remarkable. Such differences are found in general when comparing experimental phase diagrams for silica spheres + poly(dimethylsiloxane) polymer in cyclohexane (system 1) and PMMA spheres + poly(styrene) polymer in decalin (system 2), see for example also the phase diagrams in [60] (similar to system 1) and in [50] (similar to system 2, see also figure 3.5(a)), where such differences are observed for more comparable polymer-to-colloid size ratios and colloidal polydispersities. A reason for this difference lies perhaps in the fact that poly(styrene) in decalin is still relatively close to θ -conditions, whereas poly(dimethylsiloxane) is in the excluded volume limit, as explained in chapter 2.

To study the interfacial properties of the colloid-polymer mixtures we use the microscopy setup as described in chapter 2. We use the light transmission mode for

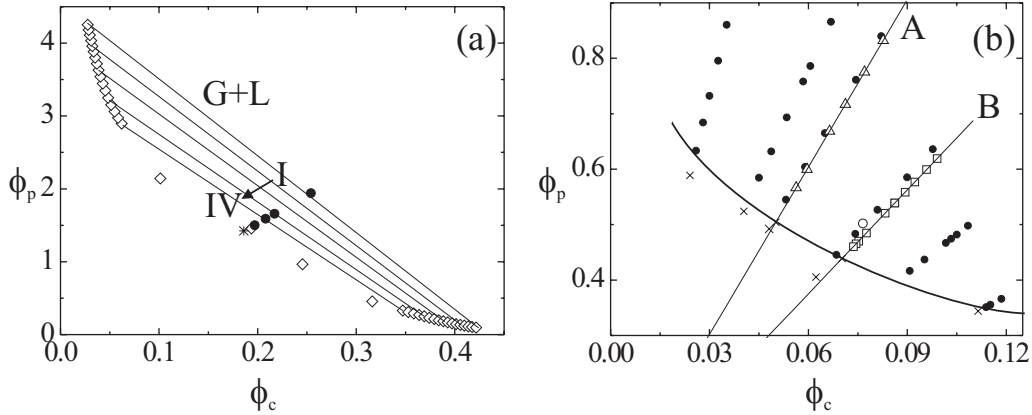


FIGURE 5.1. Phase diagrams in (ϕ_p, ϕ_c) -representation for system 1 SPC13 (a) and 2 PPD25 (b) as described in chapter 2. (a) The open symbols denote the experimental binodal. State points to which references are made in the text are indicated. Tie-lines are shown as well. (b) Indicated are points where gas-liquid phase separation occurs (open and filled symbols), and statepoints in the one-phase region (crosses). Lines A and B are two dilution lines along which the capillary lengths have been measured. The full curve is an estimate of the binodal and is drawn to guide the eye.

system 1 SPC13 and the laser scanning confocal mode for system 2 PPD25. Glass cells (of volume $\sim 1 \text{ cm}^3$) were used, both with and without stearyl-coated glass walls, which did not lead to essential differences, probably since the refractive index difference between solvent and colloids was very small and van der Waals interactions were thus minimal. The laser scanning confocal microscope (LSCM) detects the fluorescence of excited dye in the colloids, while solvent and polymers remain dark. Hence the colloidal rich phase (liquid) appears bright, whereas the colloidal poor phase (gas) appears dark.

After phase separation had completed, the interface looks very sharp by visual inspection even close to a wall, see figure 5.2(a) and (c). Using a microscope enables resolving the details of the interfacial profile close to the wall and in figure 5.2(b) and (d) the colloidal liquid phase is seen to favour the wall. The qualitative understanding of this phenomenon becomes apparent by considering all the depletion zones in play. The overlap at contact between the depletion zone of a spherical colloidal particle and a wall is larger than the overlap between the depletion zones of two touching colloidal spheres (see also figure 4.1). Thus, the colloidal rich phase, the liquid, favours the wall. In fact, in (d) the liquid phase even wets the wall completely, although it is not yet clear whether or not the system is in true equilibrium given the thickness of the liquid layer ($\sim 2 \mu\text{m}$) and the fact that it does not get considerably thinner higher up in the sample. Furthermore, LSCM reveals that the connection between the interfacial profile and the wetting layer appears to have a very small dimple, see the inset in figure 5.2(d).

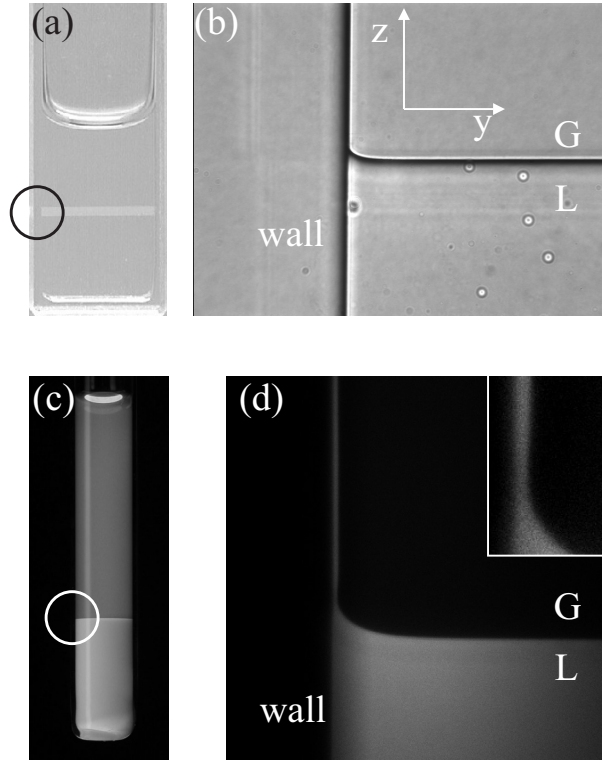


FIGURE 5.2. Photographs of two phase separated colloid-polymer mixtures of system 1 SPC13 (a), which is slightly tilted to show the interface better, and 2 PPD25 (c) taken under UV-light. (b) and (d) are “blow-ups” of the encircled regions by means of transmission light microscopy and LSCM, respectively. The image dimensions are $706 \times 528 \mu\text{m}^2$ (b) and $350 \times 350 \mu\text{m}^2$ (d). The inset in (d) is a zoom in ($73 \times 108 \mu\text{m}^2$) on the region where the interfacial profile joins the liquid layer at the wall.

The liquid layer at the wall and the dimple will be discussed in section 5.4. Nonetheless, even during (the final stages of) phase separation the interfacial profile has a very similar shape, governed by the balance between the Laplace and the hydrostatic pressure, indicating that mechanical equilibrium rapidly sets in. Wijting *et al.* [108, 109] used transmission light microscopy to study the interfacial profile in colloid-polymer mixtures, but the contour of the profile remained somewhat fuzzy [109]. Their focus was on the contact angle and no capillary lengths were measured. Clearly, LSCM has the advantage over light microscopy that a thin slice can be imaged [74], see also the differences between figure 5.2(b) and (d).

5.3. RESULTS

The shape of the capillary meniscus is described by the interplay between the hydrostatic and the Laplace pressure. Close to the wall the disjoining pressure acts on the wetting film. Within a transition zone both the capillary forces and the surface

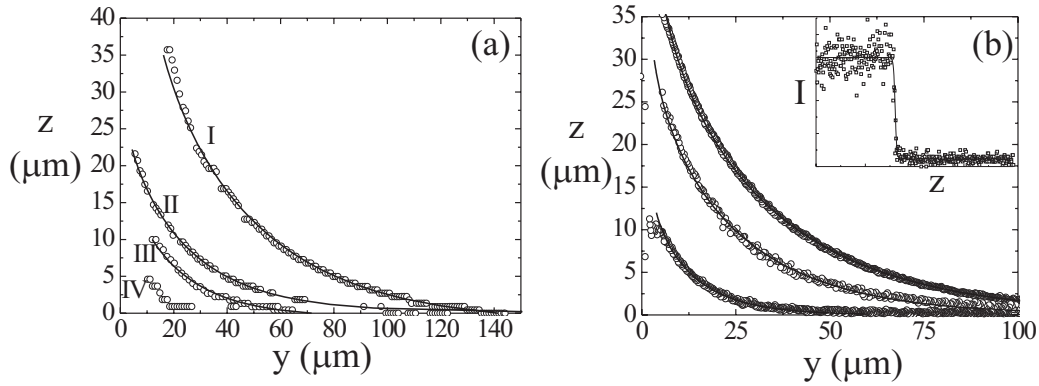


FIGURE 5.3. Interfacial profiles (symbols) from light microscopy (a, system 1 SPC13) and LSCM (b, system 2 PPD25) from images such as in figure 5.2(b) and (d) for several different statepoints. In (b) profiles are shown along dilution line B in figure 5.1(b) corresponding from top to bottom to statepoints 3, 6 and 8. The full curves follow from (5.4). The inset shows the intensity I along a single column in figure 5.2(d) (symbols) described by a hyperbolic tangent function (full curve).

force are active [137–139]. Measurements of equilibrium contact angles and interfacial shapes of bulk liquids should be carried out outside this transition zone. Outside the transition zone we obtain the following differential equation by equating pressures [39]

$$\Delta\rho g z = \gamma/R(z) \quad (5.3)$$

for the profile at a flat wall with $R(z)$ the radius of curvature at height z above the interface. The analytic solution for this problem is given in terms of $y(z)$ with y the distance to the wall and is [39]

$$\frac{y}{L_c} = \left[\operatorname{arccosh}\left(\frac{2L_c}{z}\right) - \operatorname{arccosh}\left(\frac{2L_c}{h}\right) + \left(4 - \frac{h^2}{L_c^2}\right)^{\frac{1}{2}} - \left(4 - \frac{z^2}{L_c^2}\right)^{\frac{1}{2}} \right], \quad (5.4)$$

with the capillary rise $h \equiv z(0)$. The shape of the profile only depends on L_c , which thus can be found by fitting only a part of the profile. By extrapolating the profile to the wall one also obtains h and by the relation

$$h^2 = 2L_c^2(1 - \sin\theta), \quad (5.5)$$

the contact angle θ can be measured. From figure 5.2(b) and (d) the interface can be accurately located. The open circles in figure 5.3 denote the interface from experiment. In the LSCM experiment the interface can for example be located by fitting the intensity along a column in the z -direction to a hyperbolic tangent function, which is shown as an inset in figure 5.3(b), and the position of the wall can be determined using a similar method. Then we can either fit equation (5.4) directly to this profile with L_c and h as fitting parameters or define h and fit equation (5.4) with L_c and the position of the

TABLE 5.1. Overall volume fractions of colloid (ϕ_c) and polymer (ϕ_p), gas-liquid density differences $\Delta\rho$ in g/ml, experimental capillary lengths in microns and interfacial tensions in $\mu\text{N/m}$. All samples lie on the same dilution line, see figure 5.1(a). Results for system 1 SPC13.

sample	ϕ_c	ϕ_p	$\Delta\rho$	L_c	γ
I	0.25	1.94	0.32	32.9	3.38
II	0.22	1.66	0.26	26.5	1.76
III	0.21	1.59	0.23	16.0	0.58
IV	0.20	1.50	0.20	-	-

wall (a constant in the right hand side of (5.4)) as fitting parameters. We here followed the second option and by comparing the fitted position with the actual position of the wall it is possible to obtain the actual h and hence the contact angle.

For system 1 SPC13 the experimental interfacial profiles obtained from light microscopy images are quite well described by (5.4) as can be seen in figure 5.3(a). Approaching the critical point we observe that the capillary length decreases. It becomes too difficult to resolve the profile of statepoint IV by light microscopy. From the experimental binodal and tie-lines (as constructed by de Hoog and Lekkerkerker [36]) the density differences can be obtained, and via (5.1) the interfacial tensions as well, see table 5.1. The contact angle depends very sensitively on the exact position of the wall and can change drastically close to the wall (for example, 30° in only $2 \mu\text{m}$ for sample II). Since we cannot locate the wall accurately enough with the light microscopy setup the contact angle remains intangible and we cannot say whether the interface is partially or completely wetting the wall and if there is a wetting transition upon approach of the critical point.

For system 2 PPD25 the experimental interfacial profiles obtained from LSCM are very well described by (5.4) as can be seen in figure 5.3(b). The measured capillary lengths for the dilution lines shown in figure 5.1 are given as a function of the overall colloid and polymer volume fraction in table 5.2. Following the dilution line from high to low ϕ_c , tie-lines are crossed and the critical point is approached, although the dilution lines do not intersect this point. As a result the capillary length strongly decreases, but not all the way down to zero. With the LSCM-technique we succeed in measuring capillary lengths down to just a few micrometers. As mentioned above, the apparent contact angle changes drastically close to the wall. This illustrates the necessity of using a fit-function in order to obtain the contact angle. Furthermore, the position of the wall must be precisely located. The LSCM technique enables us to measure the contact angle accurately. We find that all our samples measured show complete wetting.

TABLE 5.2. Overall volume fractions of colloid (ϕ_c) and polymer (ϕ_p) and experimental capillary lengths in microns for dilution lines A and B, see figure 5.1(b), obtained for system 2 PPD25.

sample	A			B		
	ϕ_c	ϕ_p	L_c	ϕ_c	ϕ_p	L_c
1	0.083	0.83	49.3	0.099	0.62	40.6
2	0.077	0.78	48.6	0.096	0.60	37.0
3	0.071	0.72	39.6	0.092	0.58	33.2
4	0.066	0.67	33.8	0.089	0.56	32.0
5	0.060	0.60	25.2	0.086	0.54	26.6
6	0.056	0.57	21.7	0.083	0.52	25.4
7				0.078	0.48	15.1
8				0.075	0.47	12.2
9				0.074	0.47	9.7
10				0.074	0.46	6.1

5.4. ANALYSIS AND DISCUSSION

5.4.1. Capillary lengths

The first set of experimental data has been obtained for system 1 SPC13. The gas-liquid density differences are known for each state-point and the interfacial tension can thus be extracted from the capillary length measurements using (5.1). We have compared the interfacial tensions to theory in chapter 4 (see figure 4.3). There, theory models the polymers as excluded volume interacting (EVI) polymers instead of ideal polymers since this improves the bulk phase behaviour considerably (see figure 3.5(d)). The experimental interfacial tensions are reasonably well described by theory.

The second sets of measured capillary lengths have been obtained for system 2 PPD25. Unfortunately, the method of Bodnar and Oosterbaan [60] to determine the binodal and tie-lines did not give physically acceptable results. Hence, we choose to make the comparison to theory on the level of the capillary lengths and directly along the dilution lines as a function of the overall concentration of colloids. The theory presented in chapter 4, sections 4.2 and 4.3, can be directly used for this purpose.

In chapter 3 it was observed that the EVI-polymer model predicted a binodal at too high polymer concentrations lying in general above the measured state-points for system 2. For ideal polymers the calculated binodal was in closer agreement with the experimental binodal, see figure 3.5(b). Since we want to make the comparison directly at the level of dilution lines we can only use the ideal polymer description. In figure 5.4 the theoretical interfacial tension γ , the gas-liquid density difference $\Delta\rho$ and the capillary length L_c using (5.1) are plotted as a function of volume fraction of

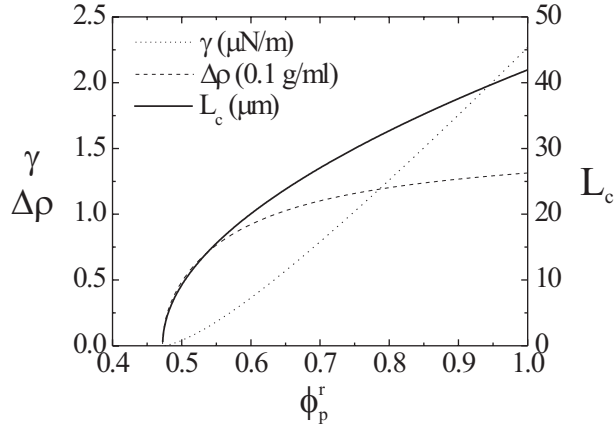


FIGURE 5.4. Interfacial tension, density difference (in units of 0.1 g/ml) and the resulting capillary length as a function of the volume fraction of polymer in the reservoir ϕ_p^r with colloid diameter $\sigma_c = 50$ nm as in the experimental system (PPD25). More experimental details can be found in chapter 2.

polymer in the reservoir. Note that the prediction of the interfacial tension is in good agreement with density functional theory calculations by Brader *et al.* [129], where the colloid-polymer mixture was described as a two-component system within fundamental measure theory. Furthermore, for homogeneous phases this density functional [104] reduces to the free volume theory [18], such that the bulk phase behaviour and the density difference found in the present work, will be found from the density functional theory as well. Approaching the critical point we find that both γ and $\Delta\rho$ decrease according to their mean-field exponents (i.e. 1.5 and 0.5, respectively), in agreement with calculations by Brader and Evans [103], leading to a decrease of the capillary length as well (with an exponent 0.5). It is straightforward to convert the capillary lengths of figure 5.4 as a function of ϕ_p^r into a function of overall ϕ_c along a dilution line. Each capillary length corresponds to a certain tie-line and by determining the intersection between that particular tie-line in the system variable concentrations (see chapter 3) and the dilution line, we obtain L_c as a function of ϕ_c for that dilution line.

We show the results for dilution lines A and B in figure 5.5. The symbols stem from the experiment (table 5.2) and the full curves follow from the theory presented in chapter 4 for the present experimental system and dilution lines. Clearly, the theoretical prediction is in qualitative agreement with experiment; the theoretical capillary length has the right order of magnitude and follows a similar shape as a function of ϕ_c . Given the reasonable, but not perfect agreement between the theoretical and experimental binodal (figure 3.5(b)) the differences are not surprising. In particular, the experimental data points in figure 5.5(b) strongly decrease, since the dilution line intersects the experimental binodal relatively close to the experimental critical point (estimated at

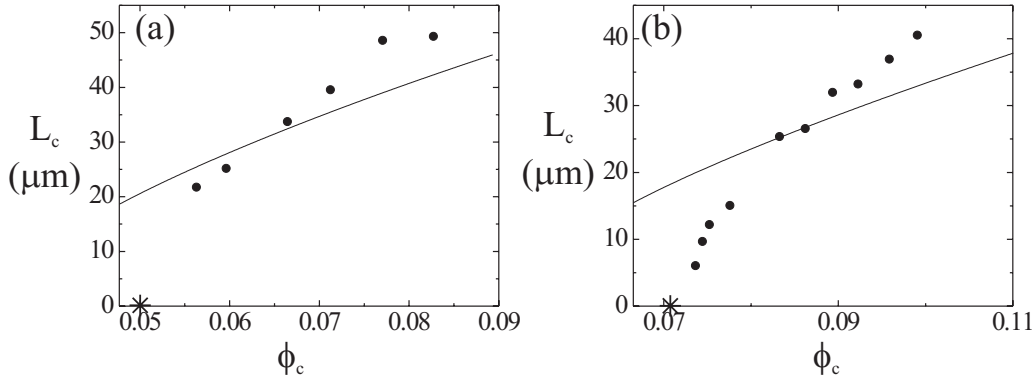


FIGURE 5.5. Capillary lengths (table 5.2) for dilution lines A (a) and B (b) (figure 5.1(b)) as a function of the overall concentration of colloids ϕ_c . The symbols follow from measurements as in figure 5.3(b) and the full curves directly stem from theory without an adjustable parameter. The stars at the horizontal axes denote the first observations of stable colloid-polymer mixtures along dilution lines A and B, which are good indications of the location of the experimental binodal points that will lie just above the stars. The theoretical curves stop at the vertical axis at an overall ϕ_c , where the experimental dilution line intersects the theoretical binodal. Results for system 2 PPD25.

$\phi_c^{cp} \sim 0.1$, $\phi_p^{cp} \sim 0.36$). The theoretical curve is calculated with respect to the theoretical critical point (located at $\phi_c^{cp} = 0.20$, $\phi_p^{cp} = 0.16$), which is more to the right in the phase diagram.

Next, we analyze where the discrepancy between theory and experiment stems from. Therefore, the gas and liquid densities have been measured for one state-point ($\phi_c = 0.076$ and $\phi_p = 0.50$, open circle in figure 5.1(b)). The results are summarized in table 5.3. The theoretical and experimental capillary length lie quite close together. However, both the theoretical density difference and interfacial tension overshoot the experimental measurements and these effects cancel to some extent. In particular, the discrepancy of the liquid densities is large, which is a direct consequence of the mismatch

TABLE 5.3. Comparison between experiment and theory. The capillary lengths are in μm , the densities in g/ml and the interfacial tensions in $\mu\text{N/m}$. Note that the experimental interfacial tension (obtained from the capillary length) is in good agreement with an analysis of the thermal capillary wave-spectrum, following the method of [134], for which $\gamma \sim 0.2 \mu\text{N/m}$ is obtained. Results for system 2 PPD25.

	L_c	ρ_L	ρ_G	$\Delta\rho$	γ
Experiment	18	0.942	0.889	0.053	0.16
Theory	23	0.992	0.891	0.101	0.50

between the theoretical and experimental binodal as shown by the difference in critical points. Of course, the experimental volume fractions have been found by directly converting the colloid mass fractions, as explained in chapter 2. Since this system does not display a crystal phase –possibly related to the colloid’s size polydispersity– the volume fractions have not been scaled on for example the freezing volume fraction [71]. This could in principle expand the experimental binodal more to the right, but here we have kept the comparison as direct as possible. It is also possible to calculate the theoretical interfacial tension for a given density difference. In that case we find $\gamma = 0.053 \mu\text{N/m}$, such that the capillary length would be $10 \mu\text{m}$ for the statepoint indicated in the table.

The differences between experiment and theory indicate that the applied theory does not completely capture all the details of the experimental system. This leads to differences in the binodals as well as in the interfacial tensions. It is unclear what details of the colloid-polymer mixture have to be included in theory to obtain a more quantitative agreement with experiment. We will speculate upon this in the next section.

5.4.2. Wetting behaviour

As discussed above we cannot determine the contact angle in system 1 SPC13, but this is possible in system 2 PPD25. All our samples measured show complete wetting. This is in contrast with predictions of Brader *et al.* [129] (see also the extension by Wessels *et al.* [140]), who calculated a wetting transition reasonably close to the critical point both for polymer-colloid size ratio $q = 1.0$ and $q = 0.6$, which is close to the experimental q of 0.56. This was later confirmed by Dijkstra and van Roij [105] in extensive computer simulations, who found a 20 % different location of the wetting transition for $q = 1.0$. In the Cahn-theory presented in chapter 4 we found similar results, although the transitions were predicted to occur at slightly higher polymer volume fractions, but still in the measured range of polymer concentrations. However, in these calculations and simulations the polymer was described as an ideal polymer, i.e. a mutually penetrable hard sphere. Such a simplified polymer model gives a qualitative description of the bulk phase behaviour (chapter 3) and of the capillary length, as shown above, and provides reasonable predictions. Therefore, we feel that the prediction of a wetting transition within the ideal polymer model can also be a qualitative guide in the experiment. Quantitatively, however, the wetting transition may well be found elsewhere.

For example, if polymer-polymer interactions are taken into account, then this has clear effects on the bulk phase behaviour. Several theories are available in literature that provide a more realistic description of the polymer when calculating the phase behaviour (see the reviews of [26, 32–34] and references therein, see also the results in chapter 3). These show in one way or another a shift upwards of the binodal with respect to an ideal polymer calculation. More recently, several theories predict that the interfacial tension

decreases when taking polymer interactions into account [120–122, 130] (chapter 4). Finally, the wetting transition within a Cahn-model [9] for mixtures of colloids and excluded volume interacting polymers is predicted to occur far away from the critical point, even to above the triple point (see chapter 4). In sum, the experimental data of this chapter nor the theory presented in chapter 4 discuss the existence of the wetting transition, but merely question its exact location in relation with the theoretical models and the experimental complexity. In [108, 109] a wetting transition was reported in a colloid-polymer mixture very similar to system 1 SPC13, although the subtleties of the interfacial profile in reference to the contact angle -as explained above- were perhaps not fully realised, since contact angles were determined by hand.

Finally, we would like to discuss some experimental phenomena, which are not yet understood. The liquid layer at the wall is surprisingly thick and does not get considerably thinner higher up in the sample as mentioned in section 5.2. This may indicate that the system did not yet reach complete equilibrium. Related to this is the observation that after the liquid drops have stopped dripping down from the dispersion-air meniscus as described in chapter 8, liquid material remains hanging at the lowest part of the meniscus at least for over a month. It is difficult to estimate the time needed to reach complete equilibrium, especially given the intrinsic slowness of colloidal suspensions (chapter 1). For example, in [141] it was shown that under the influence of gravity a system of colloidal platelets found its equilibrium phase coexistence only after a year. Furthermore, the connection between the interfacial profile and the wetting layer shows a very small dimple, see the inset in figure 5.2(d). Several ideas have been proposed in order to explain the liquid layer at the wall, or the dimple, or both phenomena: an effect of the disjoining pressure [142], or the line tension [138, 143, 144], a Marangoni effect [145], a size fractionation effect [146], a (very slow) drainage of the film or an effect of the thermal roughness of the interface. Several of these points are still open, although the disjoining pressure should be quite considerable to work over such thick wetting layers. Furthermore, the Marangoni effect and the drainage could not be confirmed by bleaching experiments of the liquid layer as well as of the bulk gas and liquid phases, although the diffusion might of course be faster than the flow in the layer. Attempts are being made to control the temperature more accurately. Furthermore, we are currently investigating the role of fluctuations on the wetting layer thickness.

5.5. CONCLUSION

We studied two different gas-liquid phase separating colloid-polymer mixtures in the vicinity of a vertical hard wall. The difference between the location of the mixtures' binodals is somewhat remarkable and possibly a direct consequence of the polymer properties. Precise measurements of the capillary length are obtained by analyzing

the interfacial profiles. The profiles are accurately described by the interplay between the Laplace and the hydrostatic pressure. The interfacial tensions that followed for system 1 SPC13 were compared in chapter 4 with theory, where a reasonable agreement was found. No contact angles are measured in this system, since the wall cannot be located accurately enough with light microscopy. In the more elaborate study for system 2 PPD25 with LSCM the capillary lengths vary between 50 and 5 μm for different statepoints approaching the binodal. We see that theory, in which the comparison is direct and descriptions are kept as simple as possible, already gives a qualitative description of the experimental data without the use of an adjustable parameter. A more detailed comparison for a single statepoint shows that theory overestimates both the density difference and the interfacial tension. These effects compensate each other to some extent when calculating the capillary length.

In system 2 PPD25 the position of the wall can be accurately located, which allows for precise measurements of the contact angle. We find complete wetting for all statepoints measured, in contrast with theoretical predictions in which the polymer is modelled as a mutually penetrable hard sphere. It is unclear what details of the colloid-polymer mixture have to be included in theory in order to obtain an overall quantitative agreement, not only with the bulk phase behaviour, but also with the interfacial tension and the precise location of the wetting transition. One may think of taking polymer-polymer interactions into account, but also sphere and polymer polydispersity might play a role. Finally, in our experiment not all phenomena are fully understood. Possibly the most interesting route is to explore the effects of the thermal roughness on the wetting properties, since this has a rather different character than in molecular systems as will be discussed in chapter 6.

6

Direct visual observation of thermal capillary waves

ABSTRACT

We studied the free fluid-fluid interface in a phase separated colloid-polymer dispersion with laser scanning confocal microscopy and directly observed thermally induced capillary waves at the interface in real space. Experimental results for static and dynamic correlation functions validate the capillary wave model down to almost the particle level. We are able to obtain the ultra-low interfacial tension, the capillary length and the capillary time, which are found to be in agreement with independent measurements.

6.1. INTRODUCTION

At rest, the free interface between any two fluids, like that between a liquid and its vapour, appears to be smooth. Yet thermal motion inevitably gives rise to statistical fluctuations of the local interface position and hence leads to a rough interface. This phenomenon was first predicted almost a century ago by von Smoluchowski [6] and it was Mandelstam who quantitatively described the interface roughness in terms of thermally excited capillary waves [7]. These capillary waves have been studied with light [147] and x-ray scattering [148–152]. They play a significant role in modern theories of interfaces [8, 153, 154] and have been argued to be essential in the rupture of thin liquid films [155, 156] as occurs in droplet coalescence. We show how to tune length- and timescales, by using colloidal suspensions, in such a way that the fluctuating fluid-fluid interfaces can be seen directly in real space with a resolution close to the particle size.

This chapter is organised as follows; We will start with a brief derivation of capillary wave theory in section 6.2 deriving the relevant expressions that we will use to analyse our data, followed by a description of the experimental system, i.e. system 3 PPD71, and the experimental methods in section 6.3. Results are presented in section 6.4 and conclusions will be drawn in section 6.5.

6.2. THEORETICAL BACKGROUND

We here follow the statistical analysis of interface corrugations, first developed by Mandelstam [7], as reviewed by Vrij [147]. The work ΔF to create a corrugation at constant temperature can be written as

$$\Delta F = \Delta F_g + \Delta F_c, \quad (6.1)$$

where we only consider gravity (ΔF_g) and capillary (ΔF_c) forces, resulting from the displacement of matter against gravity and the creation of extra interface area, respectively. Other contributions, for example arising from bending of the interface, are ignored, the validity of which will be discussed in section 6.5. Clearly, this is a mesoscopic approach, which is justified if one looks at distortions much larger than the particle size as is done in light scattering studies on molecular interfaces. The local interface position with respect to the mean interface position has coordinates $\mathbf{r} = (x, y, h(x, y))$, see figure 6.1. This Monge parametrization neglects overhang of the interface as well as bubbles of one phase in the other. To create a corrugation of an area $dxdy$ over a distance h gravity contributes

$$\delta F_g = \int_0^h h' g \Delta \rho dx dy dh' = \frac{1}{2} g \Delta \rho h^2 dx dy \quad (6.2)$$

with g earth's acceleration, and $\Delta \rho$ the mass density difference. The interfacial tension γ contributes

$$\delta F_c = \gamma \Delta A = \gamma dx dy \left(\sqrt{1 + h_x^2 + h_y^2} - 1 \right) \approx \frac{1}{2} \gamma dx dy (h_x^2 + h_y^2), \quad (6.3)$$

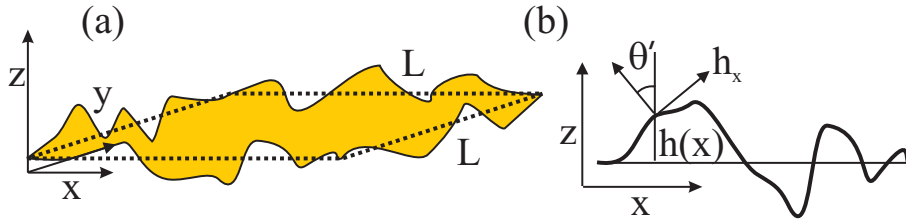


FIGURE 6.1. (a) Schematic depiction of a curved interface. A point at the interface \mathbf{r} is written in terms of $(x, y, h(x, y))$, i.e. the Monge parametrization. (b) A 2D slice out of (a). The projected angle θ' is related to the interface derivative h_x via $h_x = \tan \theta$.

with $h_i \equiv \partial h / \partial i$ and $i = x, y$. Integrating over the total interface area $L \times L$ gives

$$\Delta F_g = \frac{1}{2} g \Delta \rho \int \int dx dy h^2, \quad (6.4)$$

and

$$\Delta F_c = \frac{1}{2} \gamma \int \int dx dy (h_x^2 + h_y^2). \quad (6.5)$$

The height h can be expanded in a Fourier series in a square with length L as

$$h = \sum_{\mathbf{k}} h_{\mathbf{k}} e^{i(k_x x + k_y y)} \quad (6.6)$$

with $h_{\mathbf{k}}$ the Fourier coefficients and $\mathbf{k} = (k_x, k_y)$. The summation runs over all Fourier modes k_x and k_y . Using Parseval's identity it can readily be shown that

$$\Delta F = \frac{1}{2} L^2 \sum_{\mathbf{k}} |h_{\mathbf{k}}|^2 (g \Delta \rho + \gamma k^2), \quad (6.7)$$

with $k^2 = k_x^2 + k_y^2$ and $k = |\mathbf{k}|$. Mandelstam made use of the equipartition theorem which states that the work necessary to create each mode is equal to $k_B T / 2$, with k_B Boltzmann's constant and T the absolute temperature. Thus, in the capillary wave spectrum each Fourier component $h_{\mathbf{k}}$ of the interface displacement contributes

$$\langle |h_{\mathbf{k}}|^2 \rangle = \frac{k_B T}{\gamma L^2} \frac{1}{k^2 + L_{\parallel}^{-2}}, \quad (6.8)$$

where the brackets on the left hand side denote a thermal average and L_{\parallel} is the lateral correlation length (i.e. the capillary length L_c (chapter 1), which we give a different symbol in this chapter since it has the character of a correlation length). It is given through

$$L_{\parallel} = \sqrt{\gamma / (g \Delta \rho)}. \quad (6.9)$$

From (6.8) and again applying Parseval's theorem the mean square interfacial roughness is found to be

$$\langle h^2 \rangle = \frac{k_B T}{4\pi\gamma} \ln \left[\frac{k_{max}^2 + L_{\parallel}^{-2}}{k_{min}^2 + L_{\parallel}^{-2}} \right], \quad (6.10)$$

with $k_{min} = 2\pi/L$ and $k_{max} = 2\pi/l_m$. L denotes the physical system size and l_m is a microscopic length [8]. Thus, the interfacial roughness $L_T = L_{\perp} = \sqrt{\langle h^2 \rangle}$ is proportional to $\sqrt{k_B T / \gamma}$.

Since the interface is constantly subject to random forces the distribution $P(h)$ of the interface heights is described by a Gaussian with (6.10) its variance σ^2 . This means the distribution is given by

$$P(h) = \frac{1}{\sqrt{2\pi\sigma^2}} e^{-h^2/2\sigma^2}. \quad (6.11)$$

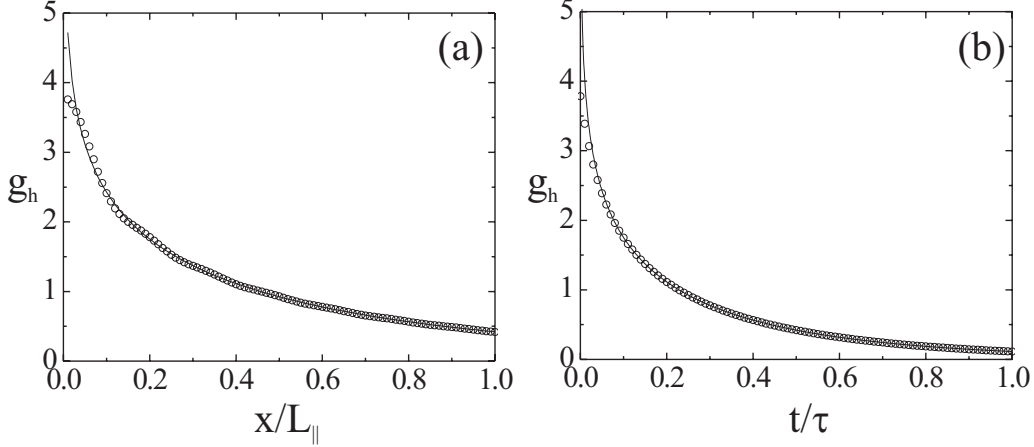


FIGURE 6.2. Static (a) and dynamic (b) height correlation functions g_h as a function of x/L_{\parallel} and t/τ in units of $k_B T/2\pi\gamma$. The symbols denote calculations in which k_{max} is set to $2\pi/\sigma_c$ leading to $\bar{k}_{max} = 44$, the full curves are for $\bar{k}_{max} = \infty$.

The next step is to look at derivatives of h for example in the x -direction [157], i.e. h_x , in which we are particularly interested since we only have information on $h(x, 0)$ as will be shown below. Given the cylindrical symmetry of the interface this does not pose a problem and it is possible to obtain all information. Again, the distribution of h_x is Gaussian. The derivative stands in direct connection to the (projected) angle θ' normal to the interface (see figure 6.1(b))

$$h_x = \tan \theta. \quad (6.12)$$

It can be shown that the distribution in one dimension of the absolute value of θ' is given by [157]

$$P[\theta'] = \frac{2}{\sqrt{2\pi\sigma'^2}} \frac{e^{-\frac{1}{2}\frac{\tan^2 \theta'}{\sigma'^2}}}{\cos^2 \theta'} \quad (6.13)$$

with $\sigma'^2 \equiv \langle \tan^2 \theta \rangle$ the variance. The special form of this equation is a result of the Jacobian of the transformation of h_x to θ using $\partial h_x(\theta)/\partial \theta = 1/\cos^2 \theta$. With the above equations we will verify if the interface can be described as a Gaussian interface.

The above equations relate to single points h at the interface. More information on the physical properties of the interface can (easier) be obtained by looking at correlation functions. The time dependent height-height correlation function is constructed as

$$g_h(x, t) = \langle [h(x', t')][h(x' + x, t' + t)] \rangle. \quad (6.14)$$

Here, $h(x) \equiv h(x, y = 0)$, t is the time and the angular brackets denote averages over primed quantities. The corresponding static correlation function, $g_h(x) \equiv g_h(x, t = 0)$,

is obtained by Fourier transforming (6.8). We can write

$$g_h(x) = \sum_{\mathbf{k}} \frac{k_B T}{\gamma L^2} \frac{1}{k^2 + L_{\parallel}^{-2}} e^{i\mathbf{k} \cdot \mathbf{s}} = \frac{k_B T}{\gamma L^2} \frac{L^2}{(2\pi)^2} \int d\mathbf{k} \frac{1}{k^2 + L_{\parallel}^{-2}} e^{i\mathbf{k} \cdot \mathbf{s}}, \quad (6.15)$$

where we have switched from a summation to an integration and $\mathbf{s} = (x, y)$. Next, we change to cylindrical coordinates and perform the integration over ϕ

$$g_h = \frac{k_B T}{\gamma} \frac{1}{(2\pi)^2} \int dk \frac{k}{k^2 + L_{\parallel}^{-2}} \int_0^{2\pi} d\phi e^{ikx \cos \phi} = \frac{k_B T}{\gamma} \frac{2\pi}{(2\pi)^2} \int dk \frac{k}{k^2 + L_{\parallel}^{-2}} J_0(kx). \quad (6.16)$$

The symbol J_0 denotes the Bessel function of the first kind. The integration over k is performed from k_{min} to k_{max} , see just below (6.10). We can directly set k_{min} to zero, since $2\pi/L \sim 0$. Setting k_{max} to ∞ allows performing the integration and (6.16) then becomes

$$g_h(x) = \frac{k_B T}{2\pi\gamma} K_0 \left(\frac{x}{L_{\parallel}} \right), \quad (6.17)$$

where K_0 is the modified Bessel function of the second kind as a function of x/L_{\parallel} . We can test the effect of setting k_{max} to infinity. We change to $\bar{k} = kL_{\parallel}$ in (6.16) and use $k_{max} = 2\pi/\sigma_c$ as a reasonable cutoff with σ_c the colloid diameter. As will be shown below L_{\parallel} is at least a couple of microns and here we will fix it at a minimal value of $1 \mu\text{m}$, whereas $\sigma_c = 142 \text{ nm}$, such that \bar{k}_{max} is at least ~ 44 . In figure 6.2(a) we plot equation (6.16) with $\bar{k}_{max} = 44$ and equation (6.17). Only at a distance $x/L_{\parallel} < 0.05$ clear differences can be observed between the two functions. Furthermore, the curve obtained with finite cut-off shows some fine structure. We thus conclude that (6.17) holds for distances x larger than a small-distance cutoff of the order of the particle size.

The dynamic correlation function at a fixed position is defined as $g_h(t) \equiv g_h(x = 0, t)$. Capillary wave theory in the overdamped regime [43,44] predicts modes with wavevector \mathbf{k} to decay according to $\exp(-t(\gamma k + g\Delta\rho/k)/2\eta)$, with the viscosity η as defined below. We are in the overdamped regime at lengths L smaller than [44]

$$L < 8\pi \frac{(\rho_L + \rho_G)}{\gamma} \left(\frac{\eta_L}{\rho_L} \right)^2 \propto L_{\eta}. \quad (6.18)$$

Here, ρ_x is the mass density and η_x the viscosity of the liquid ($x = L$) or gas ($x = G$) phase. The viscous length L_{η} is of the order of meters for colloid-polymer mixtures as shown in chapter 1. Including this in the capillary wave spectrum of (6.8) we can again perform the Fourier transformation to real space. Since we work at a fixed position $\exp(i\mathbf{k} \cdot \mathbf{s}) = 1$, we can directly write

$$g_h(t) = \frac{k_B T}{2\pi\gamma} \int_0^{\bar{k}_{max}} d\bar{k} \frac{\bar{k}}{1 + \bar{k}^2} \exp(-(\bar{k} + \bar{k}^{-1})t/2\tau), \quad (6.19)$$

where τ is given by [43, 44]

$$\tau = L_{\parallel} \frac{\eta}{\gamma} = L_{\parallel} \frac{\eta_L + \eta_G}{\gamma}. \quad (6.20)$$

Note that in the original paper [134] we erroneously omitted the factor 2 in the exponent of (6.19). Again, we can test whether or not k_{max} can be set to ∞ in the integral in (6.19). In figure 6.2(b) we make a similar plot as in (a). Clearly, only at very small times a small deviation can be expected. We now have derived the set of equations that will be used in this chapter. Of course, many extensions are possible, in particular by looking at angle correlation functions [157].

In molecular fluids γ is of the order of 10 – 100 mN/m and $\Delta\rho$ is about $10^2 - 10^3$ kg/m³. Therefore, the interface roughness $L_{\perp} \sim 0.3$ nm, whereas the correlation length $L_{\parallel} \sim 3$ mm resulting in extreme ratios of roughness-to-correlation length of 10^{-7} , only accessible through scattering techniques and a real challenge for theories describing the interface. Furthermore, it is clear that in general in molecular fluids $L \geq L_{\parallel} \gg L_{\perp} \gtrsim l_m$. Here we exploit the scaling up of lengths when going from molecules to mesoscopic colloidal particles of size 140 nm in order to directly observe capillary waves in real space.

Adding polymer to a colloidal suspension may induce a fluid-fluid demixing transition that is widely accepted to be the mesoscopic analogue of the liquid-gas phase transition in atomic substances [26]. The coexisting phases are a colloidal liquid (rich in colloid and poor in polymer) and a colloidal gas (poor in colloid and rich in polymer). The origin of the phase separation lies in the entropy-driven attraction between the colloids, which is mediated by the polymers [19, 24]. It is known from experiment [36, 37, 106] and theory [102, 103, 129], that in such systems the interfacial tension scales as $\gamma \sim k_B T / \sigma_c^2$, with σ_c the particle size, leading to ultra-low values for γ (~ 1 μ N/m and below). This, in turn, implies that using colloidal suspensions scales up the interface roughness and simultaneously scales down the correlation length. Interestingly, it also implies that $L \gg L_{\parallel} \geq L_{\perp} \gtrsim l_m$ in contrast to molecular fluids. With the current system (as detailed below) we succeed to bring both the roughness and the correlation length in the μ m-regime. In addition, the interplay between ultra-low interfacial tension and relatively large viscosity, η , sets the capillary velocity γ/η (see for example [41]) in the range of μ m/s, as opposed to typical velocities of the order of 10 m/s in molecular fluids. The associated characteristic time for the decay of interfacial fluctuations, which we refer to as the capillary time, is given by (6.20). In the case of colloids it becomes of the order of seconds. Thus, through the appropriate choice of the colloid diameter we can trace the statics *and* dynamics of the capillary waves at a free interface with optical microscopy.

6.3. EXPERIMENTAL METHODS

We used fluorescently labeled poly(methylmethacrylate) (PMMA) colloidal spheres [67] with radius $R_c = 71$ nm (obtained from static light scattering) and size polydispersity $\lesssim 10\%$. The polymer was commercially available polystyrene (Fluka) with molecular weight $M_w = 2 \cdot 10^6$ g mol $^{-1}$ ($M_w/M_n < 1.2$, where M_n is number-average molecular weight) and radius of gyration $R_g \sim 43$ nm (estimated from data in the literature [57, 68]). The underlying phase diagram is shown in figure 6.3. Details are given in chapter 2 for system 3 PPD71, section 2.3. Each measurement was done after one day of equilibration. The microscope was aligned by making use of the interface, which serves as a spirit level. We checked that the system was well equilibrated by following the recovery of intensity after bleaching a space region in the gas and/or liquid phase. The recovery appeared to be governed solely through diffusion of particles without any indications of drift (e.g. through convection). Different data sets were acquired at many different state points following several dilution lines. The data sets consisted of approximately $5.1 \cdot 10^5$ interface data points when images were scanned as fast as possible (about 5 frames per second), and about $1.5 \cdot 10^5$ when a delay time between consecutive images was used (of about 10 s) to get rid of some of the time correlation.

Pictures, such as those in figure 6.4, represent an intensity distribution of fluorescent light, $I(x, z, t)$, at a certain time t with x the horizontal (along the interface) and z the vertical (opposite to gravity) components of the space vector. The microscope records

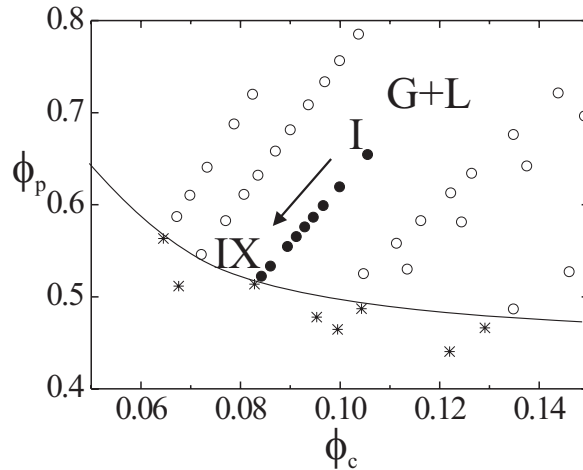


FIGURE 6.3. Experimental phase diagram of a mixture of PMMA colloids and PS polymer in decalin with $q = 0.6$, System 3 PPD71. Indicated are state points where gas-liquid phase separation occurs (open and solid circles) and state points in the one-phase region (crosses). The line is an estimate of the binodal and is drawn to guide the eye. State points to which references are made in the text are indicated (solid circles and Roman numbers).

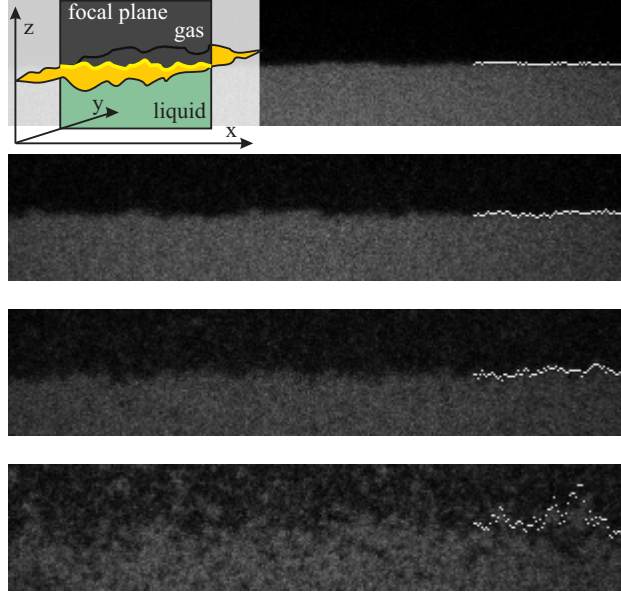


FIGURE 6.4. Capillary waves at the free liquid-gas interface in a phase-separated colloid-polymer mixture imaged with laser scanning confocal microscopy at four different statepoints approaching the critical point (from top to bottom: statepoints I, VI, VIII and IX, see figure 6.3). The focal (viewing) plane is perpendicular to the interface and only a very thin slice (of thickness $\sim 0.6 \mu\text{m}$) is imaged (see the inset). Gravity points downwards and the size of each image is $17.5 \times 85 \mu\text{m}^2$. Thermally excited capillary waves corrugate the interface and their amplitude increases upon approaching the critical point. The bright dots at the right indicate the surface location $h(x)$ obtained with our method.

the fluorescence of excited dye within the colloids, hence the colloid-rich (liquid) phase appears bright and the colloid-poor (gas) phase appears dark. $I(x, z, t)$ is a direct measure of the local and instantaneous distribution of colloidal particles and provides the starting point for a statistical analysis. Due to the finite resolution [74] we can access length scales $\sim 2R_c$, and we neglect effects induced by the finite time needed to scan each frame, and take I as an instantaneous snapshot (justified by comparing the colloid self-diffusion time with the scanning time). Thus, the real space pictures in figure 6.4 show the structure of a gas-liquid interface practically at the particle scale. We rely on the concept of a local interface between both phases. In the spirit of a Gibbs dividing surface we define an interface position $h_b(x, t)$ (now with respect to the bottom of the image, instead of the mean interface position as in section 6.2) such that in one column of vertical length L_z the total intensity can be written as

$$\int_0^{L_z} dz I(x, z, t) = I_L(x)h_b(x, t) + I_G(x)(L_z - h_b(x, t)). \quad (6.21)$$

Here, the values $I_G(x)$ and $I_L(x)$ are the average bulk intensities in the gas and liquid phase, respectively, and are taken to be functions of x to account for the microscope objective properties. In practice, integrals in the notation are sums over pixels and we have checked that the results of the subsequent analysis in correlation functions do not depend sensitively on the precise definitions of I_G and I_L . The resulting “height” function $h_b(x)$ (shown as the bright spots in figure 6.4) describes the interface position quite accurately. From top to bottom in figure 6.4 we approach the critical point and both the capillary waves and density fluctuations increase, while the density (intensity) difference between the two phases decreases.

For each frame the average interface position is $\bar{h}_b(t) \equiv \langle h_b(x', t) \rangle$. We now define a new height function that describes the deviations from the mean interface position $h(x, t) = h_b(x, t) - \bar{h}_b(t)$.

6.4. RESULTS AND DISCUSSION

The distribution of heights is shown in figure 6.5(a) for three different statepoints. The width of the distribution for statepoint I is about twice the particle diameter, the order of which is in good agreement with scaling arguments (1.2) as well as with (6.10). As one approaches the critical point the distributions get broader up to 7 times the particle diameter for statepoint VIII, but the shape remains that of a normal distribution. The next step is to look at derivatives of $h(x, t)$ [157]. In figure 6.5(b) histograms are plotted of the absolute value of θ' for three different statepoints (as in figure 6.5(a)). One can either fit the data to equation (6.13) with the variance as fitting parameter or obtain the variance directly from $\langle \tan^2 \theta \rangle$. Here, we have plotted both methods. The agreement is yet another confirmation that the interface can be described

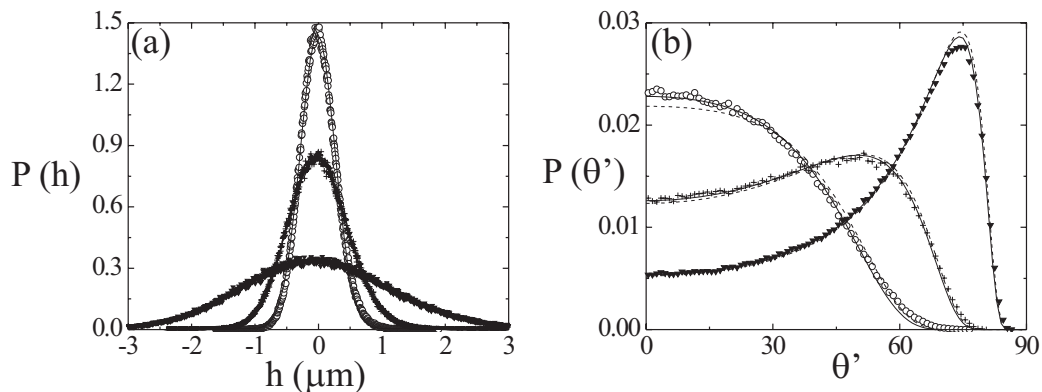


FIGURE 6.5. (a) Height and (b) angle distributions for three different state points: I (open circles), V (plusses) and VIII (triangles). In (a) full curves are Gaussian fits. In (b) we either fitted the variance in (6.13) (full curves) or obtained the variance directly from experiment (dashed curves).

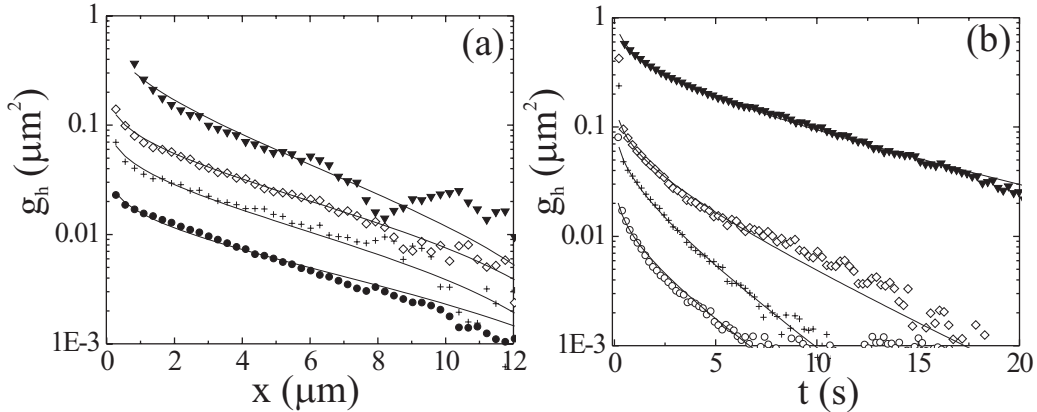


FIGURE 6.6. Correlation functions characterising the free (colloid) liquid-gas interface as obtained from quantitative analysis of LSCM pictures. (a) Static height-height correlation function $g_h(x)$ as a function of the (lateral) distance x for statepoints I, V, VI and VIII (figure 6.3) approaching the critical point. Experimental results (symbols) are compared with predictions from the capillary wave model (lines). (b) Dynamical height-height correlation function at fixed position, $g_h(t)$, as a function of time t for the same statepoints.

within a Gaussian interface model. As the critical point is approached the peak in the angle distribution shifts from 0° to 75° , since the interface roughness increases and the correlation length decreases. Since σ'^2 depends strongly on the molecular interactions, it is in principle possible to obtain the interfacial tension more accurately and to determine the microscopic cut-off, i.e. the microscopic length l_m in (6.10) [157].

However, the physical interpretation of figure 6.5 is limited due to the finite resolution of the confocal technique as well as our interface location procedure. Each height $h(x, t)$ appears to consist of the actual height plus a delta correlated “noise” term $\Delta(x, t)$ with properties such that $\langle \Delta(x', t') \rangle = 0$, and $\langle h(x', t') \Delta(x', t') \rangle = 0$ averaged over either x' or t' . Furthermore, $\langle \Delta(x', t') \Delta(x' + x, t' + t) \rangle = \sigma_\Delta^2 \delta(x) \delta(t)$ with δ the delta function. Thus, from figure 6.5 we see that the interface roughness is Gaussian, but the actual physics –although present as can be observed from the trends in the figure– is blurred by the small noise term. To cope with this we construct correlation functions. It is easy to see that such a correlation function does not suffer from the delta-correlated noise, except when both $x = 0$ and $t = 0$.

The static and dynamic correlation functions, i.e. equations (6.17) and (6.19), describe the experimental data points very well, as can be clearly seen in figure 6.6(a) and (b) for various statepoints with only two physical parameters (γ, L_\parallel in the static case and γ, τ in the dynamic case). No bending term in (6.8) was needed in the analysis. Note that in the original paper [134] the y-axis was given in units of pixels squared and not as indicated in μm^2 , but the analysis was not affected by this. Results for the

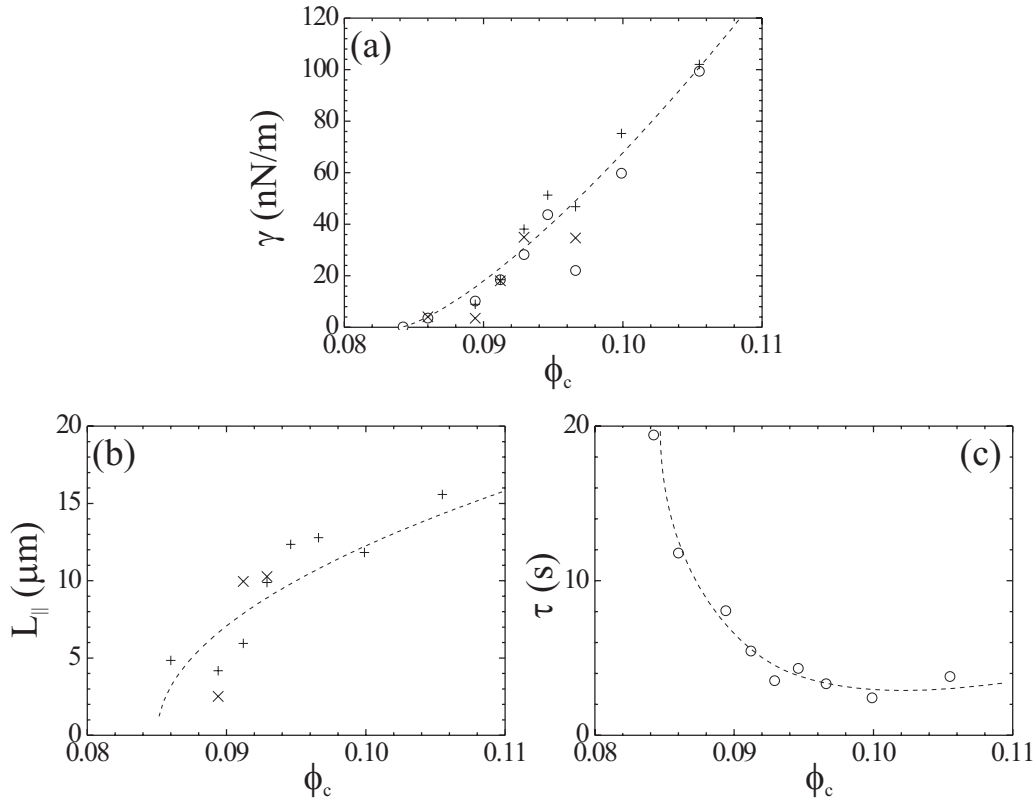


FIGURE 6.7. (a) Interfacial tension γ as a function of the overall colloid packing fraction ϕ_c obtained from $g_h(x)$ (crosses: slow frame rate, pluses: fast frame rate), and $g_h(t)$ (circles). (b) The capillary length L_{\parallel} as a function of ϕ_c obtained from $g_h(x)$. (c) The capillary time τ as a function of ϕ_c obtained from $g_h(t)$. Results stem from statepoints I-IX, see figure 6.3. The dashed lines are to guide the eye.

interfacial tension, capillary length, and capillary time are displayed in figure 6.7(a), (b) and (c), respectively. The relation of these quantities through (6.20) allows for an independent check of the consistency of our measurements. For example, for statepoint I: $\gamma = 100$ nN/m, $L_{\parallel} = 15$ μm and $\eta_L + \eta_G = (30 + 12.6)$ mPas, leading via (6.20) to a capillary time of 6 s. From the dynamical correlation function we find $\tau = 4$ s. Note that, in contrast to [134], τ as given in equations (6.19) and (6.20) and plotted in figure 6.7(c) should be the reference quantity. This differs from the time used in [134] by a factor of 2. Still the agreement with the independent check remains satisfactory.

6.5. CONCLUSIONS

Using a colloid-polymer mixture allows to carefully tune the interface properties and as a result the thermal capillary waves at a free interface are observed visually by means of LSCM. From the fluorescence intensity difference the interface can easily be located

and the height functions are constructed. By analysing the height fluctuations as well as the derivatives of these we see that the interface roughness can be described within a Gaussian model. To deal with small noisy contributions to the height function space and time correlation functions are determined. The quality of the fits in describing the correlation functions and the internal agreement validate the capillary wave model practically down to the particle level. The present work opens up a wide range of possibilities, e.g. to study temperature gradients and mass transport across the interface at a scale of the thermal roughness, to explore the effects of thermal capillary waves on droplet coalescence (chapter 7) and snap-off (chapter 8), on heterogeneous catalysis, on wetting behaviour, to study the freezing of capillary waves at the gel-line, etc.

For example, one of the interesting consequences for wetting behaviour is that in most molecular situations the system size L is larger than or comparable to the correlation length of the capillary waves L_{\parallel} . This length is much larger than a reasonable wetting layer thickness l_w , which in turn is larger than the thermal roughness L_{\perp} . Thus we find $L \gtrsim L_{\parallel} \gg l_w > L_{\perp}$, whereas in colloid-polymer mixtures we would expect $L \gg L_{\parallel} > l_w \gtrsim L_{\perp}$.

Another possibly interesting route would be to study even larger colloids to do the analysis really at the particle level. Recently, we have exploited a mixture of large PMMA particles of diameter 400 nm and poly(styrene) polymer with a radius of gyration of 200 nm ($M_w = 23 \cdot 10^6$ g/mol). Here we do see the particles in the capillary waves separately, figure 6.8. Unfortunately, gravity spoils the phase behaviour and the systems ends up in a gas-solid equilibrium, a problem that in principle can be solved by density matching the colloids.

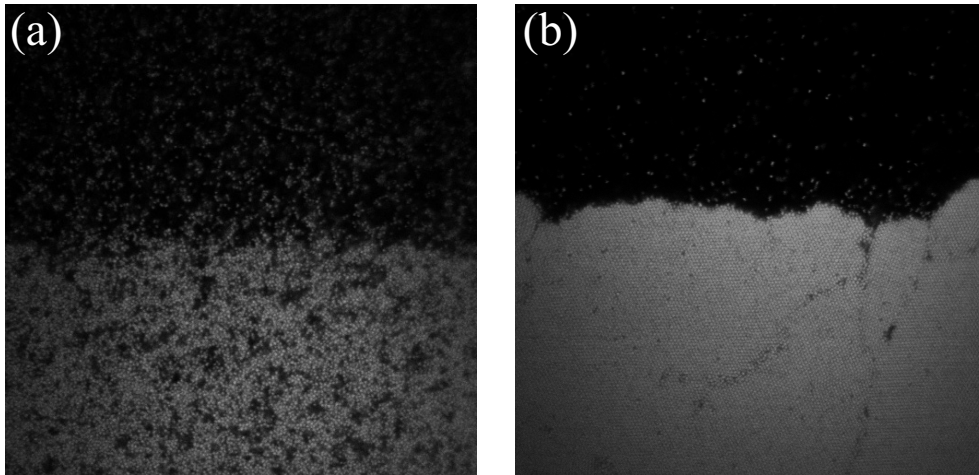


FIGURE 6.8. LSCM images ($60 \times 60 \mu\text{m}^2$) of a gas-liquid interface (a) and of a gas-crystal interface (b). The individual particles can be clearly observed. The left interface is dynamically rough, whereas in the right interface the first crystal layer appears to be fluid-like.

7

Hydrodynamics of droplet coalescence

ABSTRACT

We study the coalescence of a drop with its bulk phase in fluid-fluid demixing colloid-polymer mixtures. The process takes places in three consecutive stages: (i) drainage of the continuous film between droplet and bulk phase, (ii) breakup of the film, and (iii) the growth of the connection. The first stage is compared with existing theories on drainage, where we show several limiting cases. We observe that drainage becomes very slow and eventually the breakup of the film is induced by thermal capillary waves. The waiting time for a certain height fluctuation, which turns out to be an important parameter for the kinetics of the process, can be directly obtained from experiment. Van der Waals forces need not be invoked. During the third stage we observe that the radius of the connecting neck grows linearly with time both for gas bubbles and liquid droplets with an order of magnitude that is in good agreement with the capillary velocity.

7.1. INTRODUCTION

The process of droplet coalescence is frequently observed in every day life. Whenever two miscible liquid drops or a liquid drop and its liquid bulk come into contact they may coalesce. This has important consequences, e.g. the droplet size distribution in rain is (among other processes) determined by the coalescence probability [158]. The coalescence reduces the total interface area and is driven by interfacial tension. The phenomenon has been studied since the 19th century [159] and it is a classical example of a free surface problem in fluid dynamics. It is of practical importance as well; in many industrial applications –such as printing and sintering processes– coalescence plays a crucial role (to be either avoided or induced). Recent developments in the

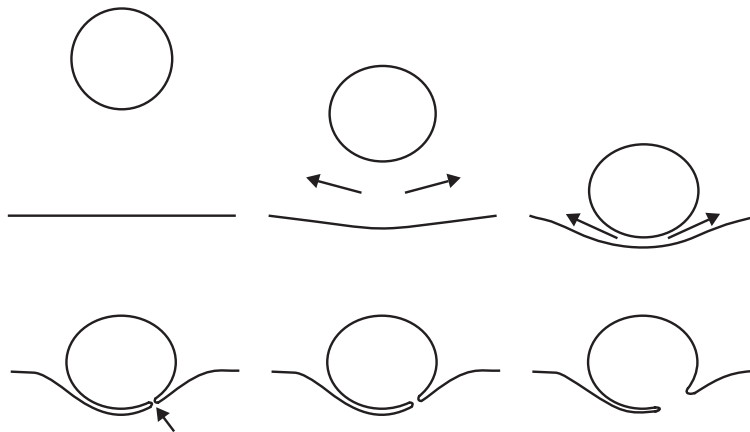


FIGURE 7.1. Schematic drawing of the consecutive stages of droplet coalescence from left to right, top to bottom. Shown is the drainage of the continuous phase (i) (top row), the first connection is made (ii) and the radius of the neck grows in time (iii) (bottom row).

field of microfluidics [160], in which fluids are manipulated on a microscopic level and miniature chemical reactions can be carried out on a chip, raise a further need to study this phenomenon.

In the present chapter we will focus on the consecutive stages of droplet coalescence. We make use of the properties of colloid-polymer mixtures to be able to follow the details of coalescence in time with microscopy. Phase separated colloid-polymer mixtures are well known to display behaviour analogous to molecular fluid-fluid systems. The origin of the phase separation in colloid-polymer mixtures lies in the entropy-driven attraction between the colloids, which is mediated by the polymers [19,24]. The coexisting phases are a colloidal liquid (rich in colloid and poor in polymer) and a colloidal gas (poor in colloid and rich in polymer). After preparing a sample in the two-phase region individual droplets of either the liquid or the gas coalesce with their bulk phases at the final stages of phase separation. This allows to study this process, which consists of three stages: (i) film drainage of the continuous phase between the droplet and the free interface, (ii) rupture of the film, and (iii) extrusion of the droplet material into its bulk phase, see figure 7.1 for a schematic drawing of these steps.

The first stage (i) has been studied for quite some time [161–165], although it theoretically still poses some difficulties [166]. In many studies the drainage is followed close to the point of film rupture (ii) and step (ii) in relation with step (i) is studied [161,167] and the role of van der Waals forces is investigated [155,168]. Recently, significant theoretical [169] and numerical [170] progress has been made in the description of the neck growth, step (iii), and in understanding the singularity that occurs during coalescence. Very recently, experiments have observed the initial viscous coalescence [171], as well as the inertial coalescence [172,173], which follows the viscous coalescence.

The big advantage of using colloid-polymer mixtures over molecular fluids finds its origin in the ultralow interfacial tension of demixed colloid-polymer mixtures. The typical magnitude of the interfacial tension γ is proportional to [3, 12]

$$\gamma \sim \frac{k_B T}{d^2} \quad (7.1)$$

with $k_B T$ the thermal energy and d the typical length scale at the interface, similar to the particle diameter σ_c far away from the critical point. This order of magnitude has been confirmed in experiment [35–38, 106, 134], theory [102, 103, 120, 129, 130] and recently in computer simulations [135, 136]. As a result the thermal roughness of the interface $L_T = \sqrt{k_B T / \gamma}$ can become of the order of (sub)microns and it is therefore possible to study step (ii) on the scale of capillary fluctuations. Furthermore, from the Reynolds number $Re = \rho u L / \eta$ with ρ the mass density, u the velocity, L the characteristic length and η the viscosity, we can estimate at what length inertia becomes as important as viscous dissipation (see chapter 9 for a more elaborate derivation). At small length- and timescales the velocity u of interface motion is always proportional to $u \sim \gamma / \eta$. At $Re = 1$ inertial terms become important, thus at lengths

$$L_\eta = \frac{\eta^2}{\rho \gamma}, \quad (7.2)$$

and times

$$t_\eta = \frac{L}{u} = \frac{\eta^3}{\rho \gamma^2}. \quad (7.3)$$

For ordinary water with $\gamma = 73$ mN/m, $\eta = 1$ mPas, and $\rho = 1$ g/ml, inertial terms come into play at $L_\eta = 10^{-8}$ m, which is reached in $t_\eta = 2 \cdot 10^{-10}$ s, an intractably short time and length. Thus, the initial viscous regime of step (iii) is hard to observe in the laboratory for ordinary molecular liquids. To tackle this problem it is in principle possible to follow two routes: either increase the viscosity or decrease the interfacial tension. Here, we follow the latter option and decrease the interfacial tension between a factor 10^5 and 10^8 as compared to the interfacial tension of water.

We show results for several colloid-polymer mixtures, systems 1 SPC13, 2 PPD25 and 3 PPD71, described in detail in chapter 2, where also the statepoints are indicated. These yield similar results, which points at generic behaviour. The consecutive steps are described in section 7.2 for step (i), section 7.3 for step (ii) and section 7.4 for step (iii). Conclusions are drawn in section 7.5.

7.2. FILM DRAINAGE

In the first stage of droplet coalescence the drop approaches the bulk phase, see figure 7.2. Here, we show results for system 1 SPC13 (top row), which is a colloid-polymer mixture of silica colloids and poly(dimethylsiloxane) polymer in cyclohexane, and for

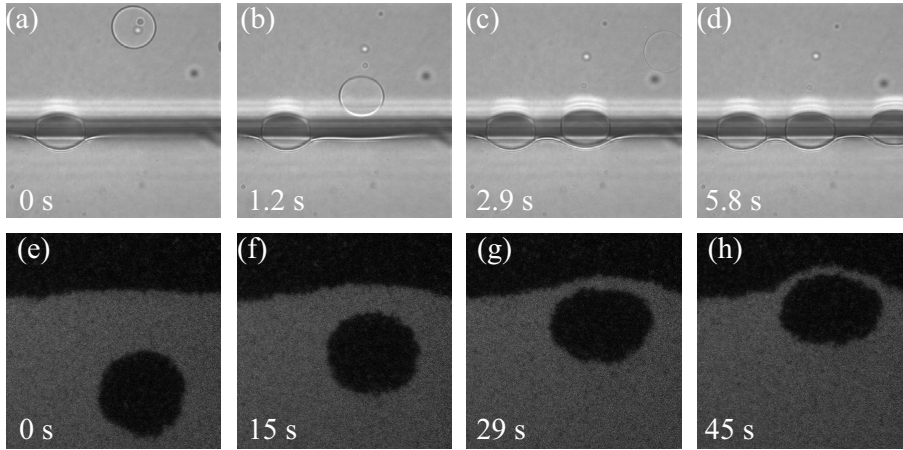


FIGURE 7.2. Step (i) in droplet coalescence in system 1 SPC13 statepoint III (a-d) and system 3 PPD71 statepoint VII (e-h) (chapter 2) as observed with transmission light microscopy (top row) and laser scanning confocal microscopy (LSCM) (bottom row). (a-d) The image size is $264 \times 264 \mu\text{m}^2$ and $R_d = 26 \mu\text{m}$. As time proceeds the shape of the drop as well as the bottom interface get distorted (b). The thin film drains very slowly (c, d) and only after about 14.5 s from panel (a) the drop coalesces. (e-h) The image size is $48 \times 48 \mu\text{m}^2$ and $R_d = 10 \mu\text{m}$. The gas bubble displays similar behaviour as the liquid drop.

system 3 PPD71 (bottom row), which contains large PMMA colloids and poly(styrene) polymer in decalin. Initially, both the drop and the interface of the bulk phase (this interface is hereafter referred to as the surface) are undistorted, figure 7.2(a) and (e). In the vicinity of the surface, however, the droplet slows down and both the drop and the surface are distorted, see figure 7.2(b) and (f). At longer times (c-d, g-h) the deformations become more pronounced, the film drains very slowly until the film ruptures.

Far away from the bulk phase a droplet of radius R_d sediments or rises at constant velocity u_s . It will not be deformed if the capillary number Ca

$$Ca = \frac{\eta u_s}{\gamma}, \quad (7.4)$$

remains smaller than unity [174]. The sedimentation velocity u_s is proportional to $g\Delta\rho R_d^2/\eta$ and we thus obtain from the capillary number the Bond number Bo [174]

$$Bo = \frac{g\Delta\rho R_d^2}{\gamma}, \quad (7.5)$$

with g earth's acceleration and $\Delta\rho$ the buoyancy. Thus, we do not expect deformations if $Bo < 1$, i.e. $R_d < L_c$, the capillary length. Indeed, in experiment most droplets remain spherical while sedimenting¹, in fact even drops with R_d slightly larger than L_c (figure 7.2(a) and (e)). A more precise treatment of the sedimentation velocity of a

¹We here use “sedimenting” as a general term, which also applies for rising gas bubbles.

viscous sphere surrounded by a viscous medium leads to (see e.g. [40])

$$u_s = \frac{2g\Delta\rho R_d^2}{3} \frac{\eta_o + \eta_i}{2\eta_o + 3\eta_i}. \quad (7.6)$$

Here, η_o is the viscosity outside the drop and η_i is the viscosity inside the drop. If $\eta_i \gg \eta_o$ the well-known Stokes friction for a hard sphere is obtained: $f = F/u_s = 6\pi\eta_o R_d$ with F the force acting on the sphere. If $\eta_i = 0$ we obtain the friction for an air bubble: $f = 4\pi\eta_o R_d$.

For a solid sphere approaching a solid or free non-deformable surface exact treatments are given in [175], which describe both the undistorted fall of (7.6) and the velocity close to the surface. The friction factor can be written as $f = 6\pi\eta_o R_d \lambda$ with $\lambda(h/R)$ the correction to the Stokes friction. In the asymptotic limit of $h = 0$, where h is the minimal distance between sphere and surface, it becomes

$$\lambda = \frac{R_d}{h} \quad \text{and} \quad \lambda = \frac{1}{4} \frac{R_d}{h} \quad (7.7)$$

for a solid surface and for a planar free surface, respectively. These limiting equations can be found from lubrication equations as well [176, 177]. Note that the factor 4 difference between a solid and a fluid interface is often observed in these types of problems. For a solid sphere approaching a deformable surface Hartland has derived expressions from lubrication theory valid for small sphere-surface separations [178]. He finds that $h \propto t^{-1/2}$. These results have later been confirmed by Jones and Wilson [166].

However, in the experiment both the fluid drop and the fluid interface become distorted at a certain separation (figure 7.2), which is approximately the drop diameter. Furthermore, fluid circulates in the drop since it has a finite viscosity, which tends to speed up drainage as compared to a solid sphere, and there is some constriction in the film thickness at its periphery, which slows down drainage. These last two effects are properly treated by Jones and Wilson [166], who point out that these effects are not captured in simple lubrication theories. They predict several asymptotic regimes, which have been confirmed by Yantsios and Davis [179] using extended lubrication theories. No full analytical treatment can be obtained and the main problem in comparison with the present experimental data is that the asymptotic limits become valid for very small separations [179].

In figure 7.3 we show the minimal drop-surface separation h as a function of time t . The time $t = 0$ is defined at $h = \sigma_d$, i.e. $t(h = \sigma_d) = 0$. The event for a liquid drop in system 1 SPC13 is plotted, which corresponds to figure 7.2(a-d). The top curve (plusses) is the minimal distance between drop and surface, the middle curve (open circles) is the distance between drop and (initially) undisturbed surface and the bottom curve (open squares) is the position of the surface with respect to its undisturbed position, see also the inset of figure 7.3(a). In figure 7.3(b) a similar event is plotted, but in this case for a gas bubble (open symbols and plusses) and for a liquid drop (filled circles) in system

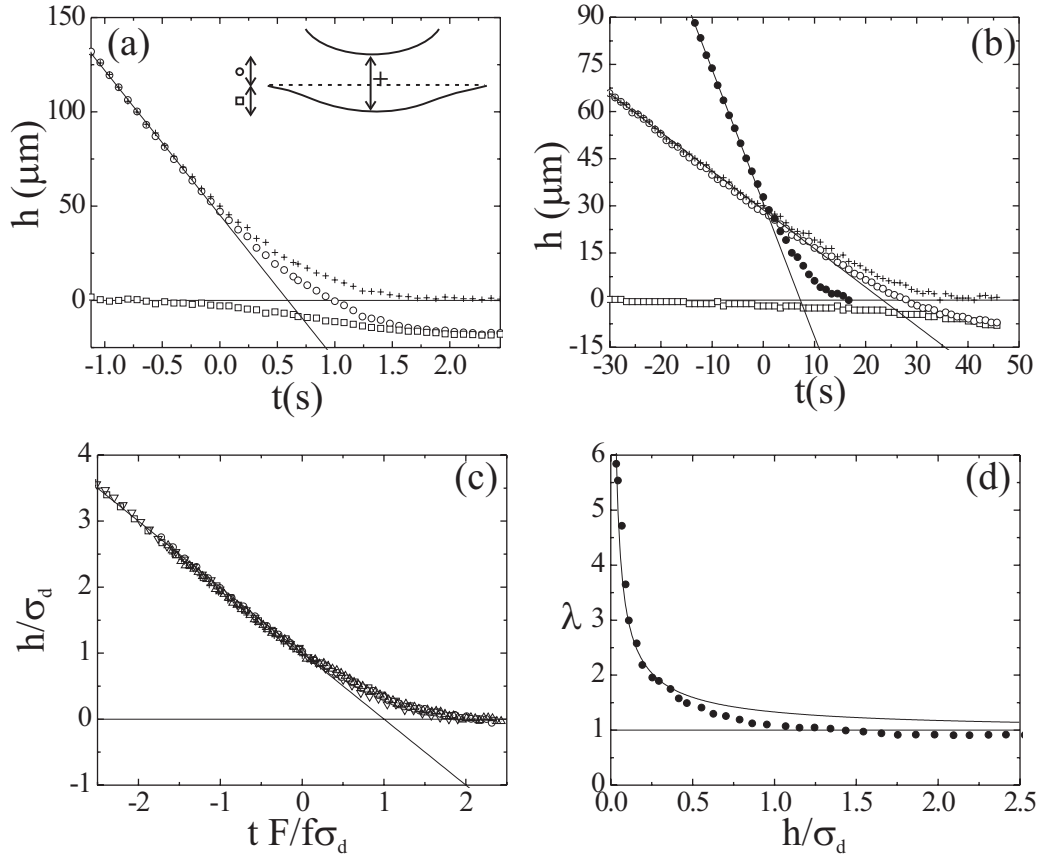


FIGURE 7.3. Interface positions as a function of time for drops in system 1 SPC13, statepoint III (a) and 2 PPD25, statepoint I (b) (chapter 2). (a) The event for a liquid drop with $R_d = 26 \mu\text{m}$. The inset explains what the symbols denote, see also the explanation in the text. (b) The event for a gas drop with $R_d = 15 \mu\text{m}$ (symbols as in (a)) and for a liquid drop with $R_d = 16 \mu\text{m}$ (for clarity, only filled circles as the circles in (a)). (c) Minimal separation (from the plusses in (a,b)) in terms of σ_d as a function of reduced time. Data of systems 1,2 and 3 collapse (six different data sets are shown). (d) The correction to the Stokes friction factor as a function of h/σ_d . At distances $h < \sigma_d$ the friction increases rapidly. The full curve comes from theory for a solid sphere sedimenting to a free non-deformable surface [175], which reaches the asymptotic value of (7.7). The full curves in (a-c) are linear fits to the first few data points.

2 PPD25, which is a mixture of small PMMA colloids and poly(styrene) polymer in decalin, see chapter 2. The difference in timescales between (a) and (b) is considerable and stems mainly from the difference in gas-liquid density contrast, which is much larger in system 1 SPC13, figure 7.3(a). In (b) the difference between gas and liquid is a result of the difference in gas and liquid viscosity, where the liquid viscosity η_L is

larger than the gas viscosity η_G . However, the shapes of the curves are very similar. In all cases the displacement is initially linear with time. For the events plotted in (b) the viscosities and density difference have been measured precisely, see table 2.1, and the initial linear velocities of the rising gas bubble and falling liquid droplet are in good agreement with equation (7.6). For example, we find for the liquid drop $4.3 \mu\text{m/s}$ from experiment and $4.2 \mu\text{m/s}$ from (7.6), for the gas bubble this is $1.2 \mu\text{m/s}$ and $1.1 \mu\text{m/s}$.

In figure 7.3(c) several data sets for liquid drops are rescaled by plotting h/σ_d vs. $t \times F/f\sigma_d$, with f following from (7.6). Thus, the initial slopes are scaled by taking the density difference as well as the inner and outer viscosity into account. We then clearly observe that data from systems 1, 2, and 3, and for different drop diameters ranging from 13 to $52 \mu\text{m}$ fall right on top of a mastercurve. Data of gas bubbles fall on a similar, but slightly different mastercurve as well. The agreement with the mastercurve for $t > 0$ is somewhat remarkable, since the distortions are considerable and surface tension is expected to play a role here as well through the Bond number [166]. The difference in the surface tension is easily one order of magnitude. This scaling implies that the problem only depends on h/σ_d .

In figure 7.3(d) we plot the Stokes' correction λ as a function of h/σ_d . The data are obtained by averaging and then differentiating the curves for liquid drops of system 2 PPD25. Here, we took the minimal drop-surface separation curves corresponding to the plusses in the inset of figure 7.3(a). Far away from the surface λ is a constant with value 0.93 in agreement with (7.6), just below the Stokes value of 1 for a hard freely sedimenting sphere. Considerable differences start occurring for $h/\sigma_d = 1$ and below. For such times $t > 0$ the friction increases due to solvent backflow and drop and surface deform. The increase in friction is in reasonable agreement with predictions for a solid sphere approaching a non-deformable surface [175]. This is of course somewhat remarkable since the problem tackled in [175] is a related, but different one. Although many approximate and asymptotic solutions have been found in literature (see for example the review of Stone [174] and references therein), it is difficult to use these on our data since it is unclear when exactly the solutions may be applied.

At very small h the velocities become very low. Here, the shape of the drop depends on the interfacial tension and the density difference alone [162, 180]. This exterior problem can be solved within a quasi static treatment and the shape (figure 7.4) is set by

$$\frac{\gamma}{g\Delta\rho} \equiv L_c^2 = \frac{l-z}{2(\frac{2}{a} - \frac{1}{b})}. \quad (7.8)$$

Here, $1/b$ and $1/a$ are the curvatures at and opposite to the apex. This relation can be derived by considering the pressure balance, $P_A = P_B$ and $P_C = P_D$, since points in

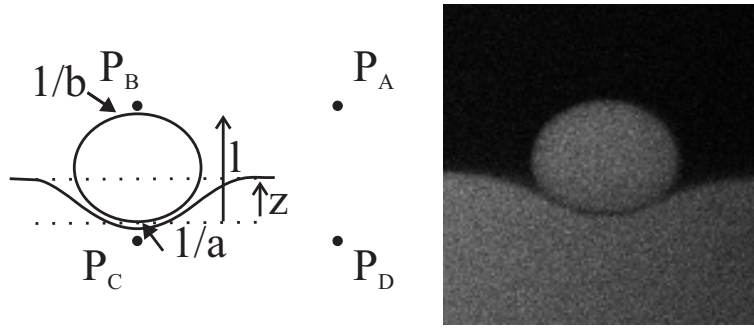


FIGURE 7.4. Explanation of the notation used in the derivation of (7.8) and an example of a liquid drop with $R_d = 19 \mu\text{m}$, $a = 28 \mu\text{m}$, $b = 24 \mu\text{m}$ and $l - z = 20 \mu\text{m}$ (system 2 PPD25, statepoint I) from which the capillary length can be obtained.

the same phase at the same height are in mechanical equilibrium. We learn that

$$P_B = P_C - \rho_L l g + \frac{4\gamma}{a} - \frac{2\gamma}{b}, \quad (7.9)$$

and

$$P_A = P_D - \rho_L z g - \rho_G (l - z) g, \quad (7.10)$$

from which (7.8) readily follows. From these simple geometric quantities the capillary length can be obtained. For example, from the shape of the droplet shown in figure 7.4 (system 2, statepoint I) the capillary length is $18 \mu\text{m}$ to be compared with $17.6 \mu\text{m}$ found by analysing the interfacial profile close to a vertical hard wall, see chapter 5.

7.3. FILM BREAKUP

The role of thermal capillary waves in the second stage of droplet coalescence has long been a topic of speculation [155, 156]. The actual breakup of the film between drop and bulk phase (step (ii)) is elusive in molecular fluids; here it is evident that capillary waves induce the spontaneous breakup, which occurs when two opposite bulges at the two interfaces meet (not necessarily symmetrically), see figure 7.5. The probability for such an event depends on the interface roughness and on the interface correlation length and time. The question is what time we have to wait for a height fluctuation $h \geq h^*$ to occur on a certain surface area.

From experiment it is possible to obtain the waiting times as a function of the observed length L , where we have followed ideas from Smoluchowski [181] and Becker [182]. After locating the interface position as described in chapter 6, we construct a space-time plot in the following manner; if $h(x, t) > h^*$ the value is 1 (white), otherwise it remains 0 (black), see figure 7.6(a) for an example of statepoint V of system 3 PPD71 with $h^* = 0.41 \mu\text{m}$. Next, we divide the system along x in a number of patches with length L . If at any point in this patch a white pixel is found the complete patch turns white,

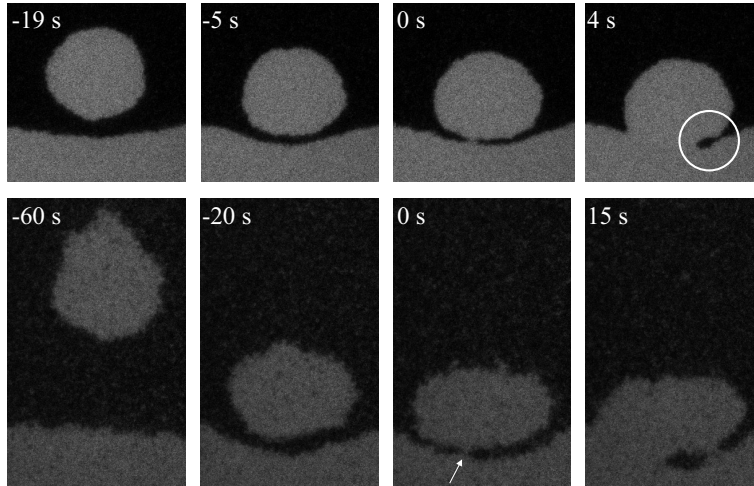


FIGURE 7.5. Coalescence of colloidal liquid droplets with the bulk liquid phase in system 3 PPD71. Top row, coalescence of a droplet of diameter $16.5 \mu\text{m}$ for state point I (far away from the critical point); bottom row, coalescence of a droplet of diameter $21.8 \mu\text{m}$ for state point VIII (close to the critical point). The three consecutive steps of the coalescence event can be followed in time (as indicated, where $t=0$ now corresponds to the instant of film breakup). Clearly, the capillary waves at both interfaces induce the breakup of the confined gas layer. The white circle marks the typical shape as predicted by Eggers *et al.* [169]. In the series in the bottom row, the arrow denotes the place of film breakup. In this case, a second connection is made and the gas phase is being trapped in the liquid phase.

which means that at that time in that patch a fluctuation of at least the predefined height has occurred. This leads to images as in figure 7.6(b), which is for the same statepoint as in (a), but now with $h^* = 0.82 \mu\text{m}$. In this case we took $L = 17.5 \mu\text{m}$. We now identify the waiting time $\theta(h^*)$ as the average time the patches are 0. We can thus write

$$\theta(h^*) = \frac{M\Delta t}{k}, \quad (7.11)$$

where M is the total number of empty patches, Δt the time between subsequent patches and k the number of jumps from 0 to 1. In constructing the waiting times it was found that these are very sensitive to noise. To cope with this we have averaged over 1000 frames. Furthermore, along the x coordinate we span $140 \mu\text{m}$, but only the inner $105 \mu\text{m}$ is used, which is slightly less noisy. In figure 7.6(c) we have plotted the waiting times as a function of h^* for three different statepoints approaching the critical point, from left to right statepoints I, V, and VII (see chapter 2, figure 2.3(b)). Clearly, the waiting times rise steeply as a function of h^* . Analysing fluctuations smaller than a certain h^* leads to a symmetric situation as shown by the open symbols in figure 7.6(c). In

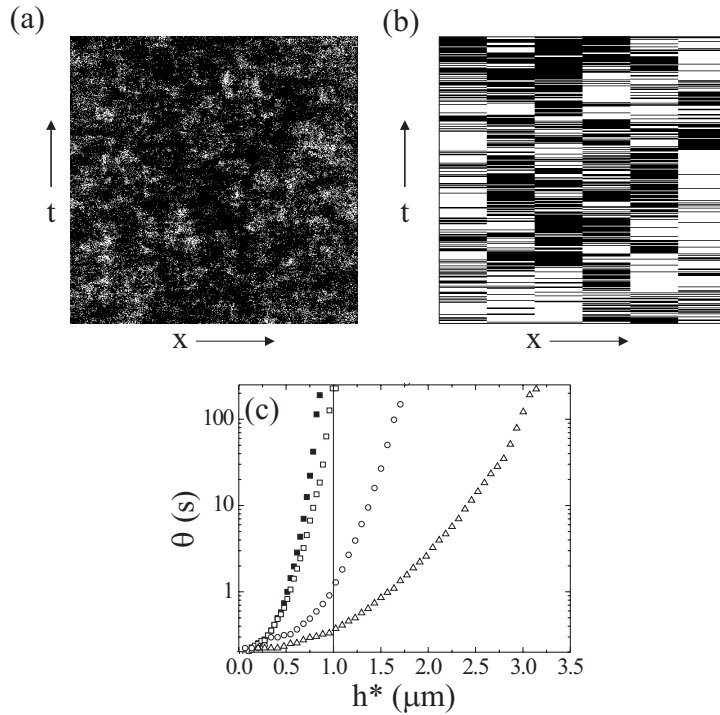


FIGURE 7.6. (a) Space-time plot for statepoint V, system 3 PPD71, with $h^* = 0.41 \mu\text{m}$. The x spans $140 \mu\text{m}$ and t spans 112 s (of the maximum of 223 s). In (b) a space-time plot is shown for the same statepoint as in (a), but for $h^* = 0.82 \mu\text{m}$. Here, x spans $105 \mu\text{m}$ and t spans 86 s . The patches have a length L of $17.5 \mu\text{m}$. In (c) the data points are for $L=17.5 \mu\text{m}$ and for three different statepoints: I (squares), V (circles) and VII (triangles) approaching the critical point. The filled squares are for a mirror event of the open squares with negative excursions and plotted against $|h^*|$. The vertical line indicates $h^* = 1 \mu\text{m}$.

chapter 6 it was already shown that the height distributions are symmetrical (Gaussian) distributions.

In the experiment it is observed that the connection in droplet coalescence is typically made at film thicknesses of $\sim 1 \mu\text{m}$ for samples reasonably close to the critical point. As can be seen from the waiting times in figure 7.6(c) such a fluctuation typically occurs in a couple of seconds. Since the droplet “sees” a certain area, the connection at such thicknesses does not seem unreasonable. For samples away from the critical point the roughness is less pronounced and the film rupture indeed occurs at smaller separations. In general we observe that at a certain droplet-surface separation, drainage becomes so slow that a spontaneous connection mediated by the capillary waves is more likely to occur. Since at these lengthscales and in these organic mixtures van der Waals forces are minimal we do not need to invoke such forces to explain the coalescence, more precisely the first connection. This is still an open debate in molecular fluids [183],

although very recently experiments indicate that in molecular fluids the connection is brought about solely by van der Waals forces [168].

7.4. NECK GROWTH

At the connection a liquid bridge is formed and the radius of the neck increases in time, see figure 7.7. The opening speed of the bridge results from a competition between the capillary forces driving the coalescence, and the viscous forces slowing it down. Equating these two forces (i.e. setting the capillary number to unity in (7.4)) leads to a time dependence of the radius of the neck R_n as [169]

$$R_n(t) \propto \frac{\gamma}{\eta_i} t. \quad (7.12)$$

This coalescence mechanism leads to very large speeds in ordinary molecular fluids: for water the capillary velocity is about 70 m/s. The full theory predicts only logarithmic corrections to this. Eggers *et al.* [169, 170] find

$$R_n(t) = -\frac{\gamma}{\pi\eta_i} t \ln\left(\frac{\gamma}{\eta_i R_d} t\right), \quad (7.13)$$

for a viscous drop in inviscid surroundings. The shape of this solution remains the same when the viscosity of the surrounding phase is incorporated in the problem.

At longer times it is either the viscous or the inertial forces that slow down the coalescence. This depends on the relative importance of these two forces and can be

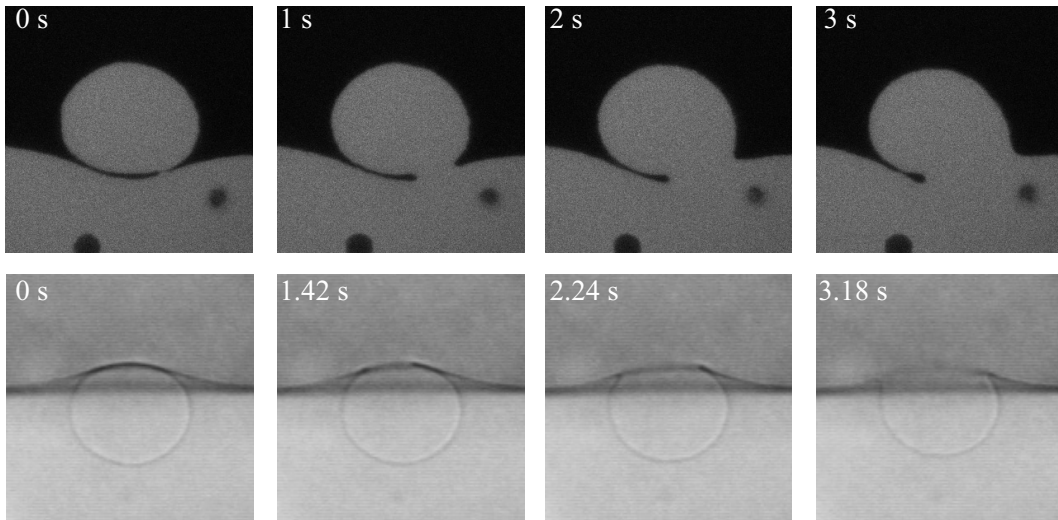


FIGURE 7.7. Neck growth in coalescence (system 2 PPD25, statepoint I) for a liquid drop with $R_d = 15 \mu\text{m}$ (top row, image size $59 \times 59 \mu\text{m}^2$, LSCM) and a gas bubble of $R_d = 16 \mu\text{m}$ (bottom row, image size $69 \times 69 \mu\text{m}^2$, transmission light microscopy). The gas bubble breaks more symmetrically in comparison with the liquid drop. The typical retracting shape in the top row can again be observed [169], see also figure 7.5.

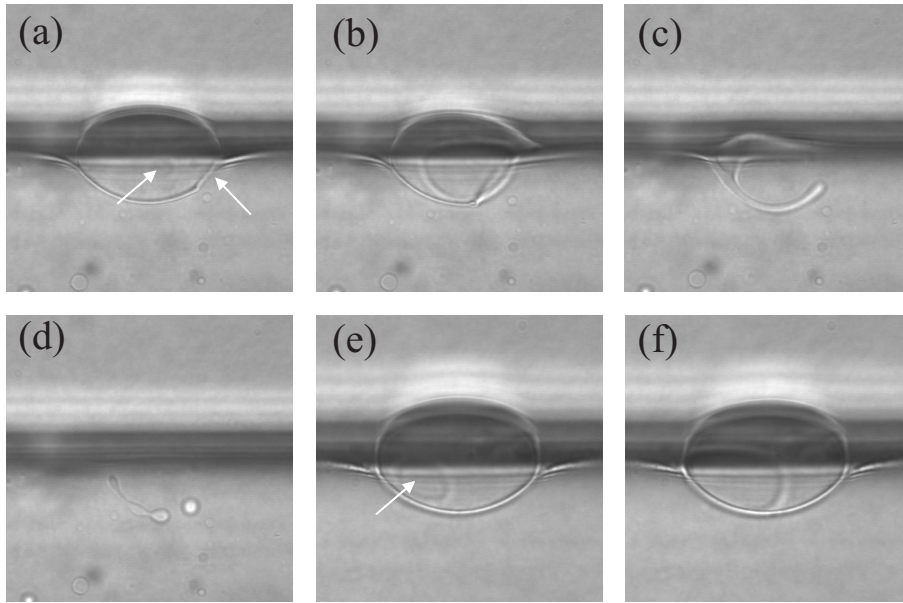


FIGURE 7.8. In (a-d) two connections are made and gas phase is left behind. The instabilities on the gas cylinder can be clearly observed (c,d). The image size is $128 \times 128 \mu\text{m}^2$. The total time span is 2.6 s. (e,f) Assymetry in growth after a first connection at the periphery of the draining film. The image size is $128 \times 128 \mu\text{m}^2$ and the time difference is 0.26 s. The white arrows point at connections. System 1 SPC13, statepoint III.

found from the Reynolds number Re , as explained in the introduction of this chapter (section 7.1). If inertia is dominant, i.e. $Re > 1$, the radius increases as [169,170]

$$R_n(t) \propto \left(\frac{\gamma R}{\rho} \right)^{1/4} \sqrt{t}. \quad (7.14)$$

But in colloid-polymer mixtures this occurs at lengths L_η and times t_η , on the order of meters and hours due to the ultra-low interfacial tension. It is therefore very unlikely that this square root regime will be reached. To the contrary, the first –linear– regime of viscous coalescence is very hard to observe for molecular fluids, since the initial velocities are huge (70 m/s) and only by increasing the viscosity drastically and using ultrafast cameras the initial regime is now observed in molecular fluids as well [171,184]. Here, however, we explore the option of using a system with an ultralow interfacial tension [184].

In figure 7.7 we show a coalescing liquid drop captured with LSCM (top row) and a coalescing gas bubble captured with transmission light microscopy (bottom row) for system 2 PPD25. Although the contrast with LSCM is much better than with light microscopy the coalescence is too fast to be followed with LSCM in great detail. In principle, this could be solved by using system 3 PPD71, which has even slower dynamics, but in this system first connections are often made at several points at more

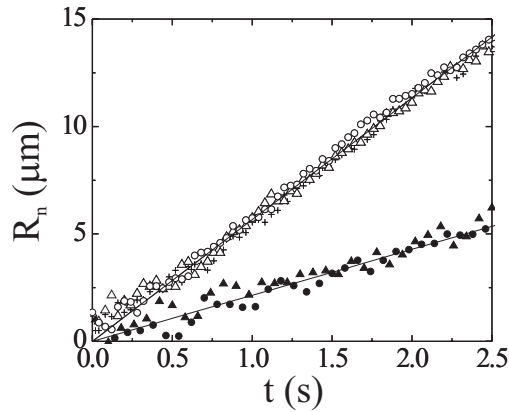


FIGURE 7.9. Radius of the neck R_n as a function of time for gas bubbles (open symbols; three different events with $R_d = 16, 17$ and $18 \mu\text{m}$) and liquid droplets (closed symbols; two different events with $R_d = 15$ and $17 \mu\text{m}$). The full curves are linear fits to the data. The linear behaviour can be observed up to several times $\eta_i R_d / \gamma$ in contrast to experiments with molecular fluids [171,184]. System 2 PPD25, statepoint I.

or less the same time, which makes the determination of the opening speed somewhat difficult. Furthermore, in that case an instability may occur and a droplet of the film phase is trapped in the bulk phase, as shown here for system 1 in figure 7.8 (a-d), in line with predictions by Eggers *et al.* [169]. In addition, with LSCM it is difficult to determine if the growth is in or out of the field of focus. Finally, we observe that the coalescence can occur anywhere in the contacting drop bulk area. For gas droplets the first connection is often made in the top of the gas droplet, which leads to a symmetric breakup. For liquid drops the first connection is made anywhere at this area, but more often at the periphery in line with the predictions of Jones and Wilson [166] about the precise shape during drainage, who show that at the periphery the drop-surface separation is minimal. The difference between gas and liquid drops points to subtle differences in the shape of the drop and surface during drainage (step (i)). If the first connection is not on the central symmetry axis this may lead to an asymmetric neck growth after a certain time, see figure 7.8(e) and (f). Here, we explore system 2 PPD25 with light microscopy.

Figure 7.9 shows the radius of the neck R_n as a function of time. The top data correspond to coalescing gas bubbles, the bottom data to coalescing liquid droplets. Clearly, a linear dependence is observed with no signs of a logarithmic correction, possibly since the logarithmic regime only occurs at very small times after coalescence [169]. The slope of the lines are $5.7 \mu\text{m/s}$ for the gas bubbles and $2.1 \mu\text{m/s}$ for the liquid droplets. For this statepoint the interfacial tension has been accurately determined by measuring the density difference and then the capillary length in several ways: by

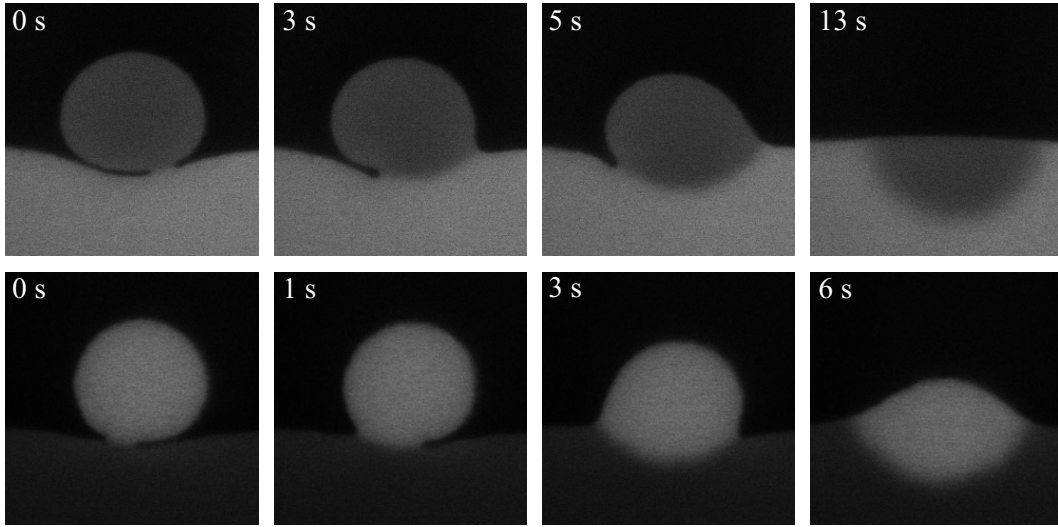


FIGURE 7.10. By bleaching either the droplet (top row, $56 \times 56 \mu\text{m}^2$) or the bulk liquid phase (bottom row, $41 \times 41 \mu\text{m}^2$) the coalescence event can be followed in great detail. The drop forms a hemisphere in the bulk phase and spreads by diffusion. System 2 PPD25, statepoint I.

analyzing the shape of a drop resting at the interface (see (7.8)) and the shape of the interfacial profile close to a wall (chapter 5). From these methods the interfacial tension is found to be $0.16 \mu\text{N/m}$. The viscosities of liquid and gas phases were measured with an Anton Paar Physica MCR300 rheometer and we found $\eta_L = 31 \text{ mPas}$ and $\eta_G = 8 \text{ mPas}$. Applying the scaling relation (7.12) we expect coalescing velocities of the order of $20 \mu\text{m/s}$ for the gas bubble and $5.2 \mu\text{m/s}$ for the liquid drop without taking the viscosity of the outer fluid into account. Thus, for this statepoint the prefactor in equation (7.12) is around 0.3 for gas droplet coalescence and around 0.4 for liquid droplet coalescence. Hence, the gas bubble is slowed down more by its relatively viscous surroundings than the liquid droplet. Clearly, the observed velocities are set by the capillary velocity. However, making a quantitative prediction for the viscosity ratios such as the one in the current experiment remains a theoretical challenge.

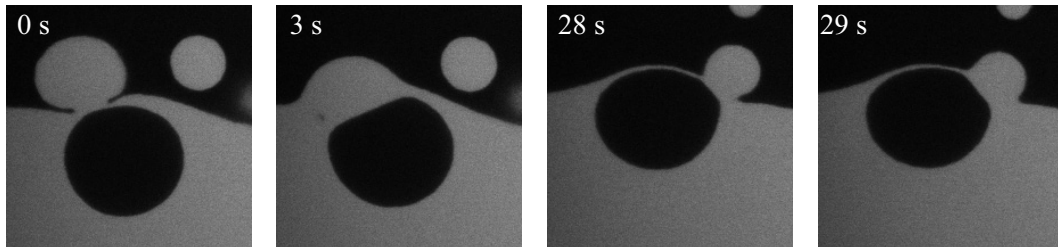


FIGURE 7.11. The liquid drops push their material into the thin liquid film, which distorts the interface at the gas bubble side as well. The image size is $84 \times 84 \mu\text{m}^2$. System 2 PPD25, statepoint I.

Another discussion in the hydrodynamics of coalescence is where the droplet material goes and what the flow pattern is; the surface free energy gained is transformed into flow, which redistributes the material. By bleaching either the coalescing drop or the bulk phase in which the drop is coalescing, it is possible to follow the liquid material into the bulk phase, see figure 7.10. Clearly, the interfaces first retract and in the next step the liquid material is pushed into the bulk phase. It forms a clear hemisphere independent of where the first connection takes place. The liquid drop material then has to spread due to diffusion which is a relatively slow process, see chapter 9 for measurements of the diffusion coefficients. In fact, by carefully inspecting the events shown in figure 7.10 we observe that in the top row the crucial wave fluctuation is done by the bulk phase, while in the bottom row it originates from the droplet. Another coalescence scheme also provides information. In figure 7.11 a liquid drop coalesces on top of a gas bubble that is close to coalescence. Due to the flow of the liquid material into the thin draining liquid film we see the film being distorted up to a level where the interface becomes flat. These observations may contribute to a further understanding of the hydrodynamics of coalescence.

7.5. CONCLUSION

We have shown the three consecutive stages in droplet coalescence in fluid-fluid phase separated colloid-polymer mixtures. The data can be obtained in a single system with light and laser scanning confocal microscopy and comparing results for three different colloid-polymer mixtures shows that the behaviour is rather general. In stage (i) drainage of the continuous film between droplet and bulk phase occurs. The minimal distance between droplet and surface can be scaled for liquid drops as well as gas drops onto a single mastercurve after taking the gas-liquid density difference and the viscosities into account. This is somewhat remarkable, given the wide range of intermediate structures formed ranging from spherical drop and flat surface to strongly deformed drop and surface. From these data the friction factor can be obtained. At large separations it is in good agreement with the modified Stokes equation for a freely sedimenting/rising fluid drop, whereas it rises considerably at small distances. There, the order of magnitude of the friction factor is in reasonable agreement with theory for a solid sphere approaching a free non-deformable surface [175]. The coalescence continues via the breakup of the film (ii), which is elusive in molecular fluids. Here, it is observed that the breakup itself is a stochastic process dominated by the thermal capillary waves. The waiting time for a certain fluctuation to occur is crucial; It can be directly obtained from experiment. From these measurements it is very likely that a fluctuation of $\sim 1 \mu\text{m}$ at a certain area occurs within a couple of seconds. We are currently incorporating these findings in a theoretical model. In fact, going from system 1 to 3 we observe that stage (ii) is reached fastest in system 3 PPD71, where the

interface roughness is more pronounced and the thin intervening film does not have to drain until very small dimensions. During the third stage (iii) we observe that the neck of the connection grows linearly with time. This is a relatively fast process with respect to drainage over a distance of for example the drop diameter. The order of magnitude of the coalescence velocity is well understood from hydrodynamic scaling arguments and it is proportional to the capillary velocity. We may conclude that the breakup itself is a stochastic process by capillary waves and that before and after the breakup, hydrodynamics is important.

8

Droplet snap-off affected by thermal noise

ABSTRACT

We report measurements on droplet snap-off in fluid-fluid phase separated colloid-polymer mixtures. The process occurs spontaneously during phase separation and provides a convenient, non-interfering way to study the phenomenon. Since the interfacial tension is ultralow, the thermal roughness is more pronounced than in molecular systems and we study the possibility of observing a regime where thermal noise is dominant over interfacial tension. To this end we focus on the shape at snap-off, the number of satellite drops formed, and the radius of the neck as a function of time.

8.1. INTRODUCTION

The process of drop formation is frequently observed in every day life. One possible route to create drops is by means of snap-off for example occurring in a dripping faucet, which gives rise to rich and beautiful phenomena. As the radius of the neck decreases, a singularity develops due to the infinite curvature at the point of snap-off [185]. This has generated much interest not only from a physical point of view, but also since one expects that at the singularity lengthscales become arbitrarily small and hence give rise to universal scaling behaviour independent of initial or boundary conditions [186–188]. This has indeed been confirmed in experiment [189] and theory/simulations [190], although in some cases non-universality has been observed [191]. Both just before and after the point of snap-off molecular scales are reached. At such small scales thermal fluctuations start playing a role and recently simulations and theory have shown that this thermal noise greatly influences the observed behaviour [192, 193]. Experiments that observe this scale appear very difficult. Here we show first indicative experimental results of snap-off events in colloid-polymer mixtures influenced by thermal fluctuations.

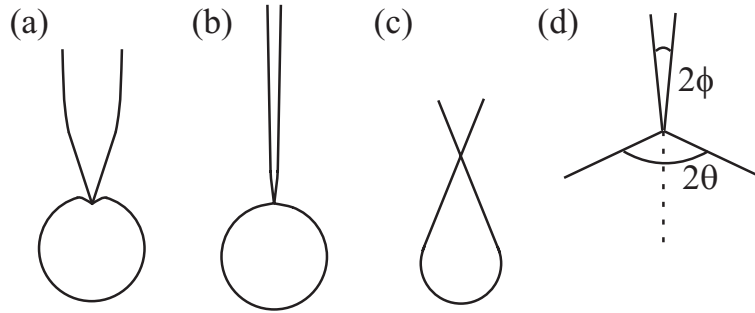


FIGURE 8.1. Schematic drawing of the typical geometries in inviscid (a), viscous (b) and thermal noise (c) breakup. In (d) the opening angles are indicated.

We use several colloid-polymer mixtures to study the droplet snap-off. Such mixtures are often used as model systems for molecular fluids with the advantage that colloids give rise to more accessible time- and lengthscales. This is because the interfacial tension γ , which is the driving term in many hydrodynamic phenomena, is much lower than in molecular systems. Typically, it has a magnitude proportional to [3, 12] $\gamma \sim k_B T / d^2$ with $k_B T$ the thermal energy and d the typical length scale at the interface, similar to the particle diameter σ_c away from the critical point. This order of magnitude has been confirmed in experiment [35–38, 106, 134], theory [102, 103, 120, 129, 130] and computer simulations [135, 136]. For colloids it typically leads to interfacial tensions of $\mu\text{N}/\text{m}$ and below. This has several consequences; the thermal roughness L_T scales up

$$L_T = \sqrt{\frac{k_B T}{\gamma}}, \quad (8.1)$$

and may become of the order of microns. The hydrodynamic inertial regime is reached at a lengthscale L_η of,

$$L_\eta = \frac{\eta^2}{\rho\gamma}, \quad (8.2)$$

and is scaled up to several meters. Here, η is the viscosity and ρ the mass density. Furthermore, the competition between gravity or hydrostatic pressure and interfacial tension sets the capillary length scale L_c

$$L_c = \sqrt{\frac{\gamma}{g\Delta\rho}} \quad (8.3)$$

with $\Delta\rho$ the mass density difference between drop and surrounding fluid and g earth's acceleration. This length is brought down to tens of microns. Finally, another length-scale is of importance as well in the study of droplet snap-off, i.e. the observation lengthscale L_{obs} . The observation lengthscale is of the order of 1 micron in standard optical microscopy setups and can be even smaller in more advanced setups.

The time dependence t of the minimal radius of the snapping neck h can generally be written as [185]

$$h(t) \propto (t_s - t)^\alpha. \quad (8.4)$$

Here, t_s denotes the time at snap-off and the exponent α depends on which hydrodynamics are dominant. For inviscid coalescence, in which inertial terms are dominant, $\alpha = 2/3$ [185, 194]. This is valid at lengths where $L_{obs} > L_\eta > L_T$, which is for instance the case in water. In addition, a cone+spherical cap geometry is predicted at the moment of snap-off, see figure 8.1(a), with opening angles (figure 8.1(d)) of $\theta = 112.8^\circ$ and $\phi = 18.1^\circ$ [195, 196]. In more viscous fluids such as glycerol we find $L_\eta > L_{obs} > L_T$. Viscosity is dominant and $\alpha = 1$ [185, 190, 197]. A thin thread + drop shape is predicted close to snap-off, see figure 8.1(b), and the opening angles are $\theta = 78^\circ$ and $\phi = 6^\circ$ [197]. The values for α can also be obtained following the scaling approach presented in chapter 9. In colloid-polymer mixtures it is now possible to get in the range $L_\eta > L_{obs} \sim L_T$, which has several interesting consequences [192]. Thermal noise becomes important and even dominant and theory predicts a power law with $\alpha = 0.42$ [193]. Furthermore, simulations [192] and theory [193] predict that at snap-off the shape of the drop and thread becomes much more symmetric like a double cone-neck (hourglass shape) with roughly equal opening angles, see figure 8.1(c). Finally, hardly any satellite drops are predicted to be formed at snap-off, implying that with thermal noise the size distribution of snapping drops becomes slightly broader and single peaked, instead of two distinct sharp peaks (main and satellite drops) [192, 193]. In all of the above predictions gravity is absent, but in colloid-polymer mixtures gravity may play a role, since the capillary length L_c is relatively small (see also the discussion in section 7.2).

8.2. EXPERIMENT

During the initial stages of phase separation (see chapter 9) liquid phase is formed throughout the mixture. Close to the macroscopic air-dispersion meniscus liquid phase nucleates at the interface, see figure 8.2. In addition, material is also present at the glass walls above the meniscus due to homogenization by shaking and liquid phase subsequently drips down to the meniscus as well (figure 8.2(c)). Since this macroscopic meniscus is slightly curved, the drops glide to the lowest part of the interface and at a certain critical size start dripping down. This behaviour has been observed in all three colloid-polymer mixtures studied in this thesis, but also in e.g. a mixture of xanthan (bio)polymer and teflon spheres in water [198]. The dripping drops are being formed in a spontaneous, but highly reproducible manner. Here, we study the detachments of the droplets; we show results for system 1 SPC13 in detail, which is a mixture of silica colloids and poly(dimethylsiloxane) polymer in cyclohexane. The colloid is relatively small, such that the interfacial tension is relatively large. Furthermore, we show first

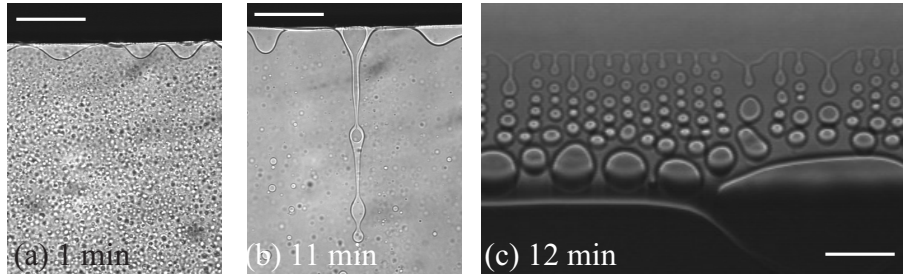


FIGURE 8.2. Collection of liquid material during phase separation at the lower side of (a,b) and at the wall above (c) the air-dispersion meniscus. The white bars are placed inside the meniscus. The drops are liquid phase. In (b) gas is trapped inside the liquid cylinder. Times are in minutes after homogenization of the sample. Image sizes are $705 \times 890 \mu\text{m}^2$ (a,b) and $515 \times 325 \mu\text{m}^2$ (c). System 1 SPC13, statepoints II (a,b) and I (c) (chapter 2).

results for system 3 PPD71, which is a mixture of PMMA colloids and poly(styrene) polymer in decalin. Here, the colloids are relatively large and the interfacial tension is thus small. The physical properties of these systems are presented in chapter 2. We observe that system 2 PPD25 shows similar behaviour as system 1.

System 1 has been studied with the transmission light microscopy setup as described in chapter 2. It is equipped with a CCD camera with a capturing rate of 50 frames per second. Although the refractive indices of liquid and gas phase are rather similar the interface can be clearly observed. System 3 has been studied with the LSCM setup, see chapter 2 as well. We are interested in the minimal neck radius as a function of time t to snap-off. The interface between gas and liquid phase can easily be located automatically using routines written in IDL [199], see the Appendix of this chapter.

8.3. RESULTS

In figure 8.3 we show snapping droplets for systems 1 SPC13 (a) and 3 PPD71 (b,c). Clearly, the shapes at snap-off are rather different. In (a) the shape is asymmetric, and we find on average $\theta_1 = 62^\circ \pm 3.4^\circ$ and $\phi_1 = 1.8^\circ \pm 1.2^\circ$ (see figure 8.1(d) for the definition of angles). After the large drop snapped off, the filament also detaches from the top as shown in figure 8.4. The neck at the top part gets thinner and snaps off in a way that is apparently similar as the first drop, as also observed in inviscid coalescence [188]. Here, $\theta_2 = 64^\circ \pm 3.9^\circ$ and $\phi_2 = 3.6^\circ \pm 1.7^\circ$, where ϕ_2 is the opening angle of the filament and corresponds to ϕ_1 , just as θ_2 corresponds to θ_1 . Theory predicts $\theta = 78^\circ$ and $\phi = 6^\circ$ for the capillary breakup of a viscous thread surrounded by another viscous fluid [197], in reasonable agreement with experiment. Now, in figure 8.3(b) and (c) the roughness by thermal fluctuations can be clearly observed and the shape at snap-off is much more symmetric, especially for the event in (c), in line with simulations [192] and theory [193]. Here, a double cone-neck shape is predicted. In addition, the number of crests and

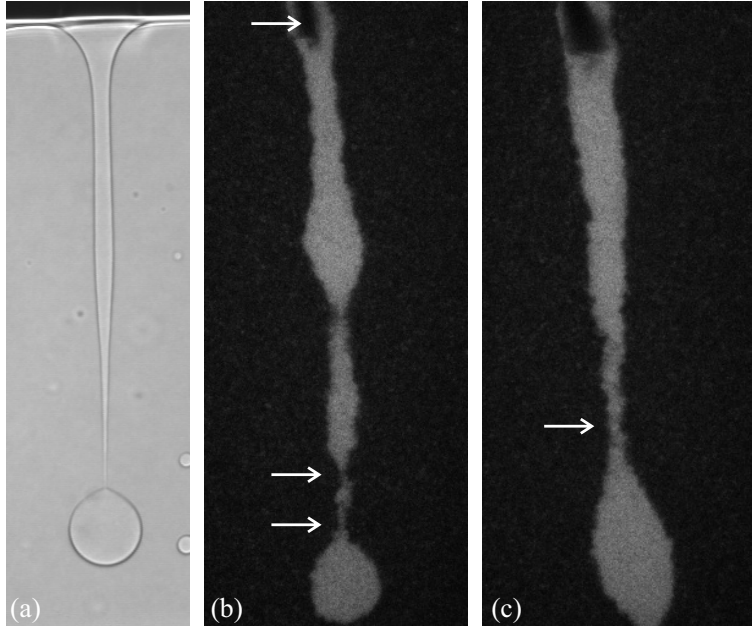


FIGURE 8.3. Snap-off events for system 1 (SPC13, statepoint III) (a), and system 3 (PPD71, statepoint VII) (b) and (c). In (a) the neck shape is highly asymmetric. The image size is $154 \times 528 \mu\text{m}^2$. In (b) and (c) two different events are shown. At snap-off (indicated by the arrows) the neck shapes are rather different than in (a). In (b) only two and in (c) zero satellite droplets will be formed. In the top of the image the glass stick can be seen (see the top arrow), which acts as a collector of liquid material and facilitates the snap-off. The image size is 59×235 (b) and 59×223 (c) μm^2 .

throughs at the filament typically increases. Finally, hardly any satellite drops are being formed in system 3, in clear contrast with system 1, see figure 8.5. In sum, the observations in system 3 are in line with predictions by Moseler and Landman [192] and Eggers [193], see especially figures 3A-C in [192].

To further quantify the differences it is possible to determine the exponent α of snap-off, see equation (8.4). Unfortunately, the time resolution with LSCM is not yet sufficient to determine the exponent α accurately for system 3, though we need the optical resolution of LSCM given the importance of L_{obs} as discussed in the introduction. Therefore, we now are only able to determine α in system 1.

From the image analysis it is easy to find the centre of the droplet as a function of time. In figure 8.6 we plot the vertical distance between the centre of the drop at time t with respect to its position at t_s . Here, several events are plotted. The top line is of a large drop with a final diameter of $63 \mu\text{m}$. Initially, the drop accelerates, until it reaches a constant velocity at about 1.5 s before t_s . The open symbols stem from a different event with a drop of equal size. The data lie on top of each other underlining the reproducibility of the events. In addition, the shape of the neck changes

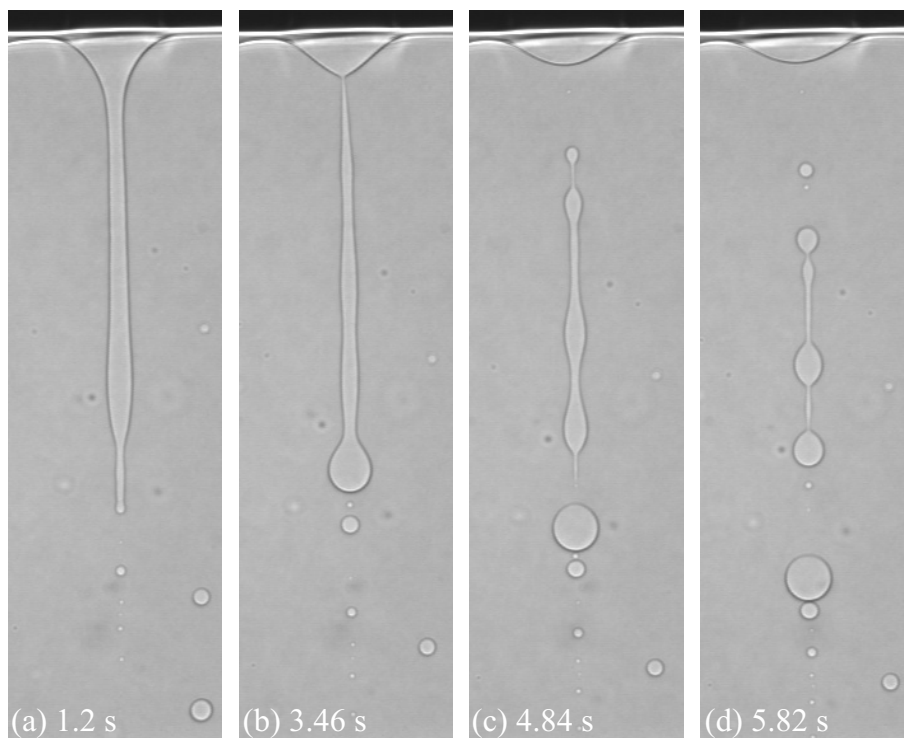


FIGURE 8.4. Second snap-off following after the first snap-off. The remaining filament immediately becomes Rayleigh unstable and the instabilities grow in time. The image size is $154 \times 528 \mu\text{m}^2$. Times are with respect to the first snap-off event, i.e. figure 8.3(a). System 1 SPC13, statepoint III.

from roughly parabolic/symmetric (figure 8.6(b)) to asymmetric (figure 8.6(c)) around the time that a constant velocity is reached. Please note that this discussion about the neck geometry is different from the discussion about the neck shape at snap-off (section 8.1), since this occurs well before snap-off. Such a change in shape has been observed in experiments on a glycerin-water mixture as well, but there this effect was analyzed in terms of inertia [200], which is very unlikely in colloid-polymer mixtures, since L_η is on the order of meters, see section 8.1. The two other lines are for two smaller snapping droplets with final diameters of $41 \mu\text{m}$ (top) and $31 \mu\text{m}$ (bottom). The shape of the curves are similar, although their final velocities are reached closer to t_s . The final velocity of the large droplets is somewhat larger than the velocity of sedimenting droplets close (but not too close) to the flat interface, see chapter 7.

In figure 8.7 we plot the minimal neck radius h as a function of time to snap-off for the first (a) and second (b) snap-off. In (a) three different events are plotted, two large droplets snapping off and one small droplet. The data of the large droplets fall on top of each other, whereas the data corresponding to the small droplet join the general curve closer to the time to snap-off. Since close to t_s the three events follow the same curve, we conclude that there is a proper separation of lengthscales close to snap-off and the

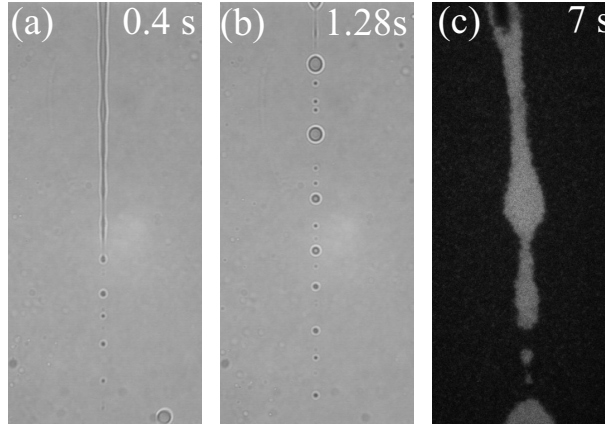


FIGURE 8.5. Formation of satellite droplets after the snap-off of the first (large) liquid droplet. In (a) and (b) the image size is $242 \times 527 \mu\text{m}^2$ and shown are data for system 1 SPC13, statepoint I. In (c) the image size is $59 \times 235 \mu\text{m}^2$ and data are for system 3 PPD71, statepoint VII. Times are with respect to t_s .

initial conditions do not influence this part. In fact, this behaviour is verified for many more events (> 10) and is also observed in system 2 PPD25. For sake of clarity we only show a few events for system 1 SPC13. The snap-off event is seen to be divided into different regimes. Far away from the point of snap-off the droplet is still accelerating

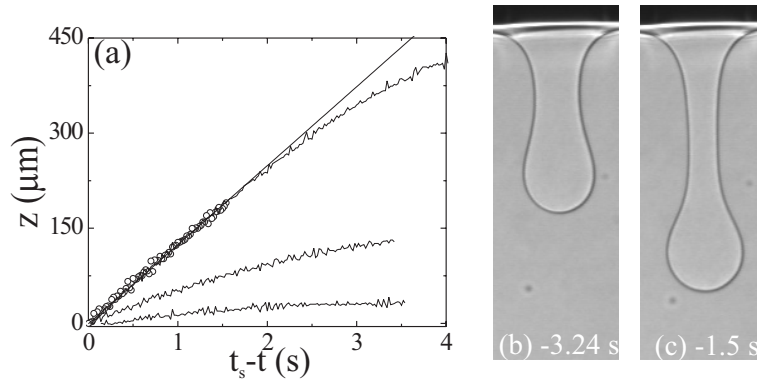


FIGURE 8.6. (a) Position of the centre of the drop with respect to its position at snap-off. The top curve and the symbols correspond to drops of diameter $63 \mu\text{m}$. The middle and bottom curve are for drops of $41 \mu\text{m}$ and $31 \mu\text{m}$, respectively. The large drops reach an almost constant velocity about 1.5 s before snap-off, indicated by the drawn line. The smaller drops reach a constant velocity closer to t_s . In (b) and (c) the subtle change of geometry of the neck shape is shown. In (b) the interfacial profile is still roughly parabolic and symmetric, whereas in (c), which is just after the transition point, it has flattened off, similar to observations in [200]. Times are with respect to t_s and data are for system 1 SPC13, statepoint III.

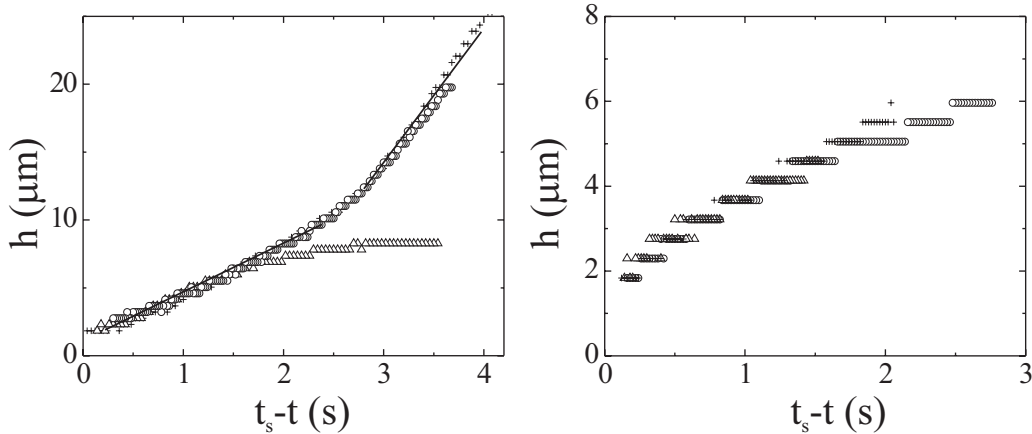


FIGURE 8.7. Radius of the neck as a function of time for several droplets for the first (a) and second (b) snap-off event. In (a) the full lines denote $\alpha = 1$. The exact point of snap-off has some uncertainty due to the finite time and space resolution. The data in (b) fall on top of the data in (a) close to snap-off. Data for system 1 SPC13, statepoint III.

while falling. Here, the radius of the neck is larger than the capillary length L_c , which is $16 \mu\text{m}$ for this statepoint. The neck shrinks with a constant velocity of about $10 \mu\text{m/s}$. At a certain point the slope changes, which is also close to the point where a constant sedimentation velocity is reached and a transition in geometry of the neck is observed. In this regime the neck shrinks linear in time as well with a velocity of about $3.7 \mu\text{m/s}$. Theory for a viscous drop in inviscid surroundings predicts velocities of $0.071 \gamma/\eta$ for symmetric snap-off with a parabolic neck shape [201] and $0.03 \gamma/\eta$ for asymmetric snap-off [190], as observed in [200]. Here, the magnitude of the two velocities is much larger, since the capillary velocity γ/η is of the order of $10 \mu\text{m/s}$, although their ratio is (perhaps coincidentally) close to the theoretical one. Moreover, the effects of the outer viscosity and especially of gravity have not been included in these theories. Since the sedimentation velocity of the drops is larger than the capillary velocity, both gravity and interfacial tension are expected to play a role in snap-off. Finally, in these linear regimes the exponent α is clearly equal to 1, indicated by the full lines.

The second snap-off, that in the top of the liquid cylinder (figure 8.4), can be analysed in a similar fashion and leads to figure 8.7(b), where three different events are shown. The data collapse on figure 8.7(a) close to snap-off, but further away the difference is large. In this case, we do not observe a linear dependence. In fact, the shape of the curve corresponds reasonably well to $\alpha = 0.42$, which is the prediction for snap-off dominated by thermal noise [193], but it is uncertain if this prediction applies for the second snap-off as well [202]. Furthermore, it is unclear where the difference in power-law behaviour between the first and second snap-off stems from. However, in the first

case a large droplet pulls the shrinking neck, whereas in the second snap-off the neck's position remains at the same spot. The effect of gravity on snap-off is currently being taken into account in extensive calculations/simulations [202].

8.4. CONCLUDING REMARKS

In phase separating colloid-polymer mixtures liquid phase spontaneously formed in the top of the mixture and slowly started dripping down during many hours after the macroscopic gas-liquid interface had emerged. This provides a convenient way to study the process of droplet snap-off in full detail in systems with ultralow interfacial tensions. The driving forces for snap-off are small and video speed camera-equipment can be used.

In system 1 SPC13, where the interfacial tension is relatively large and the thermal roughness therefore small, we observe a long thread-drop shape at snap-off as well as the formation of many satellite droplets, although this number decreases closer to the critical point. The large snapping drops reach a constant velocity about 1.5 s before the snap-off occurs. At that instant, the minimal neck radius as a function of time shows a change of slope and the geometry of the neck shape changes as well. The linear dependence of the neck radius corresponds to an exponent α of 1. In the second snap-off we observe different behaviour. In these snap-off events the effects of gravity may play an important role, which is currently under investigation. Although we are orders of magnitude closer to “molecular” lengths than in presently available molecular experiments, the effects of thermal noise seem to be minimal. This might have to do with an optical limitation: the thermal length L_T is of the order of $0.1 \mu\text{m}$ for the present statepoint, whereas the optical resolution is about $1 \mu\text{m}$, i.e. $L_{obs} > L_T$.

In a system where thermal noise is more pronounced and $L_\eta > L_{obs} \sim L_T$, i.e. system 3 PPD71, we do observe that hardly any satellite droplets are formed. Furthermore, the appearance of the snap-off event is very similar to predictions by Moseler and Landman [192]. We will combine LSCM and transmission light microscopy data to accurately determine the exponent α in this system as well.

APPENDIX: ROUTINE TO TRACK THE SNAP-OFF OF DROPLETS

The interface of the falling droplet can easily be located automatically since at the interface the intensity is minimal. The maximal radius, i.e. the radius of the droplet, is used to track the falling droplet. It sets the boundaries between which the search for the minimal neck radius occurs. The neck radius can then easily be followed in time, see the images in figure 8.8.

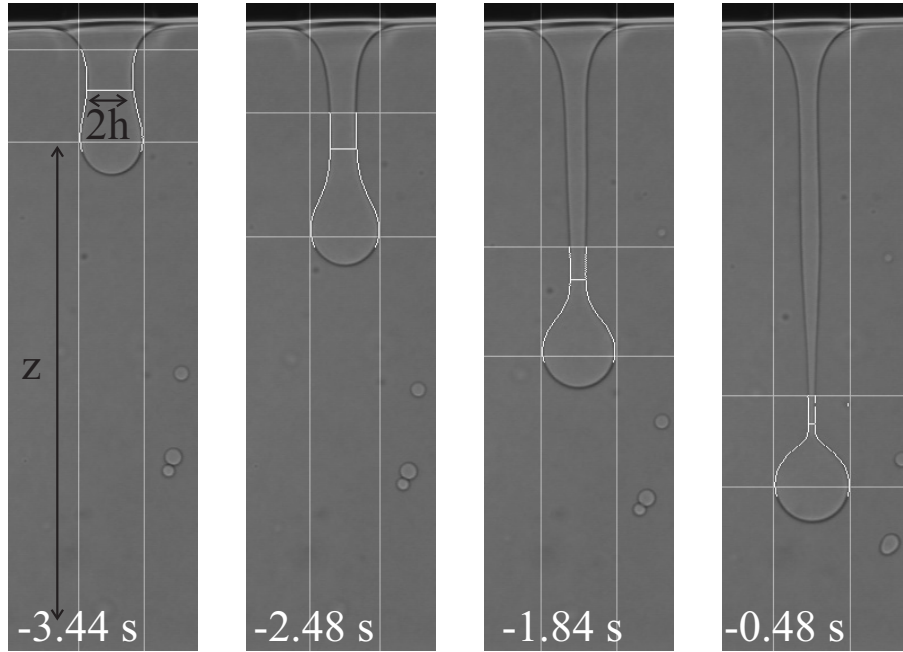


FIGURE 8.8. Analysis used to track the snap-off event. The horizontal bottom line indicates the maximum diameter of the snapping droplet and is used to locate the droplet's center. Once the center is found, the horizontal and vertical lines are set as well. In the enclosed rectangle the minimal neck radius is searched. The located minimum is indicated by the middle horizontal line. In the next frame the rectangle is slightly expanded, the interfacial profile is searched from opposite sides and the procedure is repeated. The image size is $154 \times 528 \mu\text{m}^2$ and times are with respect to t_s . System 1 SPC13, statepoint III.

9

Interfacial dynamics in demixing systems with ultralow interfacial tension

ABSTRACT

We report measurements on fluid-fluid phase separation in a colloid-polymer mixture, which can be followed in great detail due to the ultralow interfacial tension. The use of the real-space technique laser scanning confocal microscopy leads to clear, well defined images making quantitative comparisons to theory possible and being highly instructive. Simple scaling arguments are given why in experiment three steps of the phase separation can be observed: an interfacial tension driven coarsening, gravity driven flow, and finally the interface formation. All these processes are observed in a single experiment. The first stage can be quantitatively described by viscous hydrodynamics. Coarsening occurs through pinch-off events. The second stage begins at a typical size of $\sim 2\pi$ times the capillary length reminiscent of the Rayleigh-Taylor instability. The liquid phase breaks up and becomes discontinuous. There is strong directional flow in the system, but the Reynolds number remains much smaller than unity. Finally, the macroscopic interface is formed growing upwards with a velocity comparable to the coarsening velocity in the initial stage. Again, viscous hydrodynamics apply with a characteristic velocity of the interfacial tension over the viscosity.

9.1. INTRODUCTION

The study of the morphology and kinetics of phase separation processes follows a long tradition and remains of fundamental importance [203]. The early initial stages of the phase separation are determined by the underlying free energy landscape, whereas the

observed morphology kinetically depends on characteristic fluid properties as well [204], of which the viscosity and interfacial tension are the most important ones. Here, we present a real-space study of the effects of an ultralow interfacial tension on the phase separation kinetics in a fluid-fluid demixing colloid-polymer mixture. This is not only of fundamental importance, but has industrial relevance as well. For example, in the food industry extensive use is made of the properties of polymers, e.g. to invoke gelation [131], and adding these to food suspensions leads effectively to colloid-polymer mixtures [132].

Phase separating colloid-polymer mixtures are well known to display similar behaviour as molecular fluid-fluid demixing systems [205]. The coexisting phases are a colloidal liquid (rich in colloid and poor in polymer) and a colloidal gas (poor in colloid and rich in polymer). The origin of the phase separation lies in the entropy-driven attraction between the colloids, which is mediated by the polymers [19, 24]. It is known from experiment [36, 37, 106, 134] and theory [102, 103, 129], that in such systems the interfacial tension γ scales as $\gamma \sim k_B T / \sigma_c^2$, with $k_B T$ the thermal energy and σ_c the particle diameter, leading to ultralow values for the interfacial tension.

We use laser scanning confocal microscopy (LSCM) to follow the processes of phase separation. This real-space technique leads to clear, well defined images of the several stages of phase separation. Hence, the purpose of this work is to study the effects of the ultralow interfacial tension *and* present images which we believe to be instructive and might assist in a further development in theories on demixing.

Experimentally, the phase separation process can roughly be divided in three stages, which will be made apparent by a consideration of the relevant length- and timescales in demixing systems (section 9.2). Once sharp interfaces have been formed the interfacial tension drives the coarsening of the spinodal structure (section 9.4), which is followed by a gravity driven collapse and flow of the spinodal network (section 9.5), and finally a sharp macroscopic interface is formed and the phase separation has completed (section 9.6). These sections will be preceded by a brief description of the experimental system and methods (section 9.3) and our findings will be summarised in section 9.7.

9.2. LENGTH- AND TIMESCALES

In the unstable region of the phase diagram each density fluctuation in an initially homogeneous system is energetically favourable, but fluctuations with large wavelengths and hence shallow density gradients are thermodynamically more favourable, whereas for short wavelengths particles only have to diffuse over short distances. This competition leads to a fastest growing mode q_m within the framework of Cahn-Hilliard theory of [206–209]

$$q_m^2 = -\frac{1}{2\kappa} \left(\frac{\partial \mu}{\partial n} \right). \quad (9.1)$$

Here, κ is the Cahn-Hilliard square gradient coefficient [206, 207] (like the van der Waals square gradient coefficient), n is the overall number density and μ the chemical potential. The wavelength $L \equiv 2\pi/q_m$ that follows from (9.1) is a few times the particle diameter d for colloid-polymer mixtures away from the critical point, as for example can be verified by using theory presented in Ref. [130], see also chapter 4. As time proceeds the system approaches its equilibrium densities and the gradients in the density get steeper [210].

At the same time the system coarsens and L grows in the diffusive regime as [211]

$$L(t) = \left(\frac{k_B T}{\eta} t \right)^{1/3}. \quad (9.2)$$

A simple way to understand this diffusive coarsening is by considering the velocity of an object of size L driven by chemical potential gradients of magnitude $\propto k_B T/L$, i.e.

$$\frac{dL}{dt} = \frac{-\nabla\mu}{f} \propto \frac{k_B T/L}{\eta L}, \quad (9.3)$$

with f the friction of magnitude ηL and η the viscosity. Integrating (9.3) immediately leads to (9.2).

Upon the formation of sharp interfaces the interfacial tension γ starts playing a role. Here, we will follow didactic derivations of especially Siggia [211] and Bray [212]. A more extended scaling analysis is given by Kendon *et al.* [213]. The dynamics are governed by the Navier-Stokes equations

$$\rho D_t \mathbf{u} = \eta \nabla^2 \mathbf{u} - \nabla p - g \Delta \rho \mathbf{e}_3. \quad (9.4)$$

The left hand side of (9.4), with ρ the mass density, D_t the material derivative and \mathbf{u} the velocity, captures the inertial terms and is much smaller than the viscous dissipation -the first term of the right hand side of (9.4)- if the Reynolds number is small. The last term accounts for the hydrostatic pressure with g earth's acceleration, $\Delta \rho$ the mass density difference between the two phases and \mathbf{e}_3 a unit vector pointing along gravity. For small L gravity is not yet important and the interplay between viscous dissipation and gradients in the pressure p due to the Laplace pressure,

$$\eta \nabla^2 \mathbf{u} \propto \eta \frac{1}{L^2} u \text{ and } \nabla p \propto \frac{1}{L} \frac{\gamma}{L}, \quad (9.5)$$

leads to a (capillary) velocity in the viscous hydrodynamic regime of

$$u_c \propto \frac{\gamma}{\eta}, \quad (9.6)$$

of which the prefactor was estimated to be 0.1 [211]. In extensive computer simulations of two incompressible fluids of maximal symmetry, i.e. identical viscosity, density and volume fraction, the prefactor was found to be 0.072 [213, 214]. The magnitude of this

interface velocity becomes comparable to the diffusive coarsening velocity of (9.3) at a cross-over length of [211]

$$L \propto \sqrt{\frac{k_B T}{\gamma}} \equiv L_T, \quad (9.7)$$

which is also the thermal length (chapter 1). From there on the system coarsens linearly with time proportional to (9.6).

At a Reynolds number $Re = \rho u L / \eta$ of order one inertial terms start playing a role. Using the capillary velocity (9.6) as characteristic velocity we find that at a cross-over length of

$$L_\eta \propto \frac{\eta^2}{\rho \gamma}, \quad (9.8)$$

the inertial hydrodynamic regime is entered (see for example [212]). The balance between gradients in pressure (see (9.5)) and inertia,

$$\rho D_t \mathbf{u} \propto \rho \frac{L}{t^2}, \quad (9.9)$$

then leads to a coarsening of [212]

$$L(t) \propto \left(\frac{\gamma}{\rho} t^2 \right)^{1/3}. \quad (9.10)$$

This $t^{2/3}$ -regime was first predicted by Furukawa [215]. Finally, the gravity term in (9.4) becomes as large as the Laplace pressure (9.5) at [211],

$$L \propto \sqrt{\frac{\gamma}{g \Delta \rho}} \equiv L_c, \quad (9.11)$$

which is precisely the capillary length L_c and the phase separation becomes gravity driven.

During this gravity driven flow we find in our experiment that one of the phases becomes discontinuous -in our case the heavy liquid phase- and the interface emerges at the bottom of the container. Individual droplets sediment towards the emerging interface. They form a structure of droplets on top of each other which resembles a foam. For ultralow interfacial tensions the coalescence is governed by viscous forces and inertial terms do not play a role, see chapter 7. In that case the capillary velocity (9.6) again sets the scale and after all droplets of both phases have coalesced the system has fully phase separated.

In molecular systems, where the interfacial tension is relatively large, inertial terms may be expected to become important at lengths smaller than the capillary length. See for estimates of the lengths in both molecular and colloid-polymer mixtures table 1.1 [106]. However, in experiments with molecular fluids the inertial regime has not yet been observed [203]. Of course, the prefactor of (9.6) used in the estimate of (9.8)

postpones the inertial regime to larger lengthscales, though this factor alone does not suffice as explanation. In the aforementioned simulations [213, 214, 216], in which the inertial regime is observed, it is found that the cross-over does not occur at $Re = 1$, but at much larger Reynolds numbers, a further explanation of the lack of experimental evidence for the occurrence of the inertial regime. In contrast to molecular systems, colloidal systems are expected to remain for long periods of time in the viscous regime and -following the above scaling arguments- gravity driven flow occurs well before the inertial regime. Furthermore, in the case of colloid-polymer mixtures inertial terms do not play a role either during the interface formation.

9.3. EXPERIMENTAL SYSTEM AND METHOD

We will focus on a system consisting of small poly(methylmethacrylate) (PMMA) spheres with a radius of $R_c=25$ nm and poly(styrene) polymer with a radius of gyration $R_g = 14$ nm, i.e. system 2 PPD25, chapter 2. Samples were prepared by mixing colloid- and polymer-stock dispersions and diluting with decalin. The resulting macroscopic interface always was very sharp. See figure 2.3(a) for the complete phase diagram [107]. To study the colloid-polymer mixtures we used a laser scanning confocal head (Nikon C1) mounted on a horizontally placed light microscope (Nikon Eclipse E400), see figure 2.4(a). The microscope detects the fluorescence of excited dye in the colloids, while solvent and polymers remain dark. Hence the colloidal rich phase (liquid) appears bright, whereas the colloidal poor phase (gas) appears dark. We used low numerical aperture objectives in order to have a larger field of view and to obtain some three dimensional information instead of imaging only a very thin slice. Since the relevant lengthscales are not of the order of the particle diameter as in most LSCM-studies, but of the order of at least several μm the sectional power of the LSCM can still be exploited.

In the present chapter we focus on a sample with $\phi_c = 0.076$ and $\phi_p = 0.50$ (statepoint I in figure 2.3(a)), which is reasonably close to the critical point. The complete phase separation took about 20 minutes, of which the initial coarsening took 50 s (section 9.4), the gravity driven flow in the middle of the sample 5 minutes (section 9.5) and the interface formation the remaining time (section 9.6). Other statepoints show basically similar behaviour, except if close to the binodal the metastable region is entered where phase separation proceeds via nucleation and growth.

The system has been extensively characterized; we obtained an interfacial tension of $\gamma = 2 \cdot 10^{-7}$ N/m by analyzing the thermally induced capillary waves in a similar manner as done in [134], see chapter 6, and a capillary length of $L_c = 17.6 \mu\text{m}$ by measuring the colloidal gas-colloidal liquid interfacial profile close to a wall [106], see chapter 5. The densities of the gas and liquid phases have been measured with an Anton-Paar density meter resulting in a density difference of $\Delta\rho = 53 \text{ kg/m}^3$ and via (9.11) to

$\gamma = 1.6 \cdot 10^{-7}$ N/m, in good agreement with the capillary wave approach. We will use the value obtained from the capillary length, since this method is more suited for this relatively large interfacial tension than the capillary wave approach. Furthermore, the viscosities of the two phases have been measured on an Anton Paar Physica MCR300 rheometer giving $\eta_G = 8$ mPa s for the gas (G) phase and $\eta_L = 31$ mPa s for the liquid (L) phase.

The diffusion coefficients in the gas and liquid phase have been measured by performing real-space fluorescence recovery after photobleaching experiments (real-space FRAP) [107,217]. Since this technique is not standard yet, the experimental details are given in the Appendix of this chapter explicitly. The diffusion coefficient in the liquid phase is $D_L = 4.9 \cdot 10^{-13}$ m²/s and in the gas phase $D_G = 1.9 \cdot 10^{-12}$ m²/s, measured after phase separation had completed.

During the homogenization of the colloid-polymer mixture air bubbles can be present in the system. When they escape the spinodal structure is destroyed and this immediately leads to individual drops. Besides that, in the top of the sample drops are formed much earlier. Therefore, we carefully homogenized the sample to minimize the number of air bubbles and always imaged at the final interface position.

9.4. INITIAL PHASE SEPARATION

Directly after homogenization the phase separation starts. From the bicontinuous structure in figure 9.1 it is immediately clear that the system separates through spinodal decomposition. Already in the first images, which are taken 3 s after homogenization, the interfaces are sharp and the system coarsens linearly with time as will be shown below. This is similar to the observations made in [45], where the focus of the work lay on the initial stage of phase separation. From the estimates of (9.1) and (9.7) we find that the linear Cahn-Hilliard regime takes a very short time, as does the diffusive regime with the $t^{1/3}$ coarsening. Colloids only have to diffuse over a few times their own diameter before the viscous hydrodynamic regime is reached. From the colloidal diffusion coefficients in the gas and liquid phase –as measured by the real space FRAP technique– we see that the viscous regime is reached in less than a second and therefore the preceding regimes are not observed.

The system can coarsen via coalescence or pinch-off events. In 2D such events are similar, but in 3D they are distinctly different and here the system mostly coarsens through pinch-off. In the bottom row of figure 9.1 such an event is marked and the insets in figure 9.1(e) show a zoom in on this event. During a pinch-off the liquid bridge drains and snaps more or less symmetrically at a certain point. According to simulations by Cates and co-workers [216] the retracting tips might evaporate a bit, but we do not have sufficient space and time resolution to determine this. There is no recoil and an overdamped relaxation. Many more similar events can be observed,

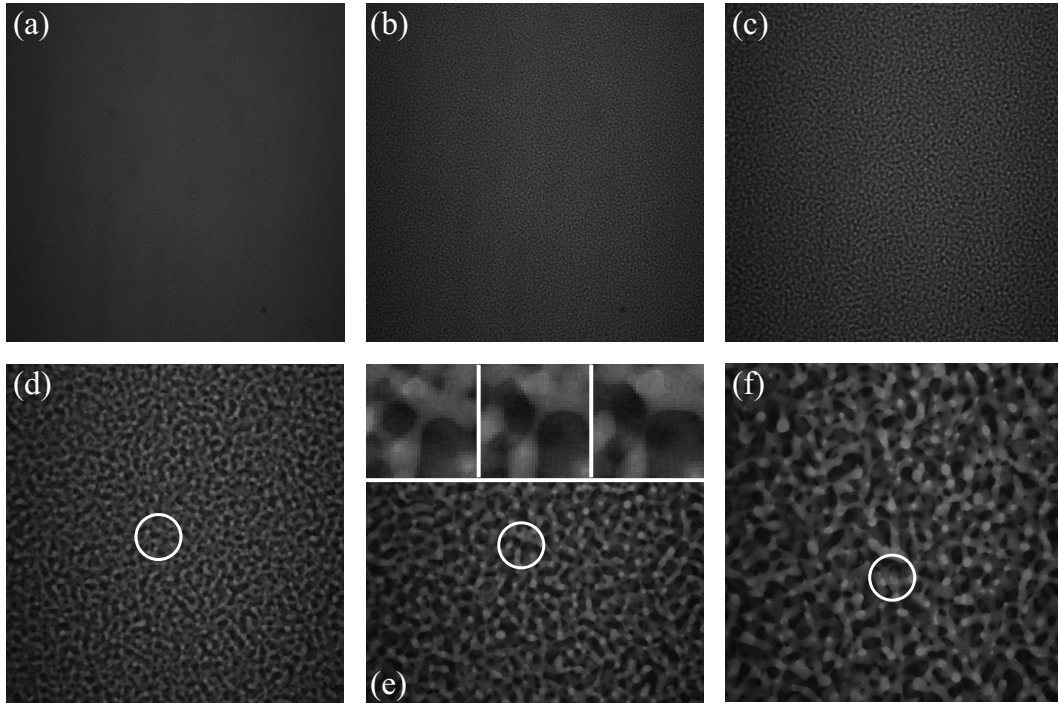


FIGURE 9.1. LSCM images ($1400 \times 1400 \mu\text{m}^2$) of a phase separating colloid-polymer mixture. Gravity points downwards (in all images). Directly after homogenization a spinodal structure is observed (a, $t = 3$ s), which immediately coarsens in time (b, $t = 7$ s) and (c, $t = 11$ s). From (d, $t = 22$ s) it is evident that coarsening occurs through pinch-off instead of coalescence and one can follow such events in time (e, $t = 33$ s) and (f, $t = 45$ s). The white circle marks such an event. The insets ($109 \times 109 \mu\text{m}^2$) zoom in on the pinch-off event (from left to right, $t = 29, 33, 37$ s).

especially of snapping liquid necks surrounded by gas phase, since the liquid has a stronger fluorescence than the gas phase.

The collective overdamped motion of the interface leads to a coarsening of the spinodal structure. One possible way to analyze the structure was clearly demonstrated by Hashimoto *et al.* [218], who -for one of the first times- performed LSCM experiments on spinodally demixing polymer mixtures and paid special attention to the topology of the spinodal structure. Here, we are interested in the coarsening rate, which can best be quantified by performing discrete Fourier transforms of the LSCM-images, see for example figure 9.2(a), which shows the Fourier transform of figure 9.1(c). The Fourier transforms are radially averaged, see figure 9.2(b). In fact, the structure factors obtained in such a manner scale dynamically in time. Although we perform a Fourier transform on a 2D image Guenon *et al.* [219] showed that the resulting radially averaged “structure factor” agrees remarkably well with results from light scattering experiments, where the interfaces and not the domains are seen. Binder and Stauffer

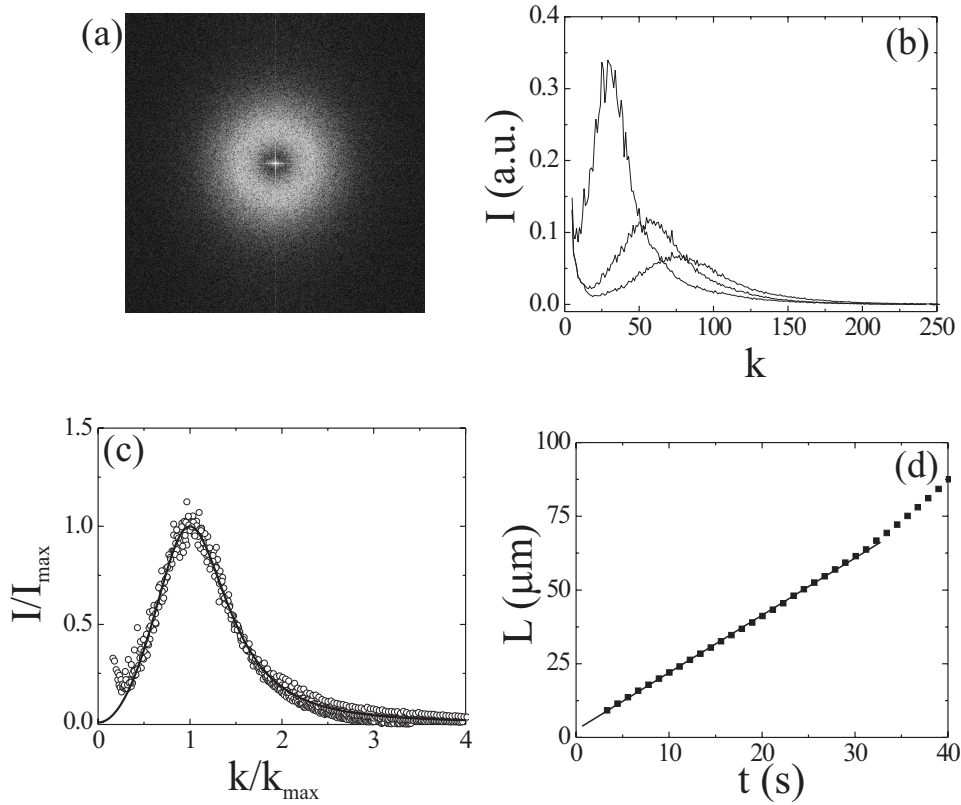


FIGURE 9.2. (a) Discrete Fourier transform of the LSCM image in figure 9.1(c). (b) Radial averages of the Fourier transforms for times 7, 11 and 22 s showing a shift in the position of the maximum intensity to smaller k values. One pixel in k -space corresponds to 2π over the image width L_{image} . The intensity increase at small k -values stems from instrument properties and contains no relevant physical information. (c) Dynamical scaling of the structure factor as a function of I/I_{max} vs. k/k_{max} for the radial averages of (b). The full line is the prediction for off-critical demixing systems by Furukawa (9.13). From the positions of the maximum intensity the characteristic length L can be obtained, which is plotted as a function of time in (d), where the full line is a linear fit up to the first 30 s.

predicted that the structure factor, which we recognize here directly as $I(k, t)$, should scale dynamically as [220]

$$I(k, t) = k_{max}^{-3} F(k/k_{max}) \quad (9.12)$$

with k_{max} the time-dependent wave-vector at the maximum intensity $I_{max} \equiv I(k_{max}, t)$ at time t and with F a universal scaling function. This scaling is not directly observed here, and it has been suggested [221–223] to divide the left hand side of (9.12) by $\int I(k', t) k'^2 dk'$, which is explained in [45]. This integral is hard to perform in this real space experiment due to lack of statistics and effects of the objective properties. By

dividing $I(k, t)$ by I_{max} this problem is circumvented and $I(k, t)/I_{max}$ collapses onto a single master curve as a function of $k/k_{max}(t)$, as shown in figure 9.1(c). The shape of the curve is quite well described by Furukawa's theory [224] for off-critical demixing systems,

$$I = I_{max} \left(\frac{3(k/k_{max})^2}{2 + (k/k_{max})^6} \right). \quad (9.13)$$

The position of the maximum intensity shifts inwards as a function of time. The position k_{max} corresponds to a length $L = L_{image}/k_{max}$, where L_{image} is the image width. In figure 9.2(d) L is plotted as a function of time. There is an initial linear increase in time; L coarsens with a velocity of $1.94 \mu\text{m/s}$ over the first 30 s. For longer times determining the typical size L by Fourier transforming becomes more unreliable. From (9.6) and the quantities for the interfacial tension and the viscosities (section 9.3) a velocity of $\gamma/\eta_L \sim 5.2 \mu\text{m/s}$ up to $\gamma/\eta_G \sim 20 \mu\text{m/s}$ is obtained, which is directly connected to the measured coarsening velocity, but in a complicated manner. As mentioned in section 9.2 direct simulations [213,214] point to a prefactor of 0.072 in (9.6), but the simulations were performed for a symmetric fluid-fluid mixture of equal viscosity, which is not the experimental situation. Considering the spinodal structure as constructed from many individual fluid (both gas and liquid) cylinders can shed some light on the different terms at play. The breakup rate of a viscous cylinder surrounded by another viscous fluid depends on both the viscosities, the initial distortions and the radius of the cylinder [225]. Taking only the inner viscosity into account can give a reasonable estimate of the breakup rate [37,66] and leads to γ/η_L for liquid and γ/η_G for gas cylinders. In case of a cylinder the prefactor of (9.6) can become of the order of 0.01 or smaller [66], but the prefactor might be much larger given the already heavily curved (i.e. distorted) interconnected structure in the spinodal case. Finally, since there is eventually approximately 70 % gas and 30 % liquid phase, the gas phase must consist of thicker "cylinders", which break up slower. Since both phases initially stay continuous, both breakup rates, and hence both velocities (γ/η_L and γ/η_G), might play a role. The measured velocity is thus a non-trivial combination of the aforementioned terms, eventually leading to $1.94 \mu\text{m/s}$.

9.5. GRAVITY DRIVEN FLOW

The spinodal structure starts to collapse under its own weight after about 36 s at $L = 75 \mu\text{m}$. There is still some coarsening. From about 49 s, i.e. $L \sim 100 \mu\text{m}$ the scattering rings flatten off and there is clear gravity driven flow, see figure 9.3(a). The cross-over from the visous regime to the gravity driven regime is not sharp, but takes about 15 s. Since relatively heavy and light material are mixed together the gravity driven flow is reminiscent of the Rayleigh-Taylor instability [40,226]. In our case the

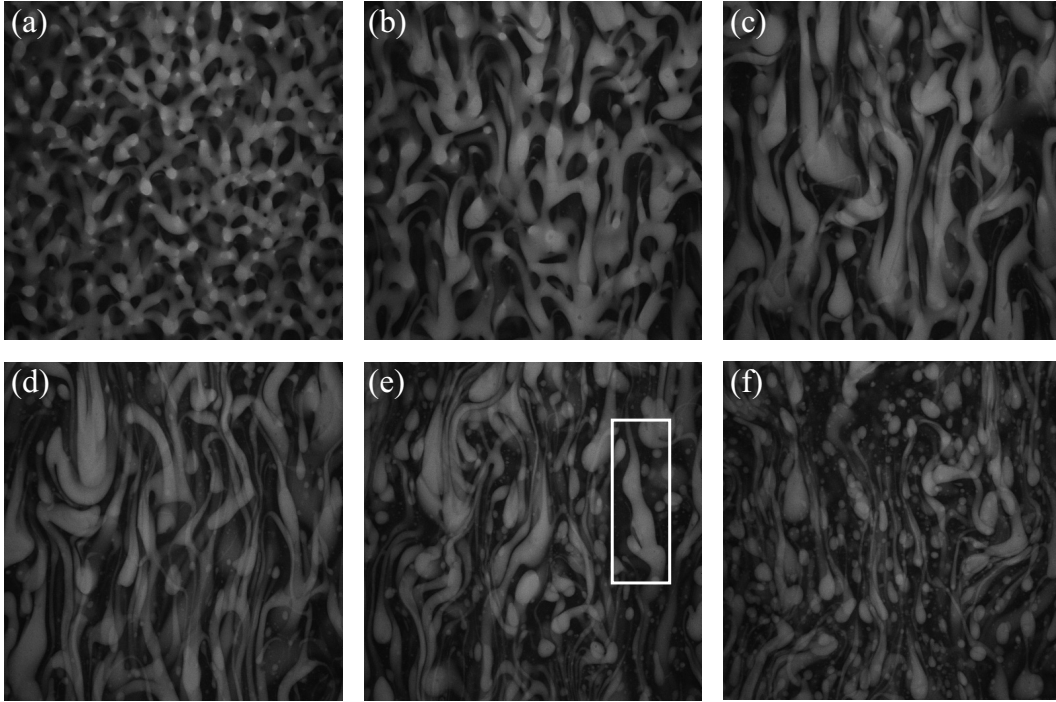


FIGURE 9.3. LSCM-images ($1400 \times 1400 \mu\text{m}^2$) of gravity driven flow in a phase separating colloid-polymer mixture. In (a, $t = 56$ s) the spinodal structure is collapsing under its own weight leading to strong flow in (b, c and d: $t = 72$, 89 and 106 s). Not much coarsening occurs. In (d) the onset to a transition with vertical lanes is observed. In (e, $t = 134$ s) and (f, $t = 178$ s) individual droplets become more apparent. The white box in (e) marks a Rayleigh instability.

fastest growing mode of the Rayleigh-Taylor instability is much larger than the capillary length, but modes with wavelengths of $2\pi L_c$ are already unstable, in good agreement with the observations and the scaling estimate (9.11).

From then on there is a strong flow as well as backflow in the system, see figure 9.3(b) and (c). Sedimenting objects drag other objects along with them leading to directional flow (lane-like structures) and larger sedimenting objects. The largest droplet shaped objects have a maximum size of $\sim 200 \mu\text{m}$ and sediment with a velocity of up to about $70 \mu\text{m/s}$. The Reynolds number, however, remains much smaller than one ($\sim 10^{-3}$). There is not much coarsening in the width of the lanes as can be seen by comparing the structures in figure 9.3(c) and (d). The vertical lanes have a width of about $100 \mu\text{m}$ decreasing to $30 \mu\text{m}$ at later times. For the present statepoint the liquid phase is the minority phase occupying approximately 30 % of the volume. It breaks up, whereas the gas phase remains continuous. During the flow a transition to regular lanes of heavy phase going down and light phase going up can occur as seen in a mixture of teflon spheres and xanthan polymer [198, 227] and in a mixture of silica

colloids and poly(dimethylsiloxane) in cyclohexane [106]. Recently, Wysocki and Löwen theoretically studied similar phenomena in driven colloidal mixtures and found for not too large driving forces good agreement with the classical Rayleigh-Taylor instability [228]. Such formation of lanes clearly is a very efficient way to phase separate. In experiments under shear such lanes are often observed, see for example [203, 229, 230], and in the present system the onset of the transition is observed, see figure 9.3(d), but does not reach the point of distinct lanes. Apparently, either gravity is not strong enough to drive this transition or it takes too long, such that most of the material has already separated.

During the flow not many individual drops are formed. Only at the final stages of the flow more and more droplets can be observed, see figure 9.3(e) and (f). The liquid cylinders are then thin enough that a Rayleigh instability [40] can grow and cause breakup, indicated by the white box in figure 9.3(e). Furthermore, the sedimenting objects disturb each other and this causes additional breakups.

9.6. MACROSCOPIC INTERFACE FORMATION

In the present example, the interface grows from the bottom. The elongated drops become more spherical again close to the forming interface, while the gravity driven structure is still present well above the interface. At the end of the gravity driven flow drops coalesce with their bulk phase, see figure 9.4. Gas droplets inside the liquid phase follow the same pattern. The coalescence is a three step process; the continuous phase drains, a first connection is made, and the material is pushed into the bulk phase, see chapter 7. The first step is time consuming. In the second step the dynamic roughness of the fluid interfaces plays an important role and facilitate the formation of a connection [134]. Moreover, rising gas bubbles induce the breakup as well as can be seen in figure 9.4(e), (f) and (g). In the third step the dynamics are initially governed by viscous hydrodynamics leading to a linear time dependence of the coalescence [169]. Since the interfacial tension is so small, this remains the case and inertia does not become important. In case of molecular fluids it normally does [170].

In the last stages of the interface formation the interface rises with a velocity of approximately $1.5 \mu\text{m/s}$ very similar to the coarsening velocity in the viscous hydrodynamic regime, i.e. proportional to (9.6). Structurally, it is similar to the collapse of an inverse foam. Finally, a sharp interface is formed, see figure 9.4(d). Some individual drops still have to coalesce, especially small droplets. Their sedimentation velocity ($6.4 \mu\text{m/s}$ for a droplet of radius $20.5 \mu\text{m}$) is in good agreement with the modified Stokes equation for sedimenting spheres with a finite viscosity [40], see chapter 7.

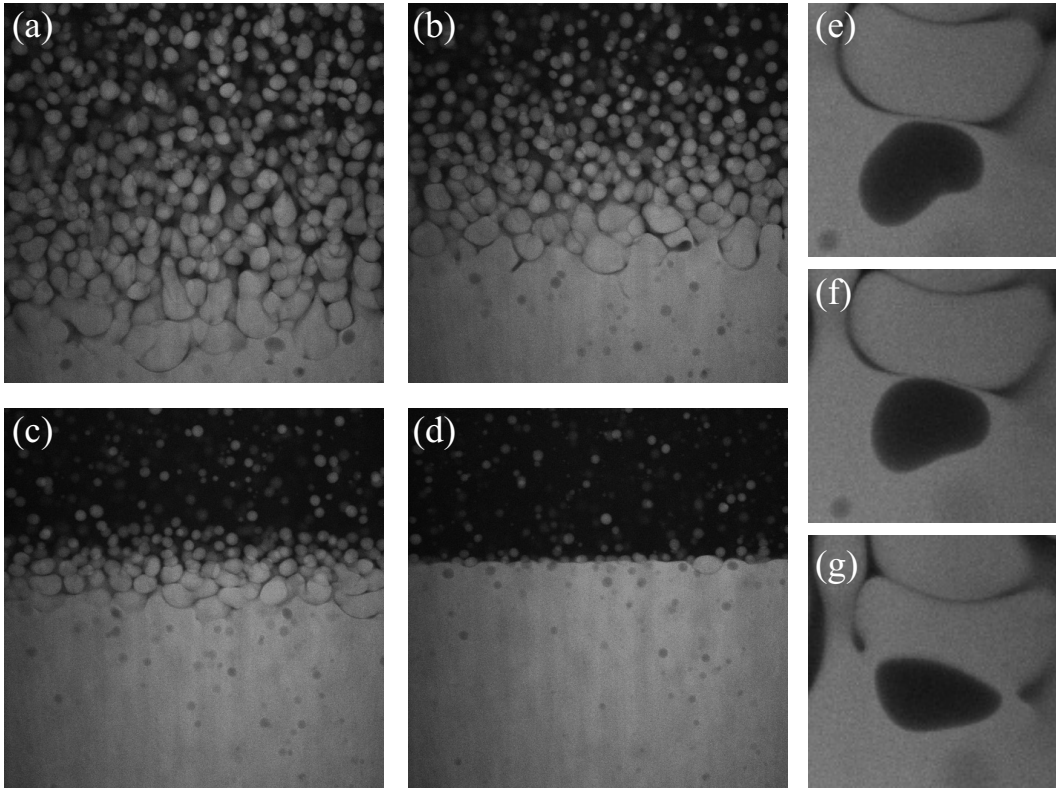


FIGURE 9.4. LSCM-images ($1400 \times 1400 \mu\text{m}^2$) of interface formation in a colloid-polymer mixture taken after 9, 13, 16 and 20 minutes after homogenization (a-d). In (e-g) an example ($171 \times 171 \mu\text{m}^2$) is shown of a coalescence event induced by the gas bubble with (f) 5 s and (g) 15 s after (e).

9.7. CONCLUSION

Simple scaling arguments have been given for the consecutive stages of fluid-fluid phase separation in a colloid-polymer mixture. In principle a different route is expected to be followed than in molecular systems, where the inertial regime is entered before gravity driven flow, although in experiments with molecular fluids the inertial regime has not yet been observed. The scaling arguments make evident that in experiment three successive steps can be observed. In the first step the spinodal pattern coarsened by means of pinch-off events. The preceding linear Cahn-Hilliard regime and the diffusive regime were experimentally not observed. Colloids only have to diffuse over a few times their own particle diameter to reach the viscous regime and this is rapidly so, as can be understood from the diffusion coefficients, which have been measured by the real space FRAP technique. In fact, only in a few systems the linear Cahn-Hilliard regime has been observed, e.g. in polymer-polymer systems [231–233], and the crossover between the diffusive and the viscous regime has been observed for example in [234, 235] for binary fluid mixtures.

By Fourier transforming the LSCM images the characteristic size L was seen to increase linearly with time proportional to γ/η (9.6), the characteristic velocity in the viscous hydrodynamic regime, although the prefactor and the precise definition of η in (9.6) are difficult to estimate given the large number of terms at play and the complexity of the spinodal structure. At typical size $L \sim 2\pi L_c$ the structure collapsed due to gravity reminiscent of the Rayleigh-Taylor instability. There was still some coarsening. The minority phase, the liquid, broke up and became discontinuous for reasons possibly related to the breakup rates of fluid cylinders. Due to the flow the liquid and gas material quickly separated and the interface grew upwards via droplet coalescence. The growth rate was similar to the coarsening rate in the initial stage and the system remained in the viscous hydrodynamic regime. Finally, the use of LSCM leads to clear and well-defined images, especially in comparison to light microscopy where we had observed similar behaviour [106], which only was fully understood after the LSCM experiments on a comparable system had been performed. We hope that the beauty and quality of the images are instructive and might inspire further theoretical development.

APPENDIX: REAL-SPACE FLUORESCENCE RECOVERY AFTER PHOTO-BLEACHING

The diffusion coefficients of colloids in the liquid and gas phase have been determined by real-space fluorescence recovery after photo-bleaching experiments in the following manner. We bleached a cuboid of (x, y) -dimensions $40 \mu\text{m}^2$ and of thickness $\sim 5 \mu\text{m}$ by illuminating the sample with a 405 nm laser. Here, we used a high numerical aperture lens (NA 1.4, 100x) to bleach with sharper edges. The dye incorporated in the particles was easily destroyed. The subsequent recovery of intensity was monitored by using a 488 nm laser. Figure 9.5 shows the bleached cube at time $t = 0 \text{ s}$ (a) and after 28 s (b). We integrated the fluorescent intensities along the four (x, y) sides of the cube, corrected for the objective properties by dividing with the fluorescent intensity far away from the cube, and then normalized the intensity profiles. Averaging in the x direction of figure 9.5(a) gives the profiles along the y direction shown in figure 9.5(c). The other two profiles contain similar information. In [217] Simeonova and Kegel show the details of this technique and derive that the intensity profile along one side at time t can ideally be described by

$$I(x; t) = \frac{1}{2} \left(1 - \operatorname{erf} \left[\frac{x - x_0}{2\sqrt{Dt}} \right] \right), \quad (9.14)$$

with D the diffusion coefficient. In practice, broadening of the profile contained in the square root-term is also caused by the objective properties and we therefore write $\sqrt{Dt + b} = \sqrt{C}$ instead of \sqrt{Dt} with b a constant. The full lines in figure 9.5(c) are the fits to (9.14) with x_0 and C as fitting parameters. By plotting the fitted width C against time, see figure 9.5(d), we obtain from the slopes a diffusion coefficient of $D_L = 4.9 \cdot 10^{-13} \text{ m}^2/\text{s}$ for the liquid (L) phase. The diffusion coefficient of the gas can be measured in a similar way, but since the diffusion is much faster, it is more difficult to measure. In figure 9.5(d) the top two lines correspond to the measured widths for the gas (G) phase followed over a shorter time period. The linear fits give $D_G = 1.9 \cdot 10^{-12} \text{ m}^2/\text{s}$, i.e. 3.7 times faster than diffusion in the liquid phase. The order of magnitude of the diffusion coefficients is in good agreement with the prediction from Stokes-Einstein behaviour. Note that a similar technique can in principle also be used to study diffusion across an interface or in wetting layers.

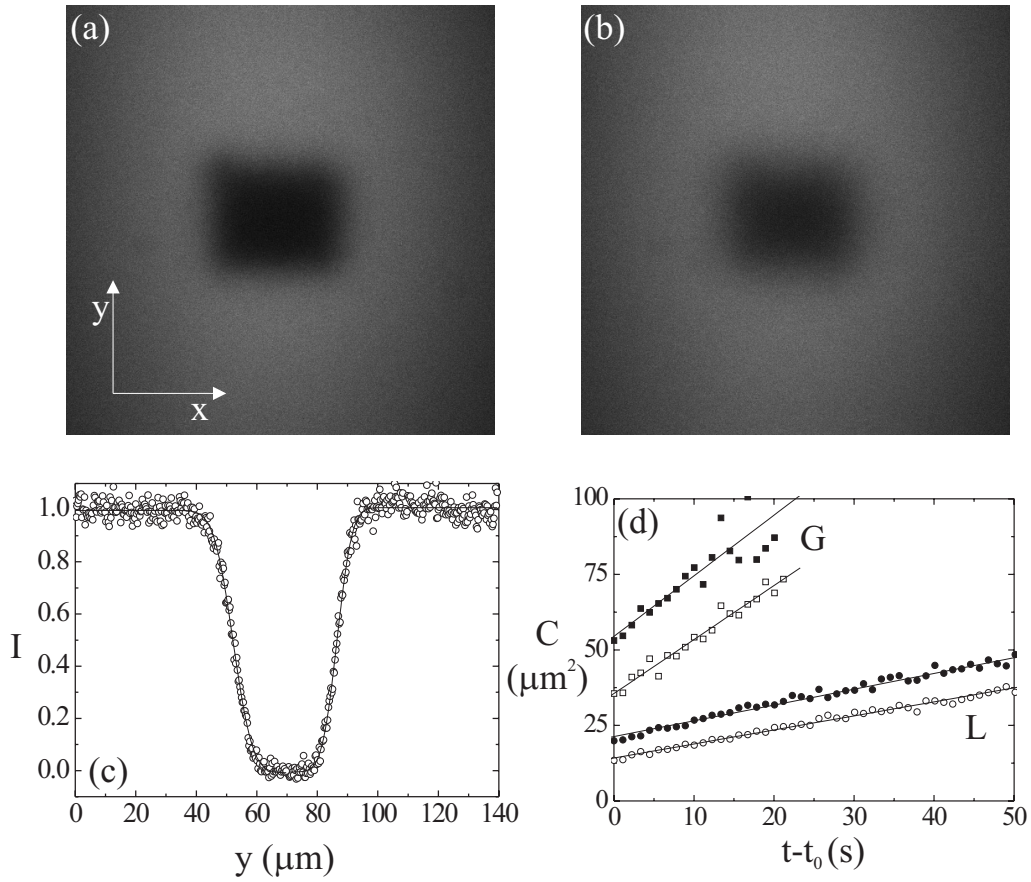


FIGURE 9.5. (a-b) LSCM images ($140 \times 140 \mu\text{m}^2$) of bleached cubes in the liquid phase at $t = 0$ s (a) and $t = 28$ s (b). In (c) the intensity profiles along y of the image in (a) are shown. The line is a fit to (9.14). In (d) the square root of the width of the profile is plotted as a function of time (minus the time t_0 between bleaching and the first recorded image) both for the liquid (circles) and the gas phase (squares) and for the top (filled symbols) and bottom (open symbols) sides. The full line is a linear fit. The slopes of these lines correspond to the diffusion coefficients in liquid and gas phase. The LSCM scans pixel per pixel from left to right and top to bottom, which takes quite some time when bleaching the cube. This explains the offset for the two lines in the same phase, whereas the difference between liquid and gas is a direct consequence of the difference in diffusion coefficients ($D_L < D_G$).

Bibliography

- [1] J.A.C. Valkenburg and C.L. Woldringh. *J. Bact.*, 160:1151, 1984.
- [2] J.D. Bekenstein. *Phys. Rev. D*, 7:2333, 1973.
- [3] J.S. Rowlinson and B. Widom. *Molecular theory of capillarity*. Clarendon Press, Oxford, 1982.
- [4] J.D. van der Waals. *Z. f. Phys. Chem.*, 13:657, 1894.
- [5] B. Widom. *Phys. A*, 263:500, 1999.
- [6] M. V. von Smoluchowski. *Ann. Phys.*, 25:205, 1908.
- [7] L. Mandelstam. *Ann. Phys.*, 41:609–624, 1913.
- [8] F. P. Buff, R. A. Lovett, and F. H. Stillinger. *Phys. Rev. Lett.*, 15:621, 1965.
- [9] J. W. Cahn. *J. Chem. Phys.*, 66:3667, 1977.
- [10] C. Ebner and W.F. Saam. *Phys. Rev. Lett.*, 38:1486, 1977.
- [11] D.R. Lide, editor. *Handbook of chemistry and physics*. Chemical Rubber publishing company, New York, 76 edition, 1995.
- [12] P.G. De Gennes. *Scaling concepts in polymer physics*. Cornell University Press, Ithaca, 1979.
- [13] H. N. W. Lekkerkerker and S. M. Oversteegen. *Physical Chemistry 3: Interfaces (Lecture notes)*. Utrecht, 2001.
- [14] A. Einstein. *Ann. Phys.*, 17:549, 1905.
- [15] J. Perrin. *Ann. de Chim. Phys.*, 18:5, 1908.
- [16] J. Perrin. *Les Atomes*. Libr. Felix Alcan, Paris, 1920.
- [17] W.C.K. Poon. 1998.
- [18] H. N. W. Lekkerkerker, W. C. K. Poon, P. N. Pusey, A. Stroobants, and P. B. Warren. *Europhys. Lett.*, 20:559, 1992.
- [19] A. Vrij. *Pure Appl. Chem.*, 48:471, 1976.
- [20] J. P. Hansen. *J. Phys.*, 46:9, 1985.
- [21] B. V. Derjaguin and L. Landau. *Acta Physicochim. (URSS)*, 14:633, 1941.
- [22] E.J. Verwey and J.Th.G. Overbeek. *Theory of the stability of lyophobic colloids*. Elsevier, Amsterdam, 1948.
- [23] S. Hachisu. *Croatica chemica acta*, 71:975, 1998.
- [24] S. Asakura and F. Oosawa. *J. Chem. Phys.*, 22:1255, 1954.
- [25] S. Asakura and F. Oosawa. *J. Pol. Sci.*, 33:183, 1958.
- [26] W.C.K. Poon. *J. Phys.: Condens. Matter*, 14:R859, 2002.
- [27] A.P. Gast, C.K. Hall, and W.B. Russel. *J. Coll. Int. Sc.*, 96:251, 1983.
- [28] B. Vincent. *Colloids Surf.*, 24:269, 1987.
- [29] B. Vincent, J. Edwards, S. Emmett, and R. Croot. *Colloids and Surfaces*, 31:267–298, 1988.
- [30] H. N. W. Lekkerkerker. *Colloids Surf.*, 51:419, 1990.
- [31] J. M. Brader, R. Evans, and M. Schmidt. *Mol. Phys.*, 101:3349, 2003.
- [32] C.N. Likos. *Phys. Rep.*, 348:267, 2001.
- [33] M. Fuchs and K.S. Schweizer. *J. Phys.: Condens. Matter*, 14:R239, 2002.
- [34] R. Tuinier, J. Rieger, and C.G. de Kruijff. *Adv. Coll. Interf. Sci.*, 103:1, 2003.
- [35] G. A. Vliegthart and H. N. W. Lekkerkerker. *Prog. Colloid Polym. Sci.*, 105:27, 1997.

- [36] E. H. A. de Hoog and H. N. W. Lekkerkerker. *J. Phys. Chem. B*, 103:5274, 1999.
- [37] E. H. A. de Hoog and H. N. W. Lekkerkerker. *J. Phys. Chem. B*, 105:11636, 2001.
- [38] B. H. Chen, B. Payandeh, and M. Robert. *Phys. Rev. E*, 62:2369, 2000.
- [39] G.K. Batchelor. *An introduction to fluid dynamics*. Cambridge University Press, Cambridge, 1967.
- [40] H. Lamb. *Hydrodynamics*. Cambridge University Press, 1932.
- [41] R. F. Probstein. *Physicochemical Hydrodynamics*, section 10.2. John Wiley & Sons, Hoboken, 2003.
- [42] E.M. Purcell. *American J. of Phys.*, 45:3, 1977.
- [43] J. Meunier. Experimental studies of liquids at interfaces: classical methods for studies of surface tension, surface wave propagation and surface thermal modes for studies of viscoelasticity and bending elasticity. In J. Charvolin, J. F. Joanny, and J. Zinn-Justin, editors, *Liquids and Interfaces*, pages 327–369. North-Holland, New York, 1988.
- [44] U. S. Jeng, L. Esibov, L. Crow, and A. Steyerl. *J. Phys.: Condens. Matter*, 10:4955, 1998.
- [45] N.A.M. Verhaegh, J.S. van Duijneveldt, J.K.G. Dhont, and H.N.W. Lekkerkerker. *Physica A*, 230:409, 1996.
- [46] E. H. A. de Hoog, H. N. W. Lekkerkerker, J. Schulz, and G. H. Findenegg. *J. Phys. Chem. B*, 103:10657, 1999.
- [47] E. H. A. de Hoog. *Interfaces and crystallization in colloid-polymer suspensions*. PhD thesis, Utrecht University, 2001.
- [48] P. N. Pusey, A. D. Pirie, and W. C. K. Poon. *Physica A*, 201:322, 1993.
- [49] P. N. Pusey, W. C. K. Poon, S. M. Ilett, and P. Bartlett. *J. Phys.: Condens. Matter*, 6:A29, 1994.
- [50] S. M. Ilett, A. Orrock, W. C. K. Poon, and P. N. Pusey. *Phys. Rev. E*, 51:1344–1352, 1995.
- [51] W. C. K. Poon, A. D. Pirie, and P. N. Pusey. *Faraday Discuss.*, page 65, 1995.
- [52] A. Moussaïd, W. C. K. Poon, P. N. Pusey, and M. F. Soliva. *Phys. Rev. Lett.*, 82:225, 1999.
- [53] K. N. Pham, A. M. Puertas, J. Bergenholtz, S. U. Egelhaaf, A. Moussaïd, P. N. Pusey, A. B. Schofield, M. E. Cates, M. Fuchs, and W. C. K. Poon. *Science*, 296:104, 2002.
- [54] W. C. K. Poon, K. N. Pham, S. U. Egelhaaf, and P. N. Pusey. *J. Phys.: Condens. Matter*, 15:S269, 2003.
- [55] K. N. Pham, S. U. Egelhaaf, P. N. Pusey, and W. C. K. Poon. *Phys. Rev. E*, 69, 2004.
- [56] A. K. Helden, J.W. Jansen, and A. Vrij. *J. Colloid Interface Sci.*, 77:418, 1980.
- [57] B. Vincent. *Colloids Surf.*, 50:241, 1990.
- [58] N. A. M. Verhaegh, D. Asnaghi, H. N. W. Lekkerkerker, M. Giglio, and M. Cipelletti. *Physica A*, 242:104, 1997.
- [59] J. H. van der Wiel. Phase separation and wetting phenomena of a colloid-polymer mixture. Technical report, Debye institute, van 't Hoff laboratory for physical and colloid chemistry, 2002.
- [60] I. Bodnar and W. D. Oosterbaan. *J. Chem. Phys.*, 106:7777, 1997.
- [61] P. Warren. *Langmuir*, 13:4388, 1997.
- [62] R.P. Sear and D. Frenkel. *Phys. Rev. E*, 55:1677, 1997.
- [63] M. Fasolo and P. Sollich. *cond-matt/0411701*, 2004.
- [64] M. Fasolo and P. Sollich. *cond-matt/0410374*, 2004.
- [65] P. Paricaud, S. Varga, P.T. Cummings, and G. Jackson. *Chem. Phys. Lett.*, 398:489, 2004.
- [66] H. N. W. Lekkerkerker and E. H. A. de Hoog. *Physica A*, 298:69, 2001.

- [67] G. Bosma, C. Pathmamanoharan, E. H. A. de Hoog, W. K. Kegel, A. van Blaaderen, and H. N. W. Lekkerkerker. *J. Colloid Interface Sci.*, 245:292, 2002.
- [68] G.C. Berry. *J. Chem. Phys.*, 44:4550, 1966.
- [69] G. Bosma. Dispersion polymerization of fluorescent pmma latex particles. Technical report, Utrecht University, 2001.
- [70] V.C. Martelozzo. *Crystallisation and phase separation in colloidal systems*. PhD thesis, University of Edinburgh, 2001.
- [71] P.N. Pusey and W. van Megen. *Nature*, 320:340, 1986.
- [72] M. Minsky. *Scanning*, 10:128, 1988.
- [73] R. H. Webb. *Rep. Prog. Phys.*, 59:427, 1996.
- [74] T. Wilson. *Confocal Microscopy*. Academic Press Limited, London, 1990.
- [75] R. P. A. Dullens. *Structure and dynamics of colloidal hard spheres in real-space*. PhD thesis, Utrecht University, 2005.
- [76] J.F. Joanny, L. Leibler, and P.G. De Gennes. *J. Polymer Sci.: Polym. Phys.*, 17:1073, 1979.
- [77] P. N. Pusey. *Colloidal Suspensions*. Les Houches: Liquides, Cristallisation et Transition Vitreuse/Liquids, Freezing and Glass Transition. Elsevier, Amsterdam, 1989.
- [78] E. J. Meijer and D. Frenkel. *J. Chem. Phys.*, 100:6873, 1994.
- [79] P. Bolhuis and D. Frenkel. *J. Chem. Phys.*, 101:9869, 1994.
- [80] M. Dijkstra, J. M. Brader, and R. Evans. *J. Phys.: Condens. Matter*, 11:10079, 1999.
- [81] H. N. W. Lekkerkerker and B. Widom. *Physica A*, 285:483, 2000.
- [82] J. M. Brader and R. Evans. *Physica A*, 306:287, 2002.
- [83] S.M. Oversteegen and H. N. W. Lekkerkerker. *Physica A*, 310:181, 2002.
- [84] A. A. Louis, P. G. Bolhuis, J. P. Hansen, and E. J. Meijer. *Phys. Rev. Lett.*, 85:2522, 2000.
- [85] P. G. Bolhuis, A. A. Louis, J. P. Hansen, and E. J. Meijer. *J. Chem. Phys.*, 114:4296–4311, 2001.
- [86] P. G. Bolhuis, A. A. Louis, and J. P. Hansen. *Phys. Rev. E*, 6402:021801, 2001.
- [87] P. G. Bolhuis and A. A. Louis. *Macromolecules*, 35:1860, 2002.
- [88] M. Fuchs and K.S. Schweizer. *J. Phys: Condens. Matter*, 14:R239, 2002.
- [89] T. Taniguchi, T. Kawakatsu, and K. Kawasaki. Slow dynamics in condensed matter. volume 256, page 503. AIP series, 1992.
- [90] E. Eisenriegler, A. Hanke, and S. Dietrich. *Phys. Rev. E*, 54:1134, 1996.
- [91] L. Schäfer. *Excluded Volume Effects in Polymer Solutions*. Springer-Verlag, Heidelberg, 1999.
- [92] A. Hanke, E. Eisenriegler, and S. Dietrich. *Phys. Rev. E*, 59:6853, 1999.
- [93] H. Reiss. *J. Phys. Chem.*, 96:4736, 1992.
- [94] N.F. Carnahan and K.E. Starling. *J. Phys. Chem.*, 51:635, 1969.
- [95] D. Frenkel and A.J.C. Ladd. *J. Chem. Phys.*, 81:3188, 1984.
- [96] S.F. Edwards and K.F. Freed. *J. Phys. A*, 2:145, 1969.
- [97] A.Y. Grosberg and A.R. Khoklov. *Statistical mechanics of macromolecules*. AIP, New York, 1994.
- [98] E. Eisenriegler. *J. Chem. Phys.*, 79:1052, 1983.
- [99] J. Dzubiella, C.N. Likos, and H. Löwen. *J. Chem. Phys.*, 116:9518, 2002.
- [100] J. Dzubiella, C.N. Likos, and H. Löwen. *Europhys. Lett.*, 58:133, 2002.
- [101] S. Ramakrishnan, M. Fuchs, K.S. Schweizer, and C.F. Zukoski. *J. Chem. Phys.*, 116:2201, 2002.
- [102] A. Vrij. *Physica A*, 235:120, 1997.
- [103] J. M. Brader and R. Evans. *Europhys. Lett.*, 49:678, 2000.
- [104] M. Schmidt, H. Löwen, J. M. Brader, and R. Evans. *Phys. Rev. Lett.*, 85:1934, 2000.
- [105] M. Dijkstra and R. van Roij. *Phys. Rev. Lett.*, 89:208303, 2002.

- [106] D. G. A. L. Aarts, J. H. van der Wiel, and H. N. W. Lekkerkerker. *J. Phys.: Condens. Matter*, 15:S245, 2003.
- [107] D. G. A. L. Aarts and H. N. W. Lekkerkerker. *J. Phys.: Condens. Matter*, 16:S4231, 2004.
- [108] W. K. Wijting, N. A. M. Besseling, and M. A. C. Stuart. *Phys. Rev. Lett.*, 90:196101, 2003.
- [109] W. K. Wijting, N. A. M. Besseling, and M. A. C. Stuart. *J. Phys. Chem. B.*, 107:10565–10570, 2003.
- [110] M. Fuchs and K.S. Schweizer. *Europhys. Lett.*, 51:621, 2000.
- [111] D.G.A.L. Aarts, R. Tuinier, and H. N. W. Lekkerkerker. *J. Phys.: Condens. Matter*, 14:7551, 2002.
- [112] M. Schmidt and M. Fuchs. *J. Chem. Phys.*, 117:6308, 2002.
- [113] P. G. Bolhuis, A. A. Louis, and E. J. Meijer. *Phys. Rev. Lett.*, 90:068304, 2003.
- [114] M. Schmidt, A. Fortini, and M. Dijkstra. *J. Phys.: Condens. Matter*, 15:S3411, 2003.
- [115] Y-L. Chen, K.S. Schweizer, and M. Fuchs. *J. Chem. Phys.*, 118:3880, 2003.
- [116] P. Paricaud, S. Varga, and G. Jackson. *J. Chem. Phys.*, 118:8525, 2003.
- [117] H. Nakanishi and M.E. Fischer. *Phys. Rev. Lett.*, 49:1565, 1982.
- [118] D. Bonn and D. Ross. *Rep. Prog. Phys.*, 64:1085–1163, 2001.
- [119] R. Tuinier, H. N. W. Lekkerkerker, and D.G.A.L. Aarts. *Phys. Rev. E*, 65:060801, 2002.
- [120] A. Moncho-Jorda, B. Rotenberg, and A. A. Louis. *J. Chem. Phys.*, 119:12667–12672, 2003.
- [121] A. Moncho-Jorda, J. Dzubiella, J. P. Hansen, and A. A. Louis. *to appear in J. Phys.: Chem. B (2005)*.
- [122] R. L. C. Vink and M. Schmidt. *Cond-matt/0501037*, 2005.
- [123] A. Bellemans. *Physica*, 28:493, 1962.
- [124] J. Fischer. *Mol. Phys.*, 34:1237, 1977.
- [125] D. Bonn, H. Kellay, and J. Meunier. *Phys. Rev. Lett.*, 73:3560, 1994.
- [126] P.P.F. Wessels, M. Schmidt, and H. Löwen. *J. Phys.: Condens. Matter*, 16:L1, 2004.
- [127] P.G. De Gennes. *Rev. Mod. Phys.*, 57:827, 1985.
- [128] S. Dietrich. In C. Comb and J.L. Lebowitz, editors, *Phase transitions and critical phenomena*, volume 12, pages 1–218. Academic, New York, 1988.
- [129] J. M. Brader, R. Evans, M. Schmidt, and H. Löwen. *J. Phys.: Condens. Matter*, 14:L1, 2002.
- [130] D. G. A. L. Aarts, R. P. A. Dullens, H. N. W. Lekkerkerker, D. Bonn, and R. van Roij. *J. Chem. Phys.*, 120:1973, 2004.
- [131] N. Lorén, A. Alstkrär, and A. M. Hermansson. *Macromolecules*, 34:8117, 2001.
- [132] E. Dickinson and P. Walstra. *Food colloids and polymers: stability and mechanical properties*. Royal Society of Chemistry, Cambridge, 1993.
- [133] H. Walter and D.E. Brooks. *FEBS Letters*, 361:135, 1995.
- [134] D. G. A. L. Aarts, M. Schmidt, and H. N. W. Lekkerkerker. *Science*, 304:847, 2004.
- [135] R. L. C. Vink and J. Horbach. *J. Chem. Phys.*, 121:3253, 2004.
- [136] R. L. C. Vink and J. Horbach. *J. Phys.: Condens. Matter*, 16:S3807, 2004.
- [137] B.V. Derjaguin, V.M. Starov, and N.V. Churaev. *Kolloid-Zeitschrift*, 38:875, 1976.
- [138] N.V. Churaev, V.M. Starov, and B.V. Derjaguin. *J. Coll. Int. Sc.*, 89:16, 1982.
- [139] F. Renk, P.C. Wayner, and G.M. Homsy. *J. Coll. Int. Sc.*, 67:408, 1978.
- [140] P. P. F. Wessels, M. Schmidt, and H. Löwen. *J. Phys.: Condens. Matter*, 16:S4169, 2004.
- [141] D. van der Beek, T. Schilling, and H. N. W. Lekkerkerker. *J. Chem. Phys.*, 121:5423, 2004.
- [142] B.V. Derjaguin. *Kolloid-Zeitschrift*, 17:207, 1955.
- [143] J.A. de Feijter and A. Vrij. *J. Electroanal. Chem.*, 37:9, 1972.

- [144] H.T. Dobbs and J.O. Indekeu. *Phys. A*, 201:457, 1993.
- [145] D. Bonn. personal communication, 2003.
- [146] P. Wessels. private communication, 2004.
- [147] A. Vrij. *Adv. Coll. Interf. Sci.*, 2:39–64, 1968.
- [148] M. K. Sanyal, S. K. Sinha, K. G. Huang, and B. M. Ocko. *Phys. Rev. Lett.*, 66:628, 1991.
- [149] M. Tolan, O. H. Seeck, J. P. Schlomka, W. Press, J. Wang, S. K. Sinha, Z. Li, M. H. Rafailovich, and J. Sokolov. *Phys. Rev. Lett.*, 81:2731, 1998.
- [150] A. K. Doerr, M. Tolan, W. Prange, J. P. Schlomka, T. Seydel, W. Press, D. Smilgies, and B. Struth. *Phys. Rev. Lett.*, 83:3470, 1999.
- [151] C. Fradin, A. Braslau, D. Luzet, D. Smilgies, M. Alba, N. Boudet, K. Mecke, and J. Dailant. *Nature*, 403:871, 2000.
- [152] T. Seydel, A. Madsen, M. Tolan, G. Grübel, and W. Press. *Phys. Rev. B*, 6307:073409, 2001.
- [153] K. R. Mecke and S. Dietrich. *Phys. Rev. E*, 59:6766, 1999.
- [154] A. Milchev and K. Binder. *Europhys. Lett.*, 59:81, 2002.
- [155] A. Vrij. *Discussions Faraday Soc.*, 42:23, 1966.
- [156] A. Scheludko. *Adv. Colloid Interface Sci.*, 44:391, 1967.
- [157] K.R. Mecke and S. Dietrich. *preprint*, 2004.
- [158] A.E. Brandes, G.F. Zhang, and J. Vivekanadan. *J. Appl. Meteorology*, 43:461, 2004.
- [159] J.J. Thomson and H.F. Newall. *Proc. R. Soc. London*, 39:417, 1885.
- [160] H.A. Stone, A.D. Stroock, and A. Ajdari. *Annu. Rev. Fluid Mech.*, 36:381, 2004.
- [161] A. H. Brown and C. Hanson. *Nature*, 214:76, 1967.
- [162] S. Hartland. *Can. J. Chem. Eng.*, 47:221, 1969.
- [163] S. Hartland. *Chem. Eng. Sci.*, 24:987, 1969.
- [164] S. Hartland. *Chem. Eng. Sci.*, 24:611, 1969.
- [165] S. Hartland, B. Yang, and S.A.K. Jeelani. *Chem. Eng. Sci.*, 49:1313, 1993.
- [166] A.F. Jones and S.D.R. Wilson. *J. Fluid Mech.*, 87:263, 1978.
- [167] G.V. Jeffreys and J.L. Hawksley. *J. Appl. Chem.*, 12:329, 1962.
- [168] N. Chen, T. Kuhl, R. Tadmor, Q. Lin, and J.N. Israelachvili. *Phys. Rev. Lett.*, 92:024501, 2004.
- [169] J. Eggers, J. R. Lister, and H. A. Stone. *J. Fluid Mech.*, 401:293, 1999.
- [170] L. Duchemin, J. Eggers, and C. Jossierand. *J. Fluid Mech.*, 487:167, 2003.
- [171] W. Yao, J.H. Maris, P. Pennington, and G.M. Seidel. *Phys. Rev. E*, 71:016309, 2005.
- [172] A. Menchaca-Rocha, A. Martínez-Dávalos, R. Núñez, S. Popinet, and S. Zaleski. *Phys. Rev. E*, 63:046309, 2001.
- [173] M. Wu, T. Cubaud, and C. Ho. *Phys. Rev. E*, 16:L51, 2004.
- [174] H.A. Stone. *Ann. Rev. Fluid Mech.*, 26:65, 1994.
- [175] J. Happel and H. Brenner. *Low Reynolds number hydrodynamics*. Martinus Nijhoff Publishers, Dordrecht, 1986.
- [176] O. Reynolds. *Philos. Trans. R. Soc. London*, 177:157, 1886.
- [177] G. E. Charles and S.G. Mason. *J. Coll. Sc.*, 15:236, 1960.
- [178] S. Hartland. *J. Coll. Int. Sc.*, 26:383, 1968.
- [179] S.G. Yiantsios and R.H. Davis. *J. Fluid Mech.*, 217:547, 1990.
- [180] H.M. Princen and S.G. Mason. *J. Coll. Sc.*, 20:246, 1965.
- [181] M. von Smoluchowski. *Phys. Zeitschrift*, 17:537, 1916.
- [182] R. Becker. *Theorie der Wärme*. Springer-Verlag, Berlin, 1966.
- [183] H.J. Schulze, K.W. Stöckelhuber, and A. Wenger. *Coll. Surf. A*, 192:61, 2001.

- [184] D. G. A. L. Aarts, H. N. W. Lekkerkerker, Tracy, G. Wegdam, and D. Bonn. *submitted to Phys. Rev. Lett.*, 2005.
- [185] J. Eggers. *Rev. Mod. Phys.*, 69:865, 1997.
- [186] J. Keller and M. Miksis. *SIAM J. Appl. Math.*, 43:268, 1983.
- [187] J. Keller and M. Miksis. *J. Fluid Mech.*, 232:191, 1991.
- [188] D.H. Peregrine, G. Shoker, and A. Symon. *J. Fluid Mech.*, 212:25, 1990.
- [189] I. Cohen, M.P. Brenner, J. Eggers, and S.R. Nagel. *Phys. Rev. Lett.*, 83:1147, 1999.
- [190] J. Eggers. *Phys. Rev. Lett.*, 71:3458, 1993.
- [191] P. Doshi, I. Cohen, W.W. Zhang, M. Siegel, P. Howell, O.A. Basaran, and S.R. Nagel. *Science*, 302:1185, 2003.
- [192] M. Moseler and U. Landman. *Science*, 289:1165, 2000.
- [193] J. Eggers. *Phys. Rev. Lett.*, 89:084502, 2002.
- [194] J. Eggers and T.F. Dupont. *J. Fluid Mech.*, 262:205, 1994.
- [195] R.F. Day, E.J. Hinch, and J.R. Lister. *Phys. Rev. Lett.*, 80:704, 1998.
- [196] D. Leppinen and J.R. Lister. *Phys. Fluids*, 15:568, 2003.
- [197] J. R. Lister and H. A. Stone. *Phys. Fluids*, 10:2758, 1998.
- [198] G. H. Koenderink, D. G. A. L. Aarts, V. W. A. de Villeneuve, A. P. Philipse, R. Tuinier, and H. N. W. Lekkerkerker. *Biomacr.*, 4:129, 2003.
- [199] Interactive data language, research systems, inc. (<http://www.rsinc.com>).
- [200] A. Rothert, R. Richter, and R. Rehberg. *Phys. Rev. Lett.*, 87:084501, 2001.
- [201] D.T. Papageorgiou. *Phys. Fluids*, 7:1529, 1995.
- [202] J. Eggers. personal communication, 2005.
- [203] A. Onuki. *Phase transition dynamics*. Cambridge University Press, Cambridge, 2002.
- [204] K. Binder. Spinodal decomposition. In *Phase transformations in materials*, volume 5, pages 405–471. VCH Verlagsgesellschaft Weinheim, 1990.
- [205] N. A. M. Verhaegh and H. N. W. Lekkerkerker. Phase transitions in colloidal suspensions. In F. Mallamace and H.E. Stanley, editors, *The physics of complex systems, International School of Physics, "Enrico Fermi", Course CXXXIV*, page 347. IOS Press, 1997.
- [206] J. W. Cahn and J. E. Hilliard. *J. Chem. Phys.*, 28:258, 1958.
- [207] J. W. Cahn and J. E. Hilliard. *J. Chem. Phys.*, 31:688, 1959.
- [208] J. W. Cahn. *Acta Met.*, 9:795, 1961.
- [209] J. W. Cahn. *J. Chem. Phys.*, 42:93, 1965.
- [210] J. K. G. Dhont. *An introduction to dynamics of colloids*. Elsevier, Amsterdam, 1996.
- [211] E. D. Siggia. *Phys. Rev. A*, 20:595–605, 1979.
- [212] A. J. Bray. Coarsening dynamics of nonequilibrium phase transitions. In M. E. Cates and M. R. Evans, editors, *Soft and Fragile Matter: Nonequilibrium Dynamics, Metastability and Flow*. SUSSP Publications, Institute of Physics Publishing, Edinburgh, 2000.
- [213] V. M. Kendon, M. E. Cates, I. Pagonabarraga, J-C Desplat, and P. Bladon. *J Fluid Mech.*, 440:147, 2001.
- [214] V. M. Kendon, J-C Desplat, P. Bladon, and M. E. Cates. *Phys. Rev. Lett.*, 83:576, 1999.
- [215] H. Furukawa. *Phys. Rev. A*, 31:1103, 1985.
- [216] I. Pagonabarraga, J-C Desplat, A. J. Wagner, and M. E. Cates. *New J. Phys.*, 3:9.1, 2001.
- [217] N. Simeonova and W. K. Kegel. *Faraday Discuss.*, 123:27, 2003.
- [218] T. Hashimoto, T. Koga, H. Jinnai, and Y. Nishikawa. *Il nuovo cimento*, 20:1947, 1998.
- [219] P. Guenon, R. Gastaud, F. Perrot, and D. Beysens. *Physica A*, 36:4876, 1987.

- [220] K. Binder and D. Stauffer. *Phys. Rev. Lett.*, 33:1006, 1974.
- [221] Y. C. Chou and W. L. Goldberg. *Phys. Rev. A*, 23:858, 1981.
- [222] R. H. Tromp, A. R. Rennie, and R. A. L. Jones. *Macromolecules*, 28:4129, 1995.
- [223] J. L. Lebowitz, J. Marro, and M. H. Kalos. *Acta Met.*, 30:297, 1982.
- [224] H. Furukawa. *Physica A*, 123:497, 1984.
- [225] S. Tomotika. *Proc. R. Soc. Ser. A*, 150:322, 1935.
- [226] S. Chandrasekhar. *Hydrodynamic and hydromagnetic stability*. Dover, New York, 1981.
- [227] D. G. A. L. Aarts. *Faraday Discuss.*, 123:General discussion: 174, 2003.
- [228] A. Wysocki and H. Löwen. *J. Phys.: Condens. Matter*, 16:7209, 2004.
- [229] T. Hashimoto, K. Matsuzaka, E. Moses, and A. Onuki. *Phys. Rev. Lett.*, 74:126–129, 1995.
- [230] K. Matsuzaka, T. Koga, and T. Hashimoto. *Phys. Rev. Lett.*, 80:5441–5444, 1998.
- [231] T. Izumitani and T. Hashimoto. *J. Chem. Phys.*, 83:3694, 1985.
- [232] M. Okada and C. C. Han. *J. Chem. Phys.*, 85:5317, 1986.
- [233] F. S. Bates and P. Wiltzius. *J. Chem. Phys.*, 91:3258, 1989.
- [234] M. W. Kim, A. J. Schwartz, and W. L. Goldberg. *Phys. Rev. Lett.*, 41:657, 1978.
- [235] Y. C. Chou and W. I. Goldberg. *Phys. Rev. A*, 20:2105, 1979.

Summary

This thesis reports on a study of the behaviour and properties of interfaces with an ultralow interfacial tension. In the first chapter it is explained that an ultralow interfacial tension has several important consequences both for the statics and dynamics of interfaces; some lengthscales increase, whereas others decrease. At the same time the system becomes intrinsically slow and it is concluded that for the dynamics life at ultralow interfacial tension is similar to life at low Reynolds number. The above makes the study relevant from a fundamental point of view. The experimental systems are colloid-polymer mixtures, which are also used for example in the food industry. Similar mixtures are present in the living cell as well. This gives the present study industrial as well as biological relevance.

In chapter 2 the model colloid-polymer mixtures are introduced, i.e. a silica colloid + poly(dimethylsiloxane) mixture in cyclohexane and two different poly(methylmethacrylate) + poly(styrene) mixtures in decalin. Furthermore, the experimental setup is described, which consists of a horizontally placed microscope used either in the transmission or in the laser scanning confocal mode. It turns out that the techniques as well as the mixtures are complementary.

The observations of the phase behaviour of the first experimental system inspired the theory presented in chapter 3. Here, we extend the free volume theory for mixtures of hard sphere colloids and ideal polymers to include curvature effects and polymer-polymer interactions. As a result more polymer is needed to induce gas-liquid phase separation. In addition, the fluid-crystal coexistence region becomes more pronounced. The experimental binodals lie between the ideal and the interacting polymer theory.

The theoretical model of chapter 3 is extended further to calculate the interfacial tension and the wetting behaviour (chapter 4). The interacting polymer model lowers the gas-liquid interfacial tension and predicts the wetting transition to occur at higher polymer concentrations as compared to the ideal polymer model. These predictions are compared to experiment in the next chapter.

In chapter 5 we experimentally study the gas-liquid interface in the vicinity of a vertical hard wall. The interfacial profile is accurately described by the interplay between the Laplace and the hydrostatic pressure. From this description the capillary length is obtained, which is at most tens of microns. The magnitude of the capillary length is compared to theory, where qualitative agreement is found. Determining the wetting state of the system turns out to be a subtle experimental task, but once the location of

the wall is accurately determined, the contact angle is found as well. It turns out that the system shows complete wetting for all statepoints measured.

In chapter 6 we show how to tune length- and timescales, by using colloidal suspensions, in such a way that the fluctuating fluid-fluid interface can be seen directly in real space with a resolution close to the particle size. Experimental results for static and dynamic correlation functions validate the capillary wave model down to almost the particle level. We are able to obtain the ultra-low interfacial tension, the capillary length and the capillary time, which are found to be in agreement with independent measurements.

It turns out that capillary waves play a crucial role in droplet coalescence (chapter 7). The coalescence is a three step process: (i) drainage of the continuous film between droplet and bulk phase, (ii) breakup of the film, and (iii) the growth of the connection. We observe that drainage becomes very slow and eventually the breakup of the film is induced by thermal capillary waves. The waiting time for a certain height fluctuation is an important parameter for the kinetics of the process and can be directly obtained from experiment. Van der Waals forces need not be invoked. During the third stage we observe that the radius of the connecting neck grows linearly with time both for gas bubbles and liquid droplets with an order of magnitude that is in good agreement with the capillary velocity.

The thermal roughness is also believed to be important in droplet snap-off processes. In chapter 8 we study the possibility of observing a regime where thermal noise dominates over interfacial tension. To this end we study a colloid-polymer mixture with a relatively high and a mixture with a relatively low interfacial tension. In the first system the shape of the neck at snap-off, the number of satellite drops, and the radius of the neck as a function of time are all in agreement with the situation that the interfacial tension is dominant. In the second system the symmetry and appearance at snap-off does suggest that thermal noise becomes dominant.

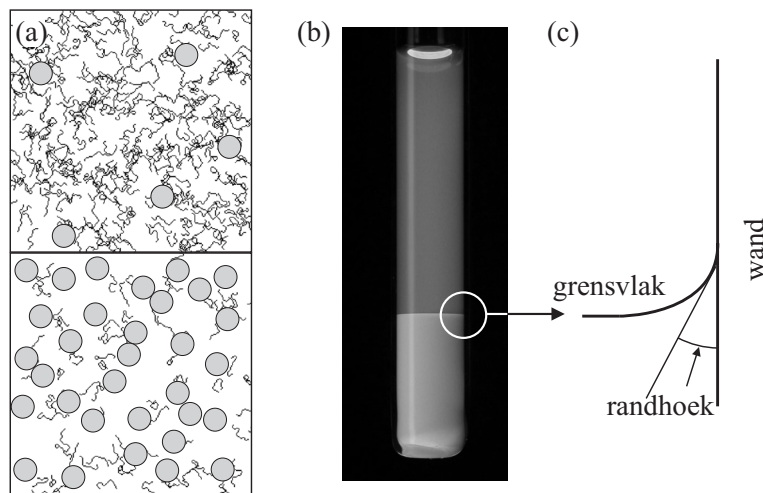
In the final chapter, chapter 9, we are able to follow the phase separation process in great detail due to the ultralow interfacial tension. Simple scaling arguments are given why in experiment three steps of the phase separation can be observed: an interfacial tension driven coarsening, gravity driven flow, and finally the interface formation. All these stages can be observed in a single experiment. The first stage can be quantitatively described by viscous hydrodynamics. Coarsening occurs through pinch-off events. The second stage begins at a typical size of 2π times the capillary length reminiscent of the Rayleigh-Taylor instability. The liquid phase breaks up and becomes discontinuous. There is strong directional flow in the system. Finally, the macroscopic interface is formed growing upwards with a velocity comparable to the coarsening velocity in the initial stage. Again, viscous hydrodynamics apply with a characteristic velocity of the interfacial tension over the viscosity.

Samenvatting voor iedereen

Oppervlakken ofwel grensvlakken zijn overal aanwezig en spelen een belangrijke rol op grote en kleine schaal. Ieder oppervlak heeft een bepaalde spanning, die oppervlakte- of grensvlakspanning wordt genoemd. Deze grensvlakspanning is microscopisch gezien het gevolg van krachten tussen moleculen, maar uit zich macroscopisch op vele manieren. Zo kunnen door de grensvlakspanning sommige insecten zoals schaatsenrijdertjes over water lopen, zijn druppels rond en staat het water-oppervlak gekromd aan een glaswand. De relatie tussen interacties op een microscopische schaal, maar verschijnselen op een macroscopische schaal heeft vele beroemde mensen uit de wetenschap aangesproken, waaronder de Nederlander Johannes Diderik van der Waals, die in 1892 voor het eerst een sluitende theoretische beschrijving van het gas-vloeistof grensvlak gaf. In dit proefschrift zijn we vanuit een fundamenteel oogpunt verder op deze relatie ingegaan door systemen te bestuderen met een zeer lage grensvlakspanning.

Een echt lage grensvlakspanning kan op verschillende manieren worden gerealiseerd, maar de beste manier is door gebruik te maken van een modelsysteem van het gas-vloeistof grensvlak. Dit modelsysteem bestaat uit een mengsel van kleine bollen en lange ketens in een oplosmiddel. De bolletjes zijn dusdanig klein dat ze niet zomaar naar beneden zinken, maar onder invloed van de temperatuur voortdurend in beweging zijn (de Brownse beweging). Ze worden colloïden genoemd en zijn een miljoen keer kleiner dan een centimeter. De ketens zijn zo dun als de oplosmiddel-moleculen, maar zo lang als de colloïden groot zijn. Ze vormen in het oplosmiddel een soort zeer open kluwen wol en worden polymeer genoemd. Dit colloïd-polymeer mengsel is schematisch weergegeven in figuur 1. Wanneer de concentraties van zowel colloïden als polymeren hoog genoeg zijn, zal het systeem zich spontaan scheiden in een fase rijk aan colloïden, maar arm aan polymeren, en een fase arm aan colloïden, maar rijk aan polymeren. Deze colloïd-rijke fase lijkt in zekere zin op een vloeistof, terwijl de colloïd-arme fase op een gas lijkt. Deze mengsels worden ook veel gebruikt in de voedingsmiddelen-industrie. Bovendien komen in de (menselijke) cel soortgelijke deeltjes voor. Dit geeft het onderzoek naast een fundamentele, ook een industriële en biologische relevantie.

In het onderzoek beschreven in dit proefschrift hebben we gebruik gemaakt van verschillende colloïd-polymeer mengsels. Hun karakteristieke eigenschappen staan beschreven in hoofdstuk 2. Daarbij is de grootte van de colloïden belangrijk, aangezien dit de

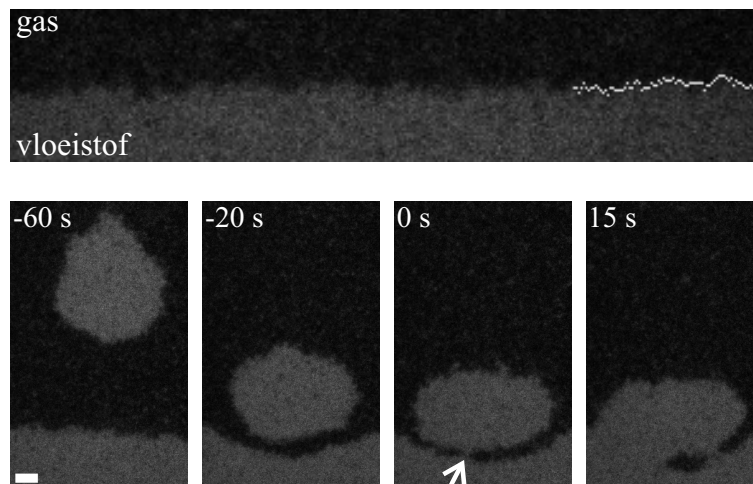


Figuur 1. (a) Schematische weergave van een fasegescheiden colloïd-polymeer mengsel. De bovenste fase lijkt op een gas van colloïden, terwijl de onderste fase op een vloeistof van colloïden lijkt. In (b) is een foto te zien van een fasegescheiden colloïd-polymeer mengsel. Als we op het grensvlak van (b) inzoomen, verwachten we dat dit grensvlak vlakbij de wand omhoog komt, zoals schematisch weergegeven is in (c). Dit is in ons onderzoek ook aangetoond (hoofdstuk 5), waarbij de randhoek overigens voortdurend 0° blijkt te zijn.

grensvlakspanning bepaalt. Vervolgens is het grensvlak bestudeerd met zowel licht microscopie als confocale microscopie. De laatste is een moderne microscopie techniek, waarbij veel nauwkeuriger kan worden gekeken.

Alvorens het grensvlak daadwerkelijk te bestuderen, wilden we eerst vanuit een theoretisch oogpunt het fasegedrag beter begrijpen. In een bekend theoretisch model voor de fasescheiding wordt het polymeer zeer eenvoudig beschreven en in hoofdstuk 3 hebben we dit model uitgebreid en het polymeer realistischer beschreven. Een belangrijk gevolg hiervan is dat er in de realistischere polymeer-beschrijving meer polymeer nodig is om het systeem te doen ontmengen. Het blijkt dat het experiment vaak tussen het eenvoudige en het verbeterde model in ligt, wat aangeeft dat het kwantitatief beschrijven van het fasegedrag zeer lastig is.

Vervolgens hebben we dit model verder uitgebreid om ook de grensvlakspanning te kunnen berekenen. Dit is gedaan in hoofdstuk 4. Daarbij hebben we gebruik gemaakt van de Van der Waals-theorie. Het blijkt dat de grensvlakspanning lager is, wanneer het polymeer realistischer wordt beschreven. Bovendien hebben we ook de randhoek berekend, die het gas-vloeistof grensvlak met een harde wand maakt, zoals aangegeven in figuur 1 (c). Vanaf een bepaalde concentratie aan polymeer blijkt dat de randhoek niet langer 0° is, wat volledige bevochtiging wordt genoemd, maar groter dan 0° wordt, wat gedeeltelijke bevochtiging wordt genoemd. Deze overgang vindt bij hogere polymeer-concentraties plaats, wanneer het polymeer realistischer wordt beschreven.



Figuur 2. Bovenste rij: De golvende ruwheid van een grensvlak waargenomen met een krachtige microscoop. Het beeld is slechts $17.5 \mu\text{m}$ bij $80 \mu\text{m}$. Onderste rij: Een colloïdale vloeistof druppel, die samenvloeit met de bulk vloeistof fase. De schaalbar is $5 \mu\text{m}$. De druppel is $22 \mu\text{m}$ groot. De drie opeenvolgende stappen van samenvloeien zijn duidelijk te zien. De eerste connectie die wordt gemaakt is erg dun (aangegeven door het pijltje). Er worden zelfs twee verbindingen gemaakt, wat ervoor zorgt dat gasfase wordt “ingevangen”.

In hoofdstuk 5 zijn de eerste experimenten beschreven. Daartoe zijn verschillende colloïd-polymeer mengsels vlakbij een wand bestudeerd (figuur 1) met de twee microscopie technieken. Het blijkt dat de kromming van het grensvlak van het gas-vloeistof systeem bepaald wordt door een balans tussen twee verschillende krachten, namelijk de zwaartekracht en de kracht ten gevolge van de grensvlakspanning. Door hier gebruik van te maken kan een karakteristieke lengte worden bepaald, die de capillaire lengte wordt genoemd, zelfs al is deze lengte duizend keer kleiner dan in systemen met een hoge grensvlakspanning. Bovendien blijkt dat het systeem altijd volledig bevochtigend is, in tegenspraak met de theoretische modellen, wat aangeeft dat de theorie nog verder ontwikkeld moet worden.

Vervolgens is het vrije grensvlak bestudeerd in hoofdstuk 6. Het is al lang bekend dat de temperatuur, die de colloïden in beweging houdt, ook het grensvlak laat bewegen. Dit wordt echter tegengegaan door de grensvlakspanning. Aangezien de grensvlakspanning in normale (moleculaire) systemen relatief groot is, zorgt dit ervoor dat de thermische beweging van het grensvlak extreem klein is en zelfs niet met behulp van een microscoop kan worden waargenomen. Aangezien in ons systeem de grensvlakspanning echter heel klein kan worden, wordt de beweging van het grensvlak door de temperatuur toch aanzienlijk en blijkt dat de dynamische ruwheid inderdaad direct kan worden waargenomen. De ruwheid wordt opgebouwd uit zogenaamde capillaire golven. Dit is

te zien in figuur 2. Het blijkt hierbij dat ons beeld van zo'n ruw grensvlak verrassend goed werkt.

Zoals te zien is in figuur 2 speelt de golvende ruwheid van het grensvlak ook een belangrijke rol in de druppel-coalescentie (hoofdstuk 7). Het proces van druppel-coalescentie verloopt in drie stappen. In de eerste stap stroomt het laagje gas tussen druppel en bulk fase weg, in de tweede stap ontstaat er een verbinding tussen druppel en bulk vloeistof en in de derde stap wordt de druppel in de vloeistof uitgeknepen. In moleculaire vloeistoffen is de tweede stap ongrijpbaar gezien de kleine fluctuaties, maar het derde plaatje in de onderste rij van figuur 2 laat nu voor het eerst duidelijk zien dat er een zeer dunne verbinding wordt gemaakt tussen twee elkaar toevallig ontmoetende golfjes. In het vierde plaatje is goed te zien dat de verbinding gegroeid is. Het blijkt in dit geval dat de groei lineair gaat met de tijd. Dit lineaire regime is zeer lastig te meten in moleculaire vloeistoffen, maar kan hier dankzij de ultralage grensvlakspanning goed worden bestudeerd.

Het blijkt dat de ruwheid van het grensvlak ook een belangrijke rol speelt in het opbreken van druppels, het tegenovergestelde proces van de druppel-coalescentie. Dit wordt beschreven in hoofdstuk 8. Hierin is te zien dat wanneer de grensvlakspanning laag genoeg is, het opbreken zich anders manifesteert. Dit is nu voor het eerst kwalitatief waargenomen in het experiment, maar de kwantitatieve analyse laat vooralsnog op zich wachten.

Dit proefschrift besluit met een beschrijving van de daadwerkelijke ontmenging in hoofdstuk 9. In dit ontmeng-proces zijn zowel de vorming als de coalescentie van druppels heel belangrijk. Opnieuw blijkt dat alles in detail kan worden bestudeerd dankzij de lage grensvlakspanning. Het blijkt dat de krachtenbalans die de snelheden bepaalt in de druppelcoalescentie en druppelvorming, ook de snelheid bepaalt in de vorming van de ontmengende structuren. Bovendien valt het gehele proces met behulp van een zeer beperkt aantal vloeistof-eigenschappen goed te beschrijven.

List of publications

This thesis is based on the following publications:

- D. G. A. L. Aarts, R. Tuinier and H. N. W. Lekkerkerker, *Phase behaviour of mixtures of colloidal spheres and excluded-volume polymer chains*, J. Phys.: Condens. Matt. **14**, 7551 (2002). (chapter 3)
- D. G. A. L. Aarts, J. H. van der Wiel and H. N. W. Lekkerkerker, *Interfacial dynamics and the static profile near a single wall in a model colloid-polymer mixture*, J. Phys.: Condens. Matt. **15**, S245 (2003). (chapter 5)
- D. G. A. L. Aarts, R. P. A. Dullens, D. Bonn, R. van Roij and H. N. W. Lekkerkerker, *Interfacial tension and wetting in colloid-polymer mixtures*, J. Chem. Phys. **120**, 1973 (2004). (chapter 4)
- D. G. A. L. Aarts and H. N. W. Lekkerkerker, *Confocal scanning laser microscopy on fluid-fluid demixing colloid-polymer mixtures*, J. Phys.: Condens. Matt. **16**, S4231 (2004). (chapters 5 and 9)
- D. G. A. L. Aarts, M. Schmidt, and H. N. W. Lekkerkerker, *Direct visual observation of thermal capillary waves*, Science **304**, 847 (2004). (chapter 6)
- D. G. A. L. Aarts, M. Schmidt, and H. N. W. Lekkerkerker, *Frontlinie Artikel: Directe visuele waarneming van thermische capillaire golven*, Nederlands tijdschrift voor Natuurkunde **70**, 216 (2004). (chapter 6)
- D. G. A. L. Aarts, R. P. A. Dullens and H. N. W. Lekkerkerker, *Interfacial dynamics in demixing systems with ultralow interfacial tension*, New. J. Phys. **7**, 40 (2005). (chapter 9)
- D. G. A. L. Aarts, *The capillary length in a fluid-fluid demixed colloid-polymer mixture*, accepted for publication in J. Phys. Chem. B (chapter 5)
- D. G. A. L. Aarts, M. Schmidt, K. Mecke and H. N. W. Lekkerkerker, *Microscopy on thermal capillary waves in demixed colloid-polymer systems*, accepted for publication in Adv. Solid State Phys. (chapter 6)
- D. G. A. L. Aarts, H. N. W. Lekkerkerker, H. Guo, G. H. Wegdam and D. Bonn *Hydrodynamics of droplet coalescence*, submitted to Phys. Rev. Lett. (chapter 7)
- D. G. A. L. Aarts, Y. Hennequin, J. H. van der Wiel, D. Bonn, G. H. Wegdam, J. Eggers and H. N. W. Lekkerkerker, *Droplet snap-off affected by thermal noise*, in preparation (chapter 8)

Other papers by the author:

- A. V. Petukhov, D. G. A. L. Aarts, I. P. Dolbnya, E. H. A. de Hoog, K. Kassapidou, G. J. Vroege, W. Bras and H. N. W. Lekkerkerker, *High-Resolution Small-Angle X-Ray Diffraction Study of Long-Range Order in Hard-Sphere Colloidal Crystals*, Phys. Rev. Lett. **88**, 208301 (2002)
- R. Tuinier, H. N. W. Lekkerkerker, and D. G. A. L. Aarts, *Interaction potential between two spheres mediated by excluded volume polymers*, Phys. Rev. E **65**, 060801(R) (2002)
- G. H. Koenderink, H. Zhang, D. G. A. L. Aarts, M. P. Lettinga, A. P. Philipse and G. Nägele, *On the validity of Stokes-Einstein-Debye relations for rotational diffusion in colloidal suspensions*, Faraday Discuss., 335 (2003)
- G. H. Koenderink, D. G. A. L. Aarts, V. W. A. de Villeneuve, A. P. Philipse, R. Tuinier, and H. N. W. Lekkerkerker, *Morphology and kinetics of phase separating transparent xanthan-colloid mixtures*, Biomacromolecules **4**, 129(2003)
- A. V. Petukhov, I. P. Dolbnya, D. G. A. L. Aarts, G. J. Vroege, and H. N. W. Lekkerkerker, *Bragg rods and multiple x-ray scattering in random-stacking colloidal crystals*, Phys. Rev. Lett. **90**, 028304 (2003)
- X. Xian, A. V. Petukhov, M. M. M. E. Snel, I. P. Dolbnya, D. G. A. L. Aarts, G. J. Vroege and H. N. W. Lekkerkerker, *High-quality colloidal crystals at a wall characterised by small angle x-ray diffraction*, J. Appl. Cryst. **36**, 597 (2003)
- G. H. Koenderink, D. G. A. L. Aarts, and A. P. Philipse, *Rotational dynamics of colloidal tracer spheres in suspensions of charged rigid rods*, J. Chem. Phys. **119**, 4490 (2003)
- R. Tuinier, D. G. A. L. Aarts, H. H. Wensink and H. N. W. Lekkerkerker, *Pair interaction and phase separation in mixtures of colloids and excluded volume polymers*, Phys. Chem. Chem. Phys. **5**, 3707 (2003)
- G. H. Koenderink, S. Sacanna, D. G. A. L. Aarts, and A. P. Philipse, *Rotational and translational diffusion of fluorocarbon tracer spheres in semidilute xanthan solutions*, Phys. Rev. E **69**, 021804 (2004)
- A. V. Petukhov, I. P. Dolbnya, D. G. A. L. Aarts, and G. J. Vroege, *Destruction of long-range order recorded with in-situ small-angle x-ray diffraction in drying colloidal crystals*, Phys. Rev. E **69**, 031405 (2004)
- R. P. A. Dullens, M. C. D. Mourad, D. G. A. L. Aarts, J. P. Hoogenboom, and W. K. Kegel, *Shape-induced frustration of hexagonal order in polyhedral colloids*, submitted
- I. P. Dolbnya, A. V. Petukhov, D. G. A. L. Aarts, G. J. Vroege, and H. N. W. Lekkerkerker, *Coexistence of rhcp and fcc phases in hard-sphere colloidal crystals*, submitted
- R. P. A. Dullens, D. G. A. L. Aarts, and W. K. Kegel, *Direct measurement of the free energy by optical microscopy*, submitted

Dankwoord

In dit dankwoord wil ik graag een aantal mensen bedanken die direct of indirect hebben bijgedragen aan de totstandkoming van dit proefschrift.

Ten eerste wil ik mijn promotor Henk Lekkerkerker bedanken. Henk, jouw stimulerende en enthousiasmerende manier van werken heeft mij zeer aangesproken. Ik heb veel van je geleerd. Je kennis van de oude literatuur is verbluffend te noemen. Aan de worstelingen met $9/280 \pi^2$ heb ik prettige herinneringen overgehouden en het bleek geen “dood getal in lege som alleen”. Bovendien heb ik geleerd hoe belangrijk het is om voortdurend ordes van grootte af te schatten. Ook waardeer ik dat je als geen ander het belang van het experiment inziet.

Verder wil ik graag mijn kamergenoten Roel Dullens en Martijn Oversteegen bedanken, als N701 vormden wij een waar blok tegen de dagelijkse beslommeringen. Roel, alleen met jou kan ik tegelijkertijd met de confocal werken, waarbij we letterlijk vier handen hebben. De vele discussies die we overal ter wereld hebben gevoerd, hebben reeds tot meerdere publicaties geleid en er zullen er nog vele volgen. Martijn, ik kijk met plezier terug op de AO-vergelijking betreffende de (μ, T) -raadselen en onze vele etymologische discussies. Hopelijk drinken we met z'n drieën in de verdere toekomst nog regelmatig een cassis/bier samen. Voordat Roel kamergenoot werd, was Valerie Anderson daar. Valerie, thank you for lending your ear once in a while. Ook wil ik Willem Kegel bedanken. Het is goed te weten dat je altijd tijd hebt om naar nieuwe ideeën te luisteren. Je creativiteit is een voorbeeld.

Gedurende mijn promotie heb ik het geluk gehad om met verschillende, zeer intelligente mensen te mogen discussiëren en samenwerken (naast bovengenoemde mensen, natuurlijk!). Daarbij wil ik ten eerste Remco Tuinier en René van Roij bedanken van wie ik in het begin van mijn promotie veel geleerd heb over de theorie van colloïd-polymeer mengsels en zonder wie hoofdstukken 3 en 4 nooit zouden zijn gelukt. Furthermore, I thank Bob Evans for teaching me a great deal on theory, theorists and Derjaguin. Vervolgens wil ik Matthias Schmidt bedanken. Matthias, zonder jou zou het werk beschreven in hoofdstuk 6 absoluut onmogelijk zijn geweest, maar ook aan de andere hoofdstukken heb je heel veel bijgedragen. Ik waardeer je manier van samenwerken zeer. Het capillaire golf telefoontje staat ook in mijn geheugen gegrift. Furthermore, I have had stimulating discussions with Klaus Mecke about capillary waves. Especially the angle distributions in chapter 6 are reflecting his profound ideas about the gas-liquid interface. Verder heb ik gedurende mijn hele promotie veel leuke en nuttige discussies

met Daniel Bonn gehad, over zowel de bevochtiging als de coalescentie en vorming van druppels. Ongetwijfeld zullen er in Parijs nog vele volgen, waar ik erg naar uitzie. I am looking forward to continue the work on droplet snap-off with the creative and skillful experimentalist Yves Hennequin.

Gedurende mijn promotietijd heb ik de hulp gehad van drie heel goede bijvak studenten, te weten Hanneke Zijtveld-van der Wiel, Volkert de Villeneuve en Susan Kersjes. Jullie inzet, creativiteit en precisie hebben tot veel van de resultaten in dit proefschrift geleid, waarvoor dank. Ook dank ik de glasblazers en Kees Rietveld voor hun hulp in het bedenken en maken van vele bijzondere cuvetten.

Ik heb het geluk gehad om tijdens mijn promotietijd aan projecten buiten mijn eigen onderwerp te kunnen werken. In het bijzonder noem ik hier de projecten met Andrei Petukhov. Samen met jou en ook met Gert Jan Vroege, Xinyi Xian en Els de Hoog, ben ik vele malen naar Grenoble geweest om kleine hoek-röntgen verstrooiing te doen op de schitterende bundellijn mede mogelijk gemaakt door Igor Dolbnya. De discussies over Kikuchi en Kossel lines staan mij nog levendig voor de geest. Bolshoe Spasibo! Furthermore, I thank Paddy Royall for sharing his colloidal insights and the ongoing work is absolutely exciting. De afschuif-experimenten met Didi Derks zijn minstens even spannend als onze potjes squash. Didi, bedankt dat je me altijd liet winnen.

De sfeer in het Van 't Hoff-lab is reeds in vele dankwoorden geprezen. Ik sluit mij daar dan ook helemaal bij aan. In het bijzonder wil ik hier Rik Wensink noemen; het was een eer jouw paranimf te mogen zijn en mogen we in de toekomst samen met Didi vele culinaire hoogstandjes bereiden. Verder ging ik graag met Judith Wijnhoven lunchzwemmen. Ook wil ik Gijsje Koenderink en Albert Philipse bedanken, die mij hebben “ingewijd” in de colloïd-kunde. Beter dan dat kun je het niet krijgen.

Tot slot wil ik de mensen bedanken, die op een geheel andere, maar zeker even belangrijke manier hebben bijgedragen aan dit proefschrift. Gelukkig weten jullie al hoe belangrijk jullie voor mij zijn en blijven, want het is onmogelijk om dit op papier uit te drukken. Ik zal dan ook geen poging wagen, maar wil papa en mama bedanken, en mijn broer(tje) Gert, en Saskia en Tim, en mijn zusje Marlous. En mijn l-de-p en s-de-p, mijn meisje Suzanne. Dankjewel voor je liefde en steun gedurende de afgelopen jaren.

Curriculum Vitae

De auteur van dit proefschrift werd geboren op 10 november 1977 te Nijmegen. Vanaf 1990 bezocht hij het Carolus Borromeus College te Helmond, waar hij in 1996 zijn VWO-diploma haalde (gymnasium; cum laude). Aansluitend studeerde hij scheikunde aan de Universiteit Utrecht. Hij studeerde in 2001 af (cum laude) in de fysische en colloïd-chemie met een bijvak in de theoretische chemie. Gedurende zijn studie ontving hij tweemaal een VNCI-beurs alsmede de Unilever Research Prijs 2001 voor zijn afstudeeronderzoek.

Op 1 april 2001 trad hij als onderzoeker in opleiding in dienst bij de Stichting voor Fundamenteel Onderzoek der Materie (FOM). Hij was werkzaam aan het Van 't Hoff Laboratorium voor Fysische en Colloïd Chemie te Utrecht onder begeleiding van Prof. Dr. H. N. W. Lekkerkerker. Resultaten van het in dit proefschrift verkregen onderzoek zijn ondermeer gepresenteerd in Konstanz (5th Liquid Matter Conference, Duitsland 2002), San Feliu de Guixols (uitgenodigd spreker; Solid/Fluid Interfaces, Euresco Conference on Complex Fluid Interfaces, Spanje 2003), Lunteren (Wetenschappelijke Vergadering Statistische Fysica, Nederland 2004), New Haven (78th ACS Colloid and Surface Science Symposium, USA 2004), Praag (uitgenodigd spreker; 20th Condensed Matter Division Conference of the European Physical Society, Tsjechië 2004) en Berlijn (uitgenodigd spreker; DPG meeting "Physik seit Einstein", Duitsland 2005).

Vanaf 1 april 2005 is hij verbonden als post-doctoraal medewerker aan het Van 't Hoff laboratorium in het kader van de organisatie van de 6th Liquid Matter Conference.